On the dynamics of subduction and the effect of subduction zones on mantle convection

Gianluca Gerardi

université PARIS-SACLAY

NNT : 20XXSACLXXXX

Thèse de doctorat

UNIVERSITÉ PARIS SUD
Comprendre le monde, construire l'avenir

On the dynamics of subduction and the effect of subduction zones on mantle convection

Thèse de doctorat de l'Université Paris-Saclay
préparée à Université Paris-Sud

Ecole doctorale n°579 Sciences mécaniques et énergétiques, matériaux et géosciences (SMEMaG)
Spécialité de doctorat : Structure et évolution de la terre et des autres planètes

Thèse présentée et soutenue à Orsay, le 16/11/18, par

M. GIANLUCA GERARDI

Composition du Jury :

M. Stéphane LABROSSE Professeur, ENS de Lyon, Laboratoire de géologie de Lyon: Terre, planètes, environnement	Président/Rapporteur
M. Clint CONRAD Professeur, University of Oslo, Centre for Earth Evolution and Dynamics (CEED)	Rapporteur
M. Taras GERYA Professeur, ETH Zurich, Department of Earth Sciences	Examinateur
M. Boris KAUS Professeur, Johannes Gutenberg University Mainz, Institute of Geosciences	Examinateur
M. Damir JURIC Chargé de Recherche, CNRS, LIMSI	Examinateur
M. Neil M. RIBE Directeur de Recherche, CNRS, FAST	Directeur de thèse
Mme Anne DAVAILLE Directeur de Recherche, CNRS, FAST	Co-directeur de thèse

This project has received funding from the European Union's Horizon 2020 research and innovation programme under the Marie Sklodowska-Curie grant agreement No 642029 - ITN CREEP.

Thèse de Doctorat

École doctorale de "Science mécaniques et énergétiques, matérieux et géosciences" (SMEMaG)

On the dynamics of subduction and the effect of subduction zones on mantle convection

Auteur
M. Gianluca Gerardi

Directeur de thèse
M. Neil M. Ribe
Co-directrice
Mme Anne Davaille

Université Paris-Sud, 2018

Acknowledgements

My first thanks go to Neil M. RIBE, my supervisor during this adventure. I am grateful to him for all his valuable advice and suggestions and for everything I learned in these years, scientifically and beyond. Most of all, I am sincerely grateful to him for teaching me what it means to be a researcher, from the importance of nurturing the curiosity which stimulates the questions that feed this job, to the methods and tools to be used to chase the right answers. Then, I want to thank my co-supervisor Anne DAVAILLE who guided me through the magic world of colloids in the last part of the thesis. Thanks also for the essential help that you provided me when I first arrived in France and I had to face the scary monster of French bureaucracy. Also, I want to thank Christiane ALBA-SIMIONESCO, Oriana OSTA and all the other members of the Laboratoire Léon Brillouin (LLP) of the CEA Saclay who kindly helped me during the experimental analysis performed in their laboratory.

A warm thank you goes to all the people involved in the CREEP project, met in many workshops, courses and conferences over the past three years. Being part of this family has been a unique experience in scientific and human terms. In particular, I would like to thank Boris KAUS who welcomed me at the Johannes Gutenberg University of Mainz for a one month session of LaMEM simulations and Christian MÜLLER who supervised me during my industrial internship at SCHOTT company. A special thought goes to all the CREEP PhD students with whom I shared joys and sorrows during this journey (mainly joys, luckily) and, in particular, to Simon PREUß and Jana SCHIERJOTT who became good friends.

Last but certainly not least, a sincere thank you to all the people of the FAST laboratory. I could have not thought of a more stimulating environment for the experience of a PhD thesis. A special thanks go to Manon ROBBE-SAULE, Nicolò RUBENS SGREVA and Arnaud SALVADOR for the unforgettable CESFO lunches, coffee breaks and improvised French lessons.

Contents

List of Figures

List of Tables

Introduction

The Earth is one of the four rocky planets of our solar system. Like Mercury, Venus and Mars it mainly consists of silicate rocks and heavy metals. During its formation, it separated into three principal layers: a core, a mantle and a crust. The core, made mostly of an iron-nickel alloy (Birch, 1964), is the Earth's innermost part and is divided into two sections: the inner core, a solid sphere with a radius $\approx 1,200$ km (Engdahl *et al.*, 1974), and the outer core, a liquid shell $\approx 2,400$ km thick, enclosed between the inner core boundary and the core mantle boundary (CMB) (Birch, 1964; Li & Fei, 2014). The latter, located at $\approx 2,890$ km beneath the Earth's surface, represents the lower limit of the second principal layer of the Earth that is the mantle. This can be divided into two different parts: the lower mantle, principally composed of a magnesium silicate mineral with a distorted perovskite structure, and the upper mantle dominated by peridotite rocks (Davies, 2001). The lower mantle extends from the CMB up to $750-660$ km depth, while the upper mantle spans between $410-350$ km and 35 km (e.g. Niazi & Anderson, 1965; Davies, 2001). Between these two regions is a transition zone where the rocks undergo different phase transitions (e.g. Deuss & Woodhouse, 2001). Starting from a depth of 35 km (i.e. the Moho discontinuity), we finally come to the shallowest layer of the Earth, the crust. There are two types of crust: oceanic, which is thinner ($7-10$ km) and composed of rocks rich in magnesium silicate minerals (e.g. Klein, 2003) and continental, which is thicker ($35-40$ km) and composed of rocks rich in silicates and aluminum minerals (e.g. Cogley, 1984). A schematic vertical profile of the Earth's interior is shown in figure 1.1a.

As one immediately notices in figure 1.1a, there is no unique definition of the layers of the Earth from the crust down to the CMB. Depending on the type of investigation adopted (seismological, mineralogical or dynamical) the boundaries and the terminology of the different layers change. In this work, however, we shall refer only to the dynamical reference given in the third column, where we distinguish between the lithosphere, the upper and lower mantle, separated by the 660 km discontinuity where a viscosity jump occurs (Rudolph *et al.*, 2015), and the

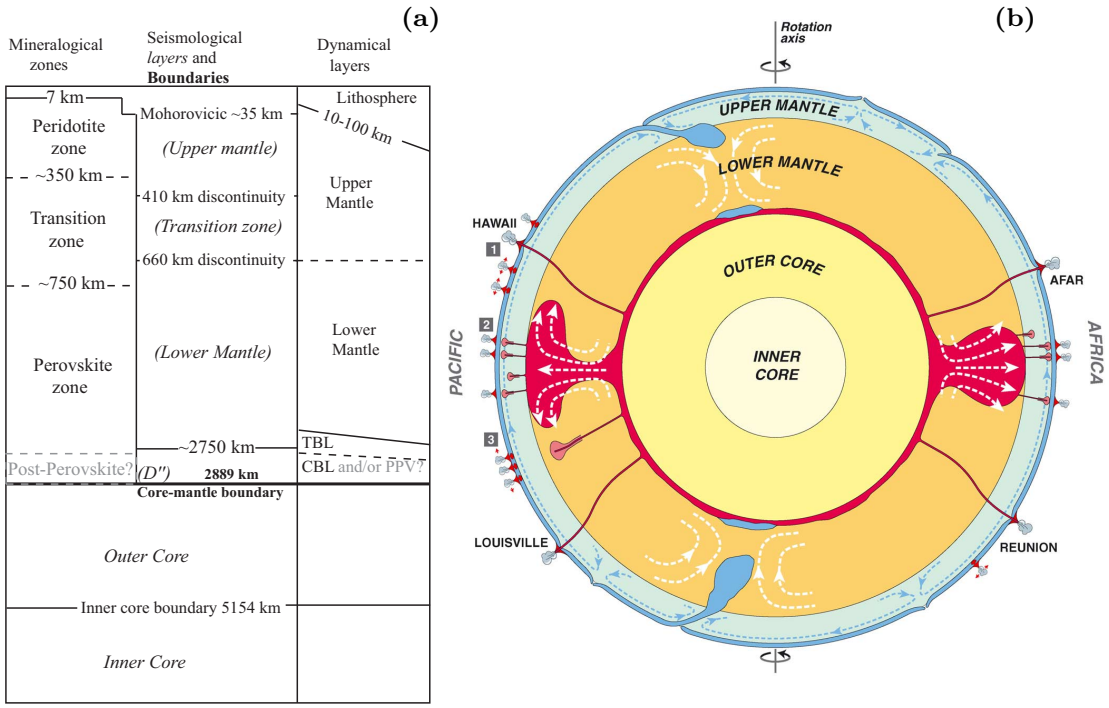

Figure 1.1. **(a)**: Earth's interior according to the terminology adopted by mineral physicists, seismologists and geodynamicists (Massmeyer, 2013; Davies, 2001). **(b)**: dynamic cross-section of the Earth (Courtillot *et al.*, 2003).

hot thermal boundary layer at the CMB. This division of the Earth is appropriate for the study of thermal convection in the mantle, i.e. the slow creeping flow of mantle rocks that results from the cooling of the Earth (e.g. Turcotte & Schubert, 2014; Ricard, 2015). A cartoon of mantle convection is shown in figure 1.1b, where we can see hot/light currents (i.e. plumes) rising from the CMB all the way to the Earth's surface, and cold/heavy tectonic plates, formed by breaking of the rigid lithosphere, sinking down toward the CMB.

The last phenomenon, known as subduction, is one of the principal surface expressions of mantle convection and represents a key ingredient of global geodynamics. It affects Earth processes ranging from the generation of mega-earthquakes and explosive volcanoes at the surface to the recycling of volatile species back into the deep interior. Yet despite its obvious importance, various aspects of subduction remain to be clarified, from the mechanics of the phenomenon itself to the effect of subduction zones on large-scale mantle convection.

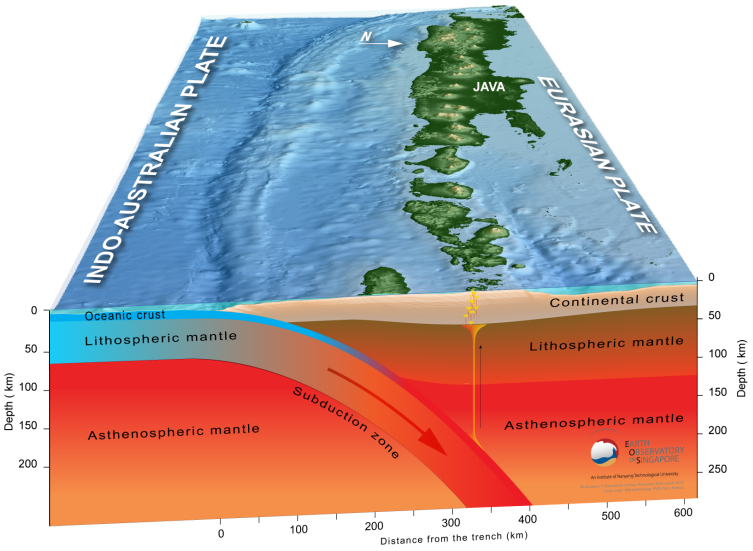

Figure 1.2. 3-D cross section of the subduction zone beneath the island of Java, Bali, Lombok and Sumbawa in Indonesia. Credits: Yves R. Descatoir, Earth Observatory of Singapore.

1.1 Subduction

A close-up view of a subduction zone is shown in figure 1.2. Here we see the oceanic subducting plate (SP), on the left, the continental overriding plate (OP), on the right, and the margin between the two where the SP starts to bend and sink, which is called the trench. This typical configuration captures the main features of a subduction system which, however, change significantly from region to region on Earth.

First of all, together with the oceanic-continental configuration, we also observe oceanic-oceanic (e.g. North American-Carribean plates) or continental-continental (e.g. Indian-Asian plates) plate collision on our planet. Moreover, even considering only the classical oceanic-continental collision, seismic tomography shows that subduction occurs with many different styles. For example, the SP sinks i) with a constant dip from upper to lower mantle, broadening in the transition zone, as in the Central America subduction zone; ii) nearly vertically (e.g. the Marianas trench) or iii) with a steep angle in the upper mantle, followed by flattening in the transition zone, e.g. the Tonga trench (e.g. Fukao *et al.*, 1992; Bijwaard *et al.*, 1998). Finally, concerning the OP deformation style, focal mechanisms of earthquakes occurring within the OPs indicate that it varies from highly compressional to highly extensional (e.g. Heuret & Lallemand, 2005). This can be appreciated from the map of figure 1.3, which shows the OP stress-state for the Earth's principal subduction zones. Among other features, we can recognize the

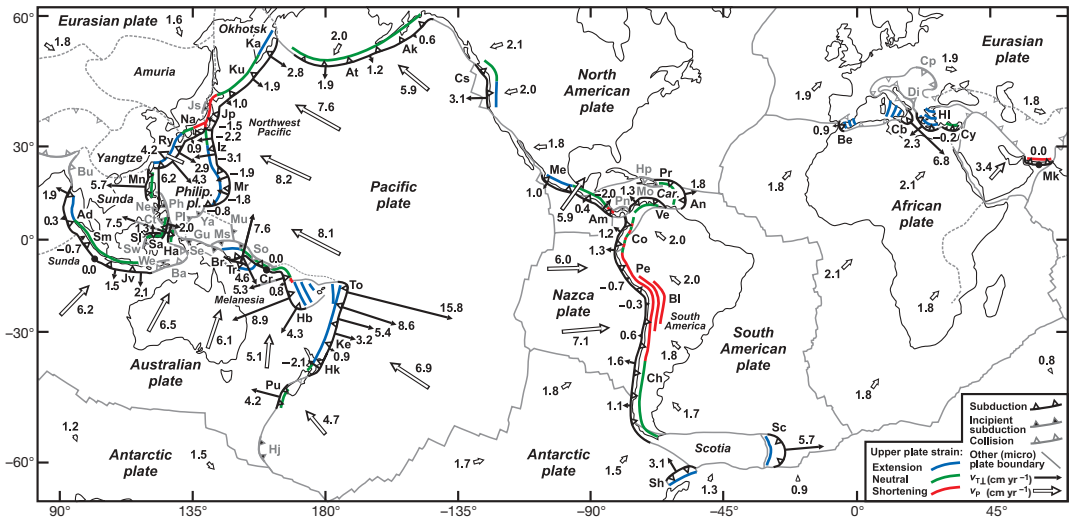

Figure 1.3. From Schellart *et al.* (2007): Map of major subduction zones on Earth with plate velocities computed relative to the Indo-Atlantic hotspot reference frame. The state of strain in the OP is reported in the legend at the bottom right corner.

strong compression of central South America (in red), related to the rise of the Andes mountains (e.g. Rutland, 1971; Sobolev & Babeyko, 2005) and the extension of the Eurasian plate at the central Mediterranean subduction zone (in blue) which, starting in the late Miocene, led to the opening of the Tyrrhenian basin (e.g. Boccaletti *et al.*, 1990; Faccenna *et al.*, 1996). Understanding how subduction gives rise to all these different features is one of the main challenges in modern geodynamics.

1.1.1 Subduction modeling

Numerical and experimental modeling of subduction have proved to be powerful techniques for investigating such complex phenomenon. Thanks to the impressive progress of the last decades, these tools have provided convincing explanations for many features of the present and past geological record, including the correlation between trench velocity and SP velocity (Funiciello *et al.*, 2008), the shape of island arcs (Morra *et al.*, 2006) and episodes of lower-mantle slab penetration (Goes *et al.*, 2008).

There are two main classes of subduction models: forced and free. In the first (forced) case, the system is partially or totally forced by a boundary condition imposed as a kinematic constraint. A classical example of this type of model is the 'corner flow' model of McKenzie (1969), shown in figure 1.4. Here the 2-D viscous flow in a wedge-shaped region is induced by the imposed speed U_0 of the wedge's inclined lower boundary representing the subducting plate. Following the

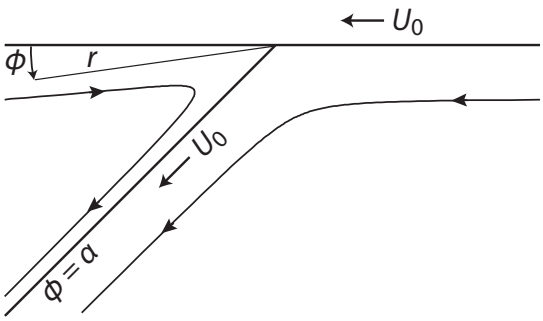

Figure 1.4. 2-D analytical model of McKenzie (1969) for mantle flow in subduction zones. Viscous fluid with uniform viscosity is contained in two wedge-shaped regions separated by the downgoing portion of the SP. The motions of the downgoing and surface portions of the SP are forced by imposed velocities U_0. Typical streamlines are shown as solid lines with arrows. Credits: Neil M. Ribe.

analytical model of McKenzie (1969), the subduction rate of the SP is imposed in other models of the forced class, either with a piston that pushes the SP toward the OP in analog models (figure 1.5a) or by prescribing it as a boundary condition in numerical models (figure 1.5c). This approach is useful to study specific features of subduction and also when one wants to mimic the effect of far-field driving forces (Schellart & Strak, 2016). However, it lacks self-consistency since there is an external source that continuously adds energy to the system. In the second (free) case, the motion and deformation of the plates are controlled entirely by the internal forces in the system. Usually, the only driving force taken into account is slab pull (e.g. Turcotte & Schubert, 2014) and subduction is triggered by imposing an initial dipping angle to the SP (figures 1.5b and 1.5d). This type of approach is useful for understanding the natural evolution of subduction systems and the causal link between the forces and the velocities observed within them. As will be described in § 3, the latter is the model class that has been chosen for the present study.

1.1.2 Subduction of an isolated plate

Figure 1.5 shows several examples of realistic model setups comprising both a SP and an OP. However, much progress in our understanding of subduction has first come from models that consider an isolated SP without an OP. In particular, this approach has provided significant insight into the origin of the different modes of subduction that have been observed both in analog and numerical models.

As recent studies have shown, one of the key parameters controlling the different styles of subduction is the viscosity contrast ($\lambda \equiv \eta_1/\eta_0$) between the SP ($\eta_1$) and the surrounding mantle (η_0) (e.g. Kincaid & Olson, 1987; Di Giuseppe *et al.*,

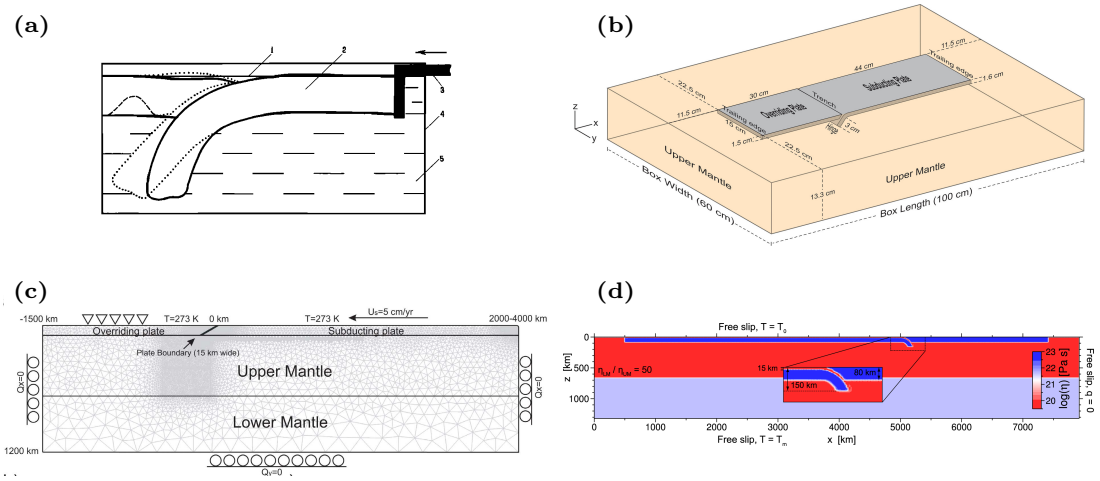

Figure 1.5. Examples of subduction model setups. Forced: **(a)** experimental (Shemenda, 1993), **(c)** numerical (Rodríguez-González *et al.*, 2012). Free: **(b)** experimental (Duarte *et al.*, 2013), **(d)** numerical (Holt *et al.*, 2015).

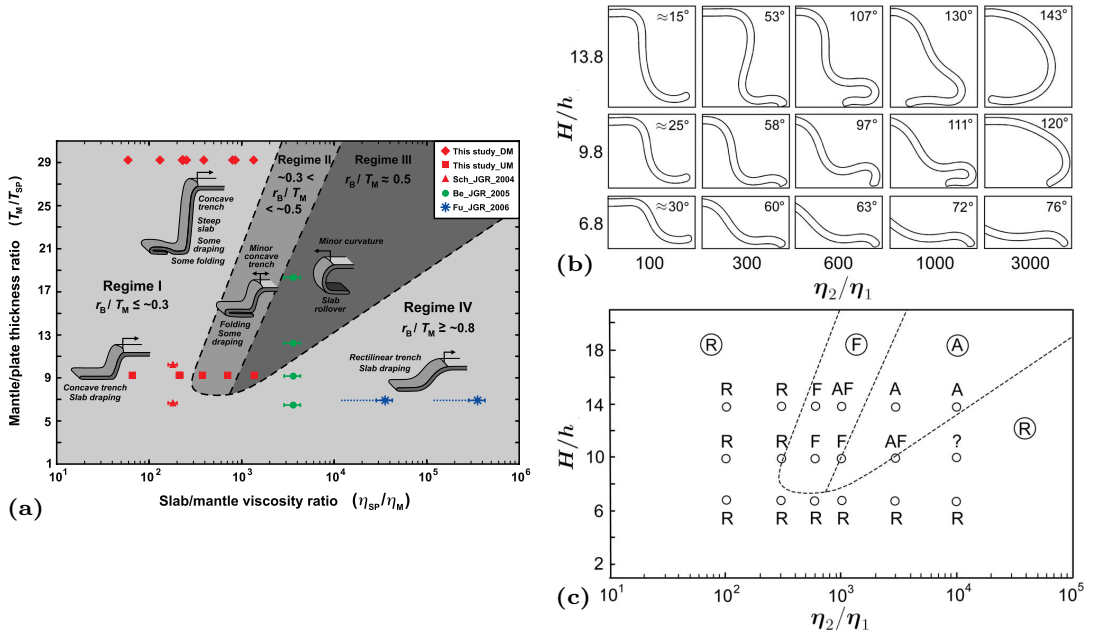

Figure 1.6. **(a)**: Phase diagram of Schellart (2008) showing the modes of free subduction as a function of the viscosity contrast (η_{SP}/η_M) and the ratio of the mantle depth to the sheet thickness (T_M/T_{SP}). **(b)-(c)**: Phase diagram of Li & Ribe (2012) showing the modes of free subduction as a function of the viscosity contrast (η_2/η_1) and the ratio of the mantle depth to the sheet thickness (H/h). In **(b)** the authors show the different shapes of the slab as it touches the bottom boundary. They also report the corresponding angle of the slab's tip. The dashed lines in **(c)** report the same regime boundaries given in **(a)**. Regime I and IV: Retreating mode. Regime II: Folding retreating mode. Regime III: Advancing mode.

2008). Considering together the effects of λ and the mantle/SP thickness ratio, Schellart (2008) proposed the phase diagram shown in figure 1.6a. Using just these two paramters, the author was able to classify a broad range of data coming from different laboratory studies (Schellart, 2004; Bellahsen *et al.*, 2005; Funiciello *et al.*, 2006). He identified four main modes of subduction: weak trench retreating (Regime I) and strong trench retreating (Regime IV), trench retreating with folding (Regime II), and trench advancing (Regime III). The same phase diagram has been reproduced quantitatively by Li & Ribe (2012) using a 3-D numerical model based on the boundary element method (figure 1.6c). As highlighted in figure 1.6b, the authors found a strong correlation between the subduction mode selected and the value of θ_D, representing the dip of the subducting slab as it impinges on the bottom boundary of the experiment/numerical model (a rough analog of the 660 km discontinuity). The authors concluded that the retreating mode (Regime I and IV) always occurs for $\theta_D < 90°$, retreating plus folding (Regime II) occurs when $\theta_D \in [97° - 130°]$ and for larger values of θ_D the trench advancing mode (Regime III) is selected.

Li & Ribe (2012), following the work of Ribe (2010), also clarified the role of the viscosity ratio λ in the dynamics of the SP by identifying a key dimensionless parameter, the SP's 'flexural stiffness' $\mathrm{St} \equiv \lambda\,(h/\ell_b)^3$, where h is the SP's thickness and ℓ_b, the SP's 'bending length', represents the length of the portion of the SP where the deformation is dominated by bending. I will come back in § 2.3.3 to the definition of ℓ_b and its meaning. Thanks to this proper measure of the mechanical resistance of the SP relative to that of the ambient mantle, Li & Ribe (2012) confirmed the scaling law found by Ribe (2010) showing that the slab's sinking speed V_{Sink} is controlled by the ambient mantle viscosity η_0 when $\mathrm{St} \leq 1$, and by the SP viscosity η_1 when $\mathrm{St} \gg 1$ (see figure 3.5, § 3.4.1 and Ribe (2010) for more details).

1.1.3 Two-plate interaction along a weak subduction interface

Even if models of an isolated SP are useful to capture meaningful features of subduction, adding an OP to the system is crucial for more realistic modeling of natural subduction zones. In this context three main questions arise: (i) how does the presence of the OP influence the kinematics of the SP? (ii) what controls the interplate stress state along the subduction interface? (iii) what drives the deformation and motion of the OP (e.g. Krien & Fleitout, 2008; van Dinther *et al.*, 2010; Gerya, 2011; Duarte *et al.*, 2013; Garel *et al.*, 2014)?

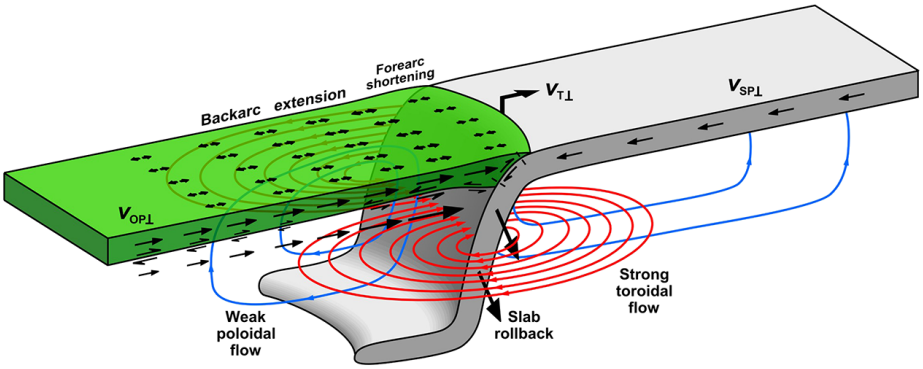

(a) Schellart & Moresi (2013): Influence of toroidal flow on backarc opening.

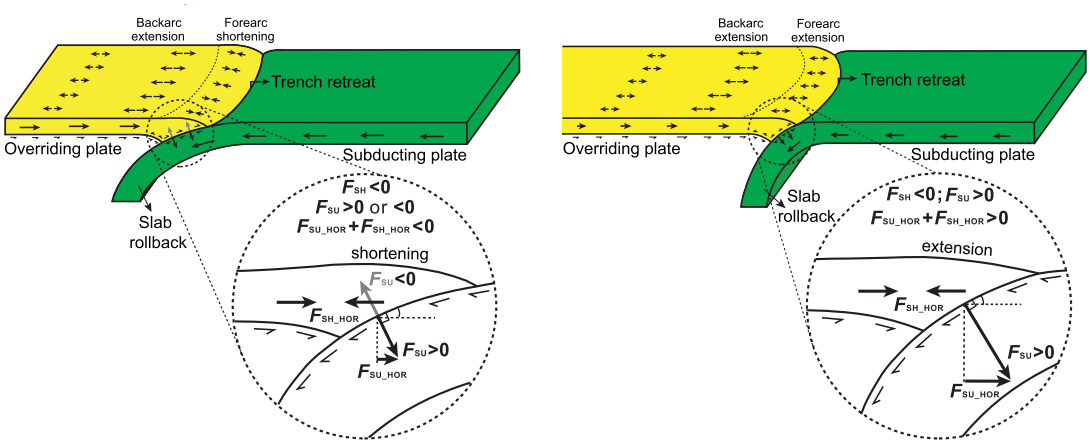

(b) Chen *et al.* (2015): Influence of interplate stresses on forearc deformation.

Figure 1.7. Mechanisms underlying OP deformation.

In recent years, several authors have used 3-D analog and numerical models of the free class to address the question of the mechanism of deformation of the OP, focusing, in particular, on the controlling factor for backarc extension. In general, it is found that backarc extension is strongly correlated with trench retreat (e.g. Duarte *et al.*, 2013; Meyer & Schellart, 2013; Schellart & Moresi, 2013; Chen *et al.*, 2016). A possible mechanical interpretation of this result is that slab rollback induces a toroidal mantle flow that exerts shear stresses on the base of the OP that in turn lead to backarc opening (figure 1.7a). The rate of extension in the backarc zone depends on whether the OP is free to move or is fixed at its end on the opposite side from the trench (Chen *et al.*, 2015). Interestingly, backarc extension is also observed in the 2-D (toroidal flow absent by definition) numerical model of Holt *et al.* (2015) when the OP is positively buoyant. For such a case, if the poloidal flow suddenly becomes weaker due to interaction of the slab with a viscosity increase at 660 km depth, a shift from extension to compression in the backarc zone may occur.

Another feature that has been explored recently is the influence of the subduction interface on the deformation of the OP and the rate of subduction of the SP. Based on analog models, Duarte *et al.* (2013) and Chen *et al.* (2015) concluded that interplate stresses at the interface are the primary control on forearc deformation within the OP. The forearc can be compressional or extensional depending on the magnitude of those stresses, whereas backarc deformation is insensitive to them (figure 1.7b). Duarte *et al.* (2013) also found that the subduction rate of the SP is controlled by the rheology of the subduction interface, decreasing strongly as the viscosity of the interface increases due to enhanced mechanical coupling between the plates.

Turning finally to the influence of the OP on the kinematics of the SP, Holt *et al.* (2015) showed that the OP viscosity does not influence significantly any of the characteristic velocities of the SP. They also found that increasing the OP's thickness decreases the rate of slab rollback, but does not affect the subduction rate or the slab's sinking speed. The same correlation between trench motion and the thickness of the OP is found in the 2-D numerical model of Garel *et al.* (2014).

1.2 Rayleigh-Bénard convection

In the first part of this introduction we have seen some examples highlighting the influence of subduction on different phenomena observed in the area close to the subduction zone itself. However, a global-scale effect of subduction zones might also occur on Earth. In particular, several authors have suggested that the viscous dissipation of energy occurring at subduction zones can strongly influence large-scale mantle convection (e.g. Conrad & Hager, 1999b; Korenaga, 2003). In order to understand how this might occur, it is useful here to give some basic concepts underlying the study of Earth's mantle convection.

In the simplest terms, thermal convection in the mantle can be described as a Rayleigh-Bénard (R-B) instability problem. A typical 2-D configuration of this type of convection is illustrated in figure 1.8, where we consider a fluid layer of thickness d confined between two horizontal planes (rigid or traction-free) kept at different temperatures. The system is heated from below and cooled from above ($T_1 > T_0$) and we assume that there is no volumetric heat generation within it. Under certain conditions, due to the density variation given by the gradient of temperature, the fluid layer becomes unstable and generates the flow indicated by the curved arrows in figure 1.8. This fluid motion repeats regularly in cells that extend horizontally according to the characteristic wavelength λ of the convection pattern (e.g. Ribe, 2015).

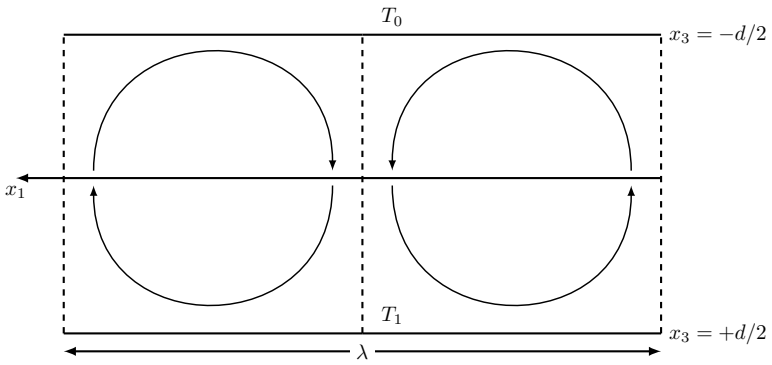

Figure 1.8. Modified from Turcotte & Schubert (2014): Rayleigh-Bénard model setup consisting of a fluid layer of thickness d, heated from below and cooled from above ($T_1 > T_0$). The characteristic horizontal wavelength of the convection pattern is λ. Note that the vertical coordinate increases downward.

For the R-B problem, the governing equations describing the conservation of mass, momentum and energy are the following:

$$\frac{\partial u_j}{\partial x_j} = 0 \tag{1.1a}$$

$$\frac{\partial P}{\partial x_i} = \eta \nabla^2 u_i - g_i \rho_0 \alpha (T - T_0) \tag{1.1b}$$

$$\frac{\partial T}{\partial t} + u_j \frac{\partial T}{\partial x_j} = \kappa \nabla^2 T, \tag{1.1c}$$

where κ is the thermal diffusivity and we consider an incompressible and isoviscous fluid (η=constant) in the relevant approximations for mantle convection of negligible inertia (Reynolds number, $\mathrm{Re} \approx 10^{-20}$) and infinite Prandtl number, $\mathrm{Pr} \approx 10^{23}$. Moreover, we assume the validity of the Boussinesq approximation according to which the density variations are retained only in the term that represents the buoyancy force, and are neglected everywhere else. This means that the density difference caused by the thermal expansion (ρ') is small enough not to affect the hypothesis of incompressibility but sufficient to drive the flow. The latter effect is taken into account in (1.1b) by the term $\rho' = -\rho_0 \alpha (T - T_0)$, where α is the volumetric coefficient of thermal expansion and T_0 is the reference temperature corresponding to the reference density $\rho_0 \gg \rho'$. We further notice that in (1.1b), P represents the dynamic pressure of the flow $P = p - \rho_0 g_i x_3$, that is the total pressure minus the hydrostatic contribution related to the reference density.

1.2.1 Onset of R-B convection

We now ask: what are the conditions that generate the instability in the fluid layer? This problem is addressed by means of a linearized stability analysis of the onset of convection when the motions and the thermal disturbance are infinitesimal. In this section I summarize some key results of this analysis, whose detailed explanation can be found in Turcotte & Schubert (2014).

Consider the setup shown in figure 1.8 with the fluid at rest. We assume a steady ($\partial/\partial t$) conductive state without any horizontal gradient ($\partial/\partial x_1 = 0$). The velocity is everywhere zero ($u_{ic} = 0$), and the steady conductive temperature profile T_c satisfies $\mathrm{d}^2T_c/\mathrm{d}x_3^2 = 0$. The solution is

$$T = T_c = \frac{(T_1 + T_0)}{2} + \frac{(T_1 - T_0)}{d}x_3, \tag{1.2}$$

Imagine now that we increase the temperature difference across the fluid layer up to the point where the slightest further increase causes the layer to become unstable and convection to start. Let the temperature be $T = T_c + T'$ and the velocity be $u_i = u_i'$, where T' and u_i' are small perturbations of the steady conductive state. Substituting these expressions into 1.1 and neglecting products of perturbation quantities, we obtain

$$\frac{\partial u_j'}{\partial x_j} = 0 \tag{1.3a}$$

$$\frac{\partial P'}{\partial x_i} = \eta\nabla^2 u_i' - g_i\rho_0\alpha(T' - T_0) \tag{1.3b}$$

$$\frac{\partial T'}{\partial t} + \frac{u_3'}{d}(T_1 - T_0) = \kappa\nabla^2 T'. \tag{1.3c}$$

We now assume that the upper and lower surfaces of the convecting layer are isothermal and free-slip, viz.

$$T' = 0 \quad \text{on} \quad x_3 = \pm d/2 \tag{1.4a}$$

$$\frac{\partial u_1'}{\partial x_3} = u_3' = 0 \quad \text{on} \quad x_3 = \pm d/2. \tag{1.4b}$$

Rewriting eq. (1.3) in terms of the stream function ψ', we reduce the problem to the two partial differential equations

$$\eta\nabla^4\psi' = \rho_0 g_3 \alpha \frac{\partial T'}{\partial x_1} \tag{1.5a}$$

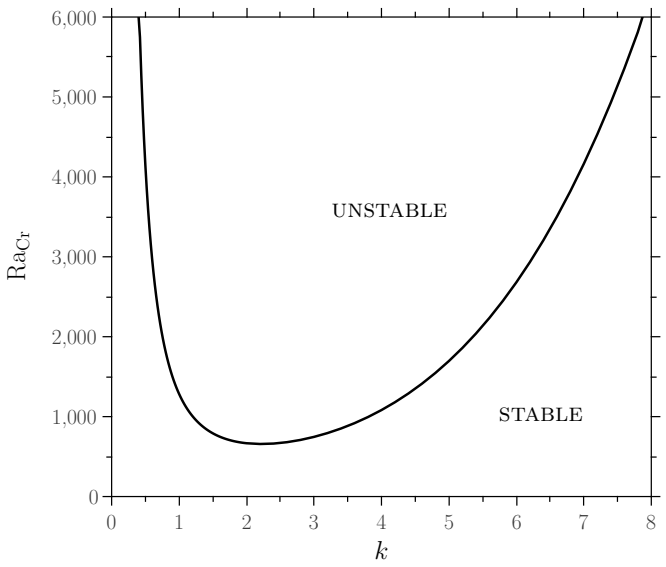

Figure 1.9. Crtitical Rayleigh number $\mathrm{Ra}_{\mathrm{Cr}}$ as a function of the dimensionless wavenumber k. The corresponding zones of stability of the layer are reported. The bounding surfaces are free-slip.

$$\frac{\partial T'}{\partial t} + \frac{1}{d}(T_1 - T_0)\frac{\partial \psi'}{\partial x_1} = \kappa \nabla^2 T', \tag{1.5b}$$

which admit solutions of the form

$$\psi' = \psi'_0 \cos\frac{\pi x_3}{d} \sin\left(\frac{2\pi x_1}{\lambda}\right) e^{st} \tag{1.6a}$$

$$T' = T'_0 \cos\frac{\pi x_3}{d} \cos\left(\frac{2\pi x_1}{\lambda}\right) e^{st}. \tag{1.6b}$$

where s is the growth rate that characterizes the time evolution of the perturbations. An expression for s is obtained by substituting (1.6a) and (1.6b) into (1.5b), yielding

$$\frac{sd^2}{\kappa} = \frac{\mathrm{Ra}k^2 - (\pi^2 + k^2)^3}{(\pi^2 + k^2)^2}, \tag{1.7}$$

where $k = 2\pi d/\lambda$ is the dimensionless wavenumber and Ra is the Rayleigh number defined as

$$\mathrm{Ra} = \frac{\rho_0 g_3 \alpha (T_1 - T_0) d^3}{\kappa \eta}. \tag{1.8}$$

The Rayleigh number expresses the relative importance of the buoyancy force acting against the viscous resistance of the fluid and the tendency of lateral temperature gradients to disappear by diffusion. Setting $s = 0$, we can finally find the

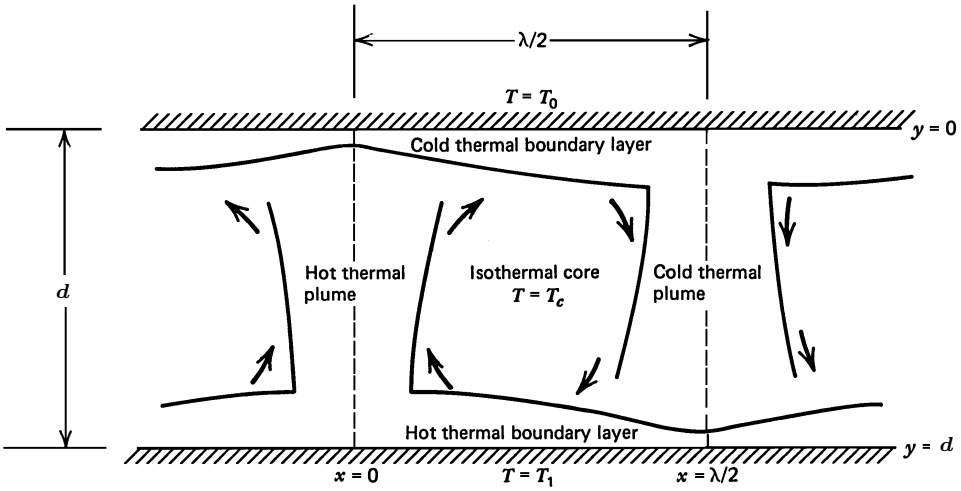

Figure 1.10. From Turcotte & Schubert (2014): Sketch of the 2-D flow of thermal convection with TBLs.

critical Rayleigh number at which convection begins:

$$\mathrm{Ra}_{\mathrm{Cr}} = \frac{(\pi^2 + k^2)^3}{k^2}. \tag{1.9}$$

The function $\mathrm{Ra}_{\mathrm{Cr}}(k)$ is shown in figure 1.9. The curve separates two zones: the UNSTABLE zone where $s > 0$ and perturbations grow exponentially with time; and the STABLE zone where $s < 0$ and perturbations are damped so that the layer remains stable against convection. Physically, the first case corresponds to a buoyancy force that is high enough to overcome the viscous resistance to convection, while in the second case the opposite is true.

In reality, random perturbations contain components of all wavenumbers. The critical Rayleigh at which convection begins is therefore the minimum value $\mathrm{Ra}_{\mathrm{min}}$ of $\mathrm{Ra}_{\mathrm{Cr}}(k)$, or

$$\mathrm{Ra}_{\mathrm{min}} = \frac{27\pi^4}{4} \approx 657.5. \tag{1.10}$$

By comparison, typical values of the Rayleigh number for the Earth's mantle (Ra_{m}) are in the range $10^6 - 10^7$, depending on whether one uses the upper mantle or the whole mantle thickness in the definition. Vigorous convection is therefore to be expected in the mantle.

1.2.2 Steady-state boundary layer analysis

Imagine now that vigorous ($\mathrm{Ra} \gg \mathrm{Ra}_{\mathrm{min}}$) convection in the fluid layer of figure 1.8 has reached the steady-state configuration shown in figure 1.10. The flow consists of an isothermal core bounded above and below by thermal boundary layers

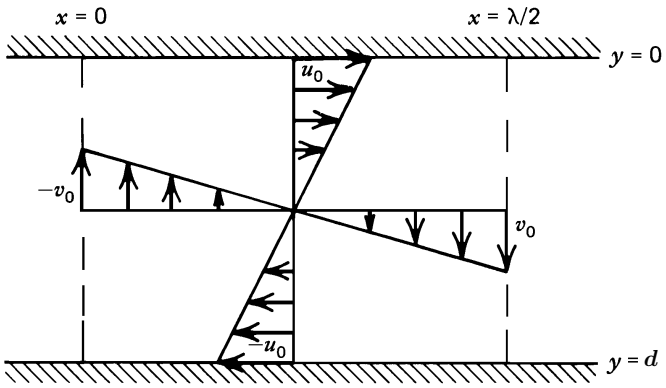

Figure 1.11. From Turcotte & Schubert (2014): Approximation of the velocity field within a convection cell.

(TBLs) and on the sides by cold (sinking) and hot (rising) thermal plumes. The boundary-layer structure of the flow is a direct consequence of the strong advection that controls heat transport in the fluid. Because the thermal Péclet number $\mathrm{Pe_T} \equiv \mathrm{RePr} \approx 10^3$ is large, advection effectively counteracts thermal diffusion and confines temperature gradients close to the boundaries of the cell. This resembles what happens in mantle convection, where horizontal TBLs are nothing else than the cold oceanic lithosphere (upper TBL) and the D''-layer (lower TBL).

For the configuration of figure 1.10, steady-state boundary layer analysis provides a useful scaling law for the convective heat transport as a function of the vigor of the flow. I now show briefly how we can obtain it.

We start from the integrated energy balance within the volume V of a single convection cell, bounded by free-slip surfaces S on the four sides:

$$2\eta \int_V e_{ij} e_{ij} = \int_S u_i \sigma_{ij} n_j dS - \int_V u_i g_i \rho_0 \alpha \Delta T_p dV, \tag{1.11}$$

where $e_{ij} = 1/2(\partial u_i/\partial x_j + \partial u_j/\partial x_i)$ is the strain rate tensor and $\sigma_{ij} = -P\delta_{ij} + 2\eta e_{ij}$ is the corresponding stress tensor. Equation (1.11) can be obtained by taking the dot product of the velocity and the momentum balance (1.1b) and then converting the volume integrals to integrals over the cell surface using Gauss's theorem. The quantity ΔT_p appearing in (1.11) is the temperature difference between the isothermal core $T = T_c$ and the upper (T_0) or lower boundary (T_1). Cold and hot thermal plumes are then assumed to have the same temperature structure as the corresponding cold or hot TBL.(Turcotte & Schubert, 2014; Conrad & Hager, 1999b). From the continuity equation and the assumption of free-slip boundaries, the first integral on the right-hand side of (1.11) vanishes, whence we obtain

$$2\eta \int_V e_{ij} e_{ij} = - \int_V u_i g_i \rho_0 \alpha \Delta T_p dV, \tag{1.12}$$

which states that the viscous dissipation in the fluid volume is exactly balanced by the buoyancy flux associated with the thermal plumes.

Now we use the simplified 2-D velocity field shown in figure 1.11 to perform a scaling analysis of (1.12). First, we identify a characteristic velocity scale $v_0 \approx u_0 \sim U$ and a characteristic length scale $\lambda/2 \approx d \sim D$. Because $e_{ij} \sim U/D$ and the volume of the square 2-D cell is $V \sim D^2$, the viscous dissipation term scales as

$$2\eta \int_V e_{ij} e_{ij} \sim \eta U^2. \tag{1.13}$$

The buoyancy term scales as

$$-\int_V u_i g_i \rho_0 \alpha \Delta T_p dV \sim U \rho_0 g_3 \alpha |\Delta T_p| (D\delta), \tag{1.14}$$

where the volume over which we integrate here is that of the descending and rising thermal plumes, whose thickness δ is determined by the growth of the corresponding TBL. The parameter δ is obtained from the half-space model

$$\delta \sim \sqrt{\kappa t} \sim \sqrt{\kappa D/U}, \tag{1.15}$$

which describes how the TBL thickens by conductive cooling/heating during a time $t \sim D/U$ until it becomes unstable and starts to sink/rise. Using (1.15) with (1.14) and substituting (1.13) and (1.14) into (1.12), we finally obtain an expression for the characteristic velocity U:

$$\frac{UD}{\kappa} \sim \mathrm{Ra}^{2/3}, \tag{1.16}$$

where Ra has been defined in (1.8) and $|\Delta T_p| \sim \Delta T \equiv (T_1 - T_0)$ because $T_c - T_0 = 1/2(T_1 - T_0)$.

The last step is to correlate the velocity (1.16) with the convective heat flux. The latter has to be equal to the total heat flow Q evacuated from the upper boundary of the convection cell. From the half-space cooling model of the upper TBL, we obtain

$$Q = 2K\Delta T_p \left(\frac{u_0 \lambda/2}{\pi\kappa}\right)^{1/2} \sim K\Delta T \left(\frac{UD}{\kappa}\right)^{1/2}, \tag{1.17}$$

where K is the thermal conductivity of the fluid. Now the heat that would be transported by the cell purely by conduction in the absence of convection is

$$Q_c = K\Delta T \frac{\lambda}{2d} \sim K\Delta T. \tag{1.18}$$

The Nusselt number of the cell $\mathrm{Nu} = Q/Q_c$ therefore scales as

$$\mathrm{Nu} \sim \left(\frac{UD}{\kappa}\right)^{1/2}. \tag{1.19}$$

Using eq. (1.16) for the velocity U in eq. (1.19), we finally get

$$\mathrm{Nu} \sim \mathrm{Ra}^{1/3}, \tag{1.20}$$

which is the well-known scaling law connecting the (dimensionless) heat flow evacuated by the cell with the strength of convection within it.

Eq (1.20) gives some useful information on the long-term evolution of the convecting system. We will see in the next section how we can exploit this argument to build a thermal evolution model able to make predictions about the present-day energy budget of the Earth.

1.3 Thermal evolution of the Earth

The Earth has been cooling down for several billion years. Estimates of the mantle temperature T_m indicate a temperature drop of ≈ 200 K from the beginning of mantle sub-solidus convection ($T_m \approx 1800$ K, Litasov & Ohtani (2002)) until today ($T_m \approx 1600$ K, McKenzie *et al.* (2005)). These values constrain the average cooling rate of the Earth to 50 ± 25 K Gy^{-1} (Jaupart & Mareschal, 2010), which seems to be consistent with geochemical data from the analysis of mid-ocean ridge basalts (Abbott *et al.*, 1994).

While it cools, the Earth also generates heat due to radioactive decay of uranium (U), thorium (Th) and potassium (K) (e.g. Turcotte & Schubert, 2014). Thus, in order to measure the efficiency of the Earth's cooling, it proves useful to define the Urey ratio Ur as the ratio of the global rate of heat generation H to the global rate of heat loss Q:

$$\mathrm{Ur} = \frac{H}{Q}. \tag{1.21}$$

For the present-day Earth, geochemical data suggest $\mathrm{Ur} \in [0.1-0.5]$, depending on the different estimates of H and Q used (e.g. Jaupart *et al.*, 2015; Davies, 2001; Stein *et al.*, 1995; Jochum *et al.*, 1983; O'Connell & Hager, 1980) and on the assumption made concerning the role (active or passive) of continental heat sources in driving mantle convection (Jaupart & Mareschal, 2010). In any case, the data provide a robust upper limit $\mathrm{Ur} \leq 0.5$.

Given this range of Ur, we can now try to build a cooling model for the Earth

which is consistent with this geochemical constraint.

1.3.1 Parameterized cooling model

We start from the Earth's global energy balance

$$M \langle C_p \rangle \frac{d\langle T \rangle}{dt} = -Q + H, \tag{1.22}$$

where M is the mass of the Earth, C_p its heat capacity, T its temperature, Q the total rate of heat loss and H the total rate of heat production. We indicate with the symbol $\langle\rangle$ a spatially averaged value of the corresponding variable. Assuming an exponential decay with time of the amount of heat generated by the sum of the radioactive elements U, Th and K, H can be approximated as

$$H(t) = H_0 e^{-t/\tau_D}, \tag{1.23}$$

where $t = 0$ at present and $t < 0$ in the past, while τ_D represents an average decay time-scale of the three elements, whose value is $\tau_D \approx 3$ Gy (Labrosse & Jaupart, 2007). An expression for Q is obtained from the scaling law (1.20) derived earlier, where $Q \sim K\Delta T \mathrm{Ra}^{\beta}$, with $\beta = 1/3$. Considering now a temperature-dependent viscosity $\eta(T)$, we can write

$$Q = C T^{1+\beta} \eta^{-\beta}(T), \tag{1.24}$$

where C is a constant taking into account the dependence on all the different fluid properties that depend weakly on temperature (Jaupart & Mareschal, 2010). Using an Arrhenius-type viscosity law $\eta = \eta_0 (T/T_0)^{-n}$ and noting that variations of temperature in the Earth are much smaller than its absolute value (a drop of 200 K against a present-day mantle temperature of 1600 K), we can linearize eq.(1.24) around a reference value T_0, obtaining (Christensen, 1985; Labrosse & Jaupart, 2007)

$$Q = Q_0 \left[1 + (1 + \beta + \beta n) \frac{T - T_0}{T_0} \right], \tag{1.25}$$

where Q_0 is the heat loss at the reference temperature T_0 and $n = 35$ (Davies, 1980; Christensen, 1985). Substituting (1.25) and (1.23), into (1.22) we finally obtain the Earth's energy equation

$$M C_p \frac{dT}{dt} = -Q_0 \left[1 + (1 + \beta + \beta n) \frac{T - T_0}{T_0} \right] + H_0 e^{-t/\tau_D}, \tag{1.26}$$

where we have dropped the symbol $\langle\rangle$ to lighten the notation.

A critical parameter that can be extracted from eq.(1.26) is the characteristic time-scale τ_R of mantle convection underlying the secular cooling of the Earth. This is the time required for the temperature and the heat flux to drop by a factor e when the heat sources are instantaneously removed. Hence, it tell us how quickly mantle convection adapts to an external perturbation which changes its state of equilibrium, for example a new boundary condition or a new rate of heat generation (Labrosse & Jaupart, 2007). Setting to zero the heat production term in(1.26), we obtain

$$\tau_R = \frac{MC_pT_0}{(1+\beta+\beta n)\,Q_0}, \tag{1.27}$$

which leads to $\tau_R \approx 800$ Myr, adopting standard values of $n = 35$, $\beta = 1/3$, $M = 6 \times 10^{24}$ kg, $Q_0 = 30$ TW, $T_0 = 1300$ K and $C_p = 1200$ J kg^{-1} K^{-1}. From the analytical solution of (1.26)

$$T = T_0 + \frac{Q_0\tau_R}{MC_p}\left(e^{-t/\tau_R} - 1\right) + \frac{\tau_R}{MC_p}\left(\frac{\tau_D}{\tau_D - \tau_R}\right)H_0\left(e^{-t/\tau_D} - e^{-t/\tau_R}\right), \tag{1.28}$$

in the limit $t \gg \tau_R$, we finally obtain a simple expression for the present-day Urey ratio (Labrosse & Jaupart, 2007)

$$\mathrm{Ur} = \frac{\tau_D - \tau_R}{\tau_D}, \tag{1.29}$$

which predicts Ur = 0.73, higher than the upper limit constrained by geochemical data.

1.3.2 Viscous dissipation of energy at subduction zones

One possible explanation for the failure of the cooling model presented above lies in the small value of the mantle relaxation time τ_R, which makes the process of secular cooling highly sensitive to any fluctuations from the equilibrium state.

In the context of the calculations presented in the preceding section, the low value of τ_R might be ascribed to the exponent β, which we assumed to have the value 1/3 in accordance with the scaling law (1.20). However, there is no good reason to suppose that $\beta = 1/3$ is representative of mantle convection. First, the prediction $\beta = 1/3$ assumes that there are no volumetric heat sources within the mantle. As we have seen, this is not a good approximation for whole-mantle convection given the radioactive decay of uranium, thorium and potassium. Second, convection models with the horizontal convection pattern like the one of

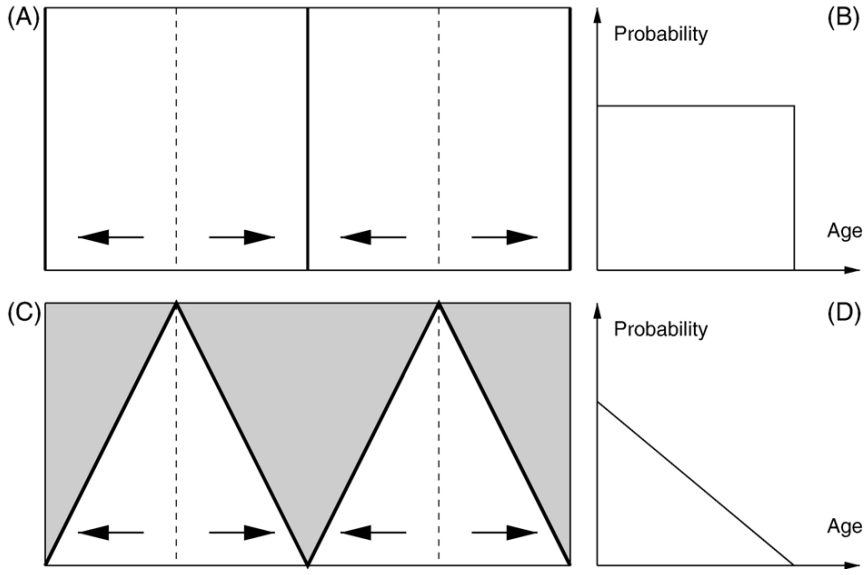

Figure 1.12. From Labrosse & Jaupart (2007): Plate tectonics systems and corresponding seafloor age distributions. The thick solid lines represent subduction zones while dashed lines are ridges. In (A) all the plate subducts at the same travel time leading to the rectangular age distribution shown in (B). In (C) the presence of continents, in gray, allow for subduction of young plates. Such a system shows an Earth-like triangular seafloor distribution (D).

figure 1.10 (e.g. Grigné *et al.*, 2005) are characterized by a 'rectangular' seafloor age distribution (Labrosse & Jaupart, 2007). The latter arises from the fact that all the plates start to subduct after traveling the same time, thus inducing a constant spatial distribution of seafloor ages in the whole domain of the model (figure 1.12(A)-(B)). On the contrary, the peculiar characteristic of mantle convection is to have generated a plate-tectonics system with a 'triangular' seafloor age distribution (Sclater *et al.*, 1981; Rowley, 2002; Cogné & Humler, 2004). A simplified representation of such a system is depicted in 1.12(C). Because young plates also can now subduct, the spatial distribution of seafloor ages in the whole model domain has a peak for short seafloor ages and decreases linearly as the seafloor age increases (figure 1.12(D)). Taking into account this feature, Labrosse & Jaupart (2007) obtained $\tau_R \approx 10$ Gy in their empirical cooling model. Third, the assumption of an isoviscous system neglects the dissipation of energy that occurs at subduction zones where highly viscous lithospheric plates must bend and then slide along the subduction interface. The resistance to deformation at such plate boundaries might partly decouple the dynamics of the lithosphere (i.e. the upper TBL) from the mantle convection that takes place below it. The plate speed and the corresponding surface heat flow would then be less sensitive to any variations in the properties of the mantle, thereby reducing the effective value of β.

This latter argument has been the object of considerable debate in the past 20 years. In fact, it is still unclear whether or not subduction zones dissipate a significant amount of energy (e.g. Irvine & Schellart, 2012; Buffett & Becker, 2012; Leng & Zhong, 2010; Krien & Fleitout, 2008; Davies, 2009; Buffett, 2006; Rose & Korenaga, 2011; Conrad & Hager, 1999b). In the pioneering work of Conrad & Hager (1999a), the authors suggested that the bending of long and highly viscous plates at subduction zones dissipates most of the energy that drives mantle convection. On this view, the surface heat flux is nearly independent of the underlying mantle, implying $\beta \approx 0$ (Conrad & Hager, 1999b). A key parameter in the model of Conrad & Hager (1999a) is the minimum radius of curvature $R_{\min}$ of the subducting plate, which the authors take to be 200 km. Subsequently, Korenaga (2003) proposed a counterintuitive scaling law with $\beta < 0$, implying that the surface heat flow decreases as mantle convection becomes more vigorous. According to Korenaga, the thickening of the lithosphere is controlled by dehydration during melting at mid-ocean ridges. A hotter mantle (higher values of $\mathrm{Ra_m}$), which produces more melt, would thus lead to a thicker lithosphere that slows down mantle convection. Davies (2009) compared two different mantle convection models in which the lithosphere thickens either by conductive cooling or by the dehydration stiffening process. He concluded that the result $\beta < 0$ is an artefact of the small value of $R_{\min}$ = 200 km and the high value of the SP viscosity $\eta_1 = 10^{23}$ Pa s assumed by Korenaga (2003). Higher values of $R_{\min}$ = 300-500 km and/or lower lithosphere viscosities ($\eta_1 = 10^{22}$ Pa s) recover the standard result $\beta = 1/3$ and imply that the dissipation of energy at subduction zones is minor. Other authors have suggested that the viscous dissipation associated with the deformation of the lithosphere is never dominant. Using a numerical model for compressible convection, Leng & Zhong (2010) found that the dissipation occurring in a subduction zone is 10-20 % of the total dissipation. A slightly wider range, 10-30 %, is suggested by the study of Krien & Fleitout (2008), who combined analysis of short and intermediate wavelength gravity and geoid anomalies with the predictions of a 2-D numerical model. Finally, Capitanio *et al.* (2007) used a numerical model of a viscoelastic plate subducting below a free surface to show that the energy consumed to stretch and bend the plate is 25-50 % of the total dissipation.

1.4 Thesis outline

The thesis is organized as follows:

- in Chapter 2 the Stokes flow is presented along with different solutions which characterized it. A particular technique (Boundary-integral representation), useful to solve this type of flow, is also described and several results of thin viscous-sheet theory are derived;
- in Chapter 3 the results published in Gerardi & Ribe (2018) are presented. This work focuses on unmasking the mechanics underlying the phenomenon of subduction by means of a numerical model built with the Boundary Element Method (BEM), here described. Three main aspects of subduction are investigated: the kinematics of the subducting plate, the overriding plate deformation and the mechanical role played by the subduction interface;
- in Chapter 4, the results of the manuscript "Gerardi G., Ribe N. M., & Tackley P. J. Plate bending, energetics of subduction and modeling of mantle convection: a boundary element approach", currently under review for *Earth and Planetary Science Letters*, are presented. Based on the same BEM model, this study specifically explores the energetics of subduction. The influence of viscous dissipation of energy at subduction zones on large-scale mantle convection is also studied;
- in Chapter 5, laboratory modeling of mantle convection is introduced. Here, preliminary results obtained running a convection experiment based on the drying of an aqueous colloidal dispersion of silica nanoparticles are presented.

Chapter 2

Stokes flow

Theoretical models developed for the study of inertialess flows underlie the investigation of many geophysical flows of the Earth's mantle, where, as already anticipated in § 1.2, a typical value of the Reynolds number is $\mathrm{Re} \approx 10^{-20}$. An important class of such flows is that of an incompressible, isothermal and purely viscous Newtonian fluid. In this case the governing equations are

$$\frac{\partial u_j}{\partial x_j} = 0 \tag{2.1a}$$

$$\frac{\partial \sigma_{ij}}{\partial x_j} = f_i \tag{2.1b}$$

$$\sigma_{ij} = -p + 2\eta e_{ij}, \qquad e_{ij} = \frac{1}{2}\left(\frac{\partial u_i}{\partial x_j} + \frac{\partial u_j}{\partial x_i}\right) \tag{2.1c}$$

where we recognize the continuity equation (2.1a), the balance of momentum (2.1b) and the stress tensor σ_{ij} and the strain-rate tensor e_{ij} in (2.1c). Here, we consider the case of a flow produced entirely by body forces, whose distribution per unit volume is f_i. For buoyancy-driven flows, the case of interest for the present work, $f_i = \rho g_i$.

Flow satisfying (2.1), called Stokes flow, presents a number of interesting properties. First, like all slow viscous flows, it is characterized by the property of instantaneity, whereby the velocity field u_i and the stress state σ_{ij} are determined exclusively by the distribution of the forcing term f_i and the boundary conditions at that specific instant. This means there is no time lag between the forcing and the fluid's response to it. Therefore, the temporal evolution of the flow is simply due to the temporal evolution of the driving term (e.g. Ribe, 2015). Next, as a consequence of its linear rheology, Stokes flows exhibit also the properties of linearity and reversibility. The first implies the principle of superposition, whereby

the sum of any two solutions (e.g., for different forcing distributions or boundary conditions) is also a solution. It also implies that u_i and σ_{ij} are directly proportional to the forcing term that generates them. Reversibility states that if the sign of the forcing term is reversed, the sign of u_i and σ_{ij} of all the material points belonging to fluid changes. The reversibility principle is particularly powerful when used in combination with symmetry arguments, because it allows us to evaluate if a given hypothetical behavior is physically possible or not (figure 2.1).

2.1 Singular solutions

Due to their linearity, the Stokes equations admit several singular solutions. These arise when the velocity and/or the pressure becomes infinite at one or more points within the fluid. We distinguish between two main classes of singular solutions: those involving point or (in two dimensions) line forces, and those related to volume sources and sinks. In this paragraph, I will focus on the singular solution associated with a line force. For more information on all the other singular solutions, refer to Ribe (2015) and Kim & Karrila (2013).

Imagine that a point force F_i (Stokeslet) is applied at a position $\mathbf{x}$ (the bold symbol denotes a vector) in the fluid. The velocity and the stress induced at any point $\mathbf{y}$ will satisfy (Ribe, 2015):

$$\frac{\partial u_j}{\partial x_j} = 0 \tag{2.2a}$$

$$\frac{\partial \sigma_{ij}}{\partial x_j} = -F_i \delta(\mathbf{y} - \mathbf{x}) \tag{2.2b}$$

where $\delta(\mathbf{y} - \mathbf{x}) = \delta(y_1 - x_1)\delta(y_2 - x_2)\delta(y_3 - x_3)$ and δ is the Dirac delta-function. Given the proportionality between u_i, σ_{ij} and the forcing term, and requiring that $u_i \to 0$ and $\sigma_{ij} \to -p_0\delta_{ij}$ as $|\mathbf{y} - \mathbf{x}| \to \infty$, where p_0 is a far-field (dynamically irrelevant) pressure, u_i and σ_{ij} can be written as

$$u_i = J_{ij}F_j/\eta, \qquad \sigma_{ik} = K_{ijk}F_j, \tag{2.3}$$

where we introduce the tensorial Green's functions J_{ij} and K_{ijk}, representing the singular solutions of the velocity (J_{ij}) and the stress (K_{ijk}) due to a unit line force. Using eq. (2.3) in eq. (2.2) and dropping the arbitrary vector F_j, the governing equations of the flow assume the form

$$\frac{\partial J_{ij}}{\partial x_i} = 0 \tag{2.4a}$$

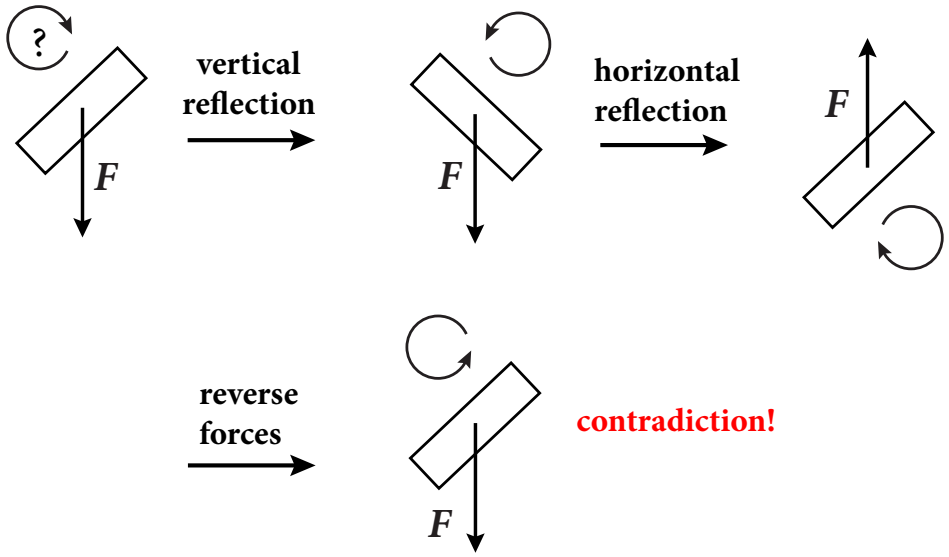

(a) Rigid body with fore-aft symmetry falling under gravity in an infinite fluid: rotation can not occur.

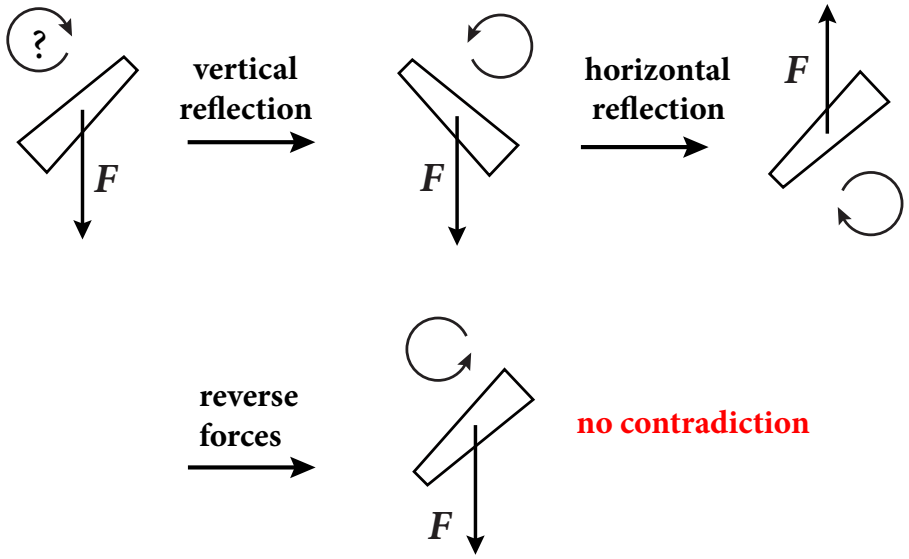

(b) Rigid body lacking fore-aft symmetry falling under gravity in an infinite fluid: rotation can occur.

Figure 2.1. Examples of the exploitation of the property of reversibility characterizing Stokes flow. Credits: Neil M. Ribe.

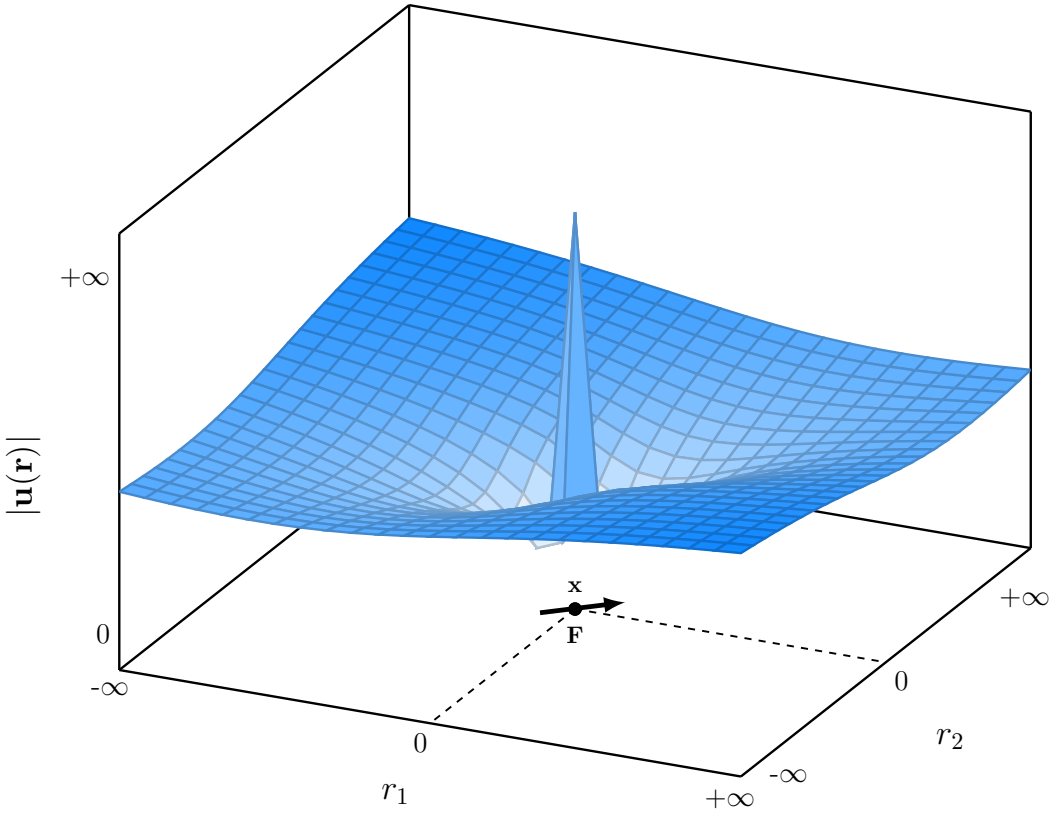

Figure 2.2. Spatial distribution of the norm of the velocity vector corresponding to the expression for J_{ij} in (2.5). The line force acts in $\mathbf{x}$ and we consider $F_1 = F_2 = \eta = 1$, so that $u_i = J_{ij}$.

$$\frac{\partial K_{ijk}}{\partial x_i} = -\delta_{jk}\delta(\mathbf{y}-\mathbf{x}), \tag{2.4b}$$

whose solutions in a 2-D domain, the one of interest in the present thesis, are (Pozrikidis, 1992; Ribe, 2015):

$$J_{ij}(\mathbf{r}) = \frac{1}{4\pi}\left(-\delta_{ij}\ln r + \frac{r_i r_j}{r^2}\right), \qquad K_{ijk}(\mathbf{r}) = -\frac{1}{\pi}\frac{r_i r_j r_k}{r^4}, \tag{2.5}$$

where $\mathbf{r} = \mathbf{y} - \mathbf{x}$ and $r = |\mathbf{r}|$.

The Green's functions in (2.5) are solutions for an unbounded 2-D Stokes flow generated by a line force acting at $\mathbf{x}$ with strength $\mathbf{F}$ per unit length of the line (the 2-D analog of the 3-D Stokeslet). For such a configuration, we show in figure 2.2 the spatial distribution of the norm of the velocity vector $\mathbf{u}(\mathbf{r})$. As we observe, the velocity is singular at $\mathbf{y} = \mathbf{x}$, where $|\mathbf{u}(\mathbf{r})| \to +\infty$, and decays away from $\mathbf{x}$. However, due to the logarithmic term in the Green's function $J_{ij}(\mathbf{r})$ in (2.5), $|\mathbf{u}(\mathbf{r})|$ does not vanish for $|\mathbf{r}| \to \pm\infty$, violating the boundary condition imposed at the beginning. This is related to Stokes's paradox, which states that a 2-D Stokes flow

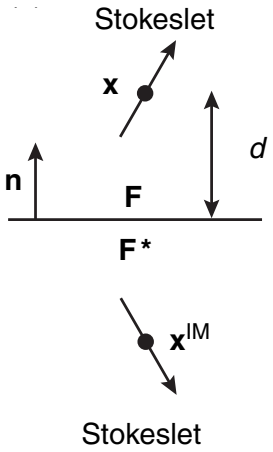

Figure 2.3. From Ribe (2015): Image system required to describe a general Stokes flow in the presence of an impermeable and traction-free wall. Because the latter is equivalent to a plane of mirror symmetry, the Stokeslet located at $\mathbf{x}$ has to be balanced by a Stokeslet reflected across the wall, located at the image point $\mathbf{x}^{\mathrm{IM}} \equiv \mathbf{x} - 2d\mathbf{n}$ and with strength $\mathbf{F}^* \equiv \mathbf{R}\cdot\mathbf{F}$.

around an infinitely long cylinder moving perpendicular to its axis does not exist (Ribe, 2015). In the following paragraph, we will show how we can resolve this paradox with the help of an impermeable boundary.

2.1.1 Effect of a free-slip wall

We consider now a 2-D Stokes flow bounded by a free-slip wall. The model setup that describes this new configuration is illustrated in figure 2.3. Here the flow is given by the combined action of two line forces: the first, located at the point $\mathbf{x}$ at a distance d from the boundary, is the line force that actually generates the flow; the second, located at the image point $\mathbf{x}^{\mathrm{IM}}$, is the one that we add in order to satisfy the boundary condition of an impermeable and traction-free wall. To fulfill such requirements, $\mathbf{x}^{\mathrm{IM}}$ has coordinates $\mathbf{x}^{\mathrm{IM}} \equiv \mathbf{x} - 2d\mathbf{n}$, where $\mathbf{n}$ is the vector normal to the wall, while the magnitude of the line force is equal to $\mathbf{F}^* \equiv \mathbf{R}\cdot\mathbf{F}$, where $R_{ij} \equiv \delta_{ij} - 2n_i n_j$ is a reflection tensor that reverses the sign of the wall-normal component of $\mathbf{F}$ and leaves its wall-parallel component unchanged (Ribe, 2015). From the superposition of the two line forces, we can thus find the new Green's functions $J^{\mathrm{G}}_{ij}(\mathbf{r})$ and $K^{\mathrm{G}}_{ijk}(\mathbf{r})$ which are solutions of the 2-D Stokes flow bounded by the free-slip wall:

$$J^{\mathrm{G}}_{ij}(\mathbf{r}) = J_{ij}(\mathbf{r}) + (-1)^{j+1} J_{ij}(\mathbf{r}^{\mathrm{IM}}) \tag{2.6a}$$

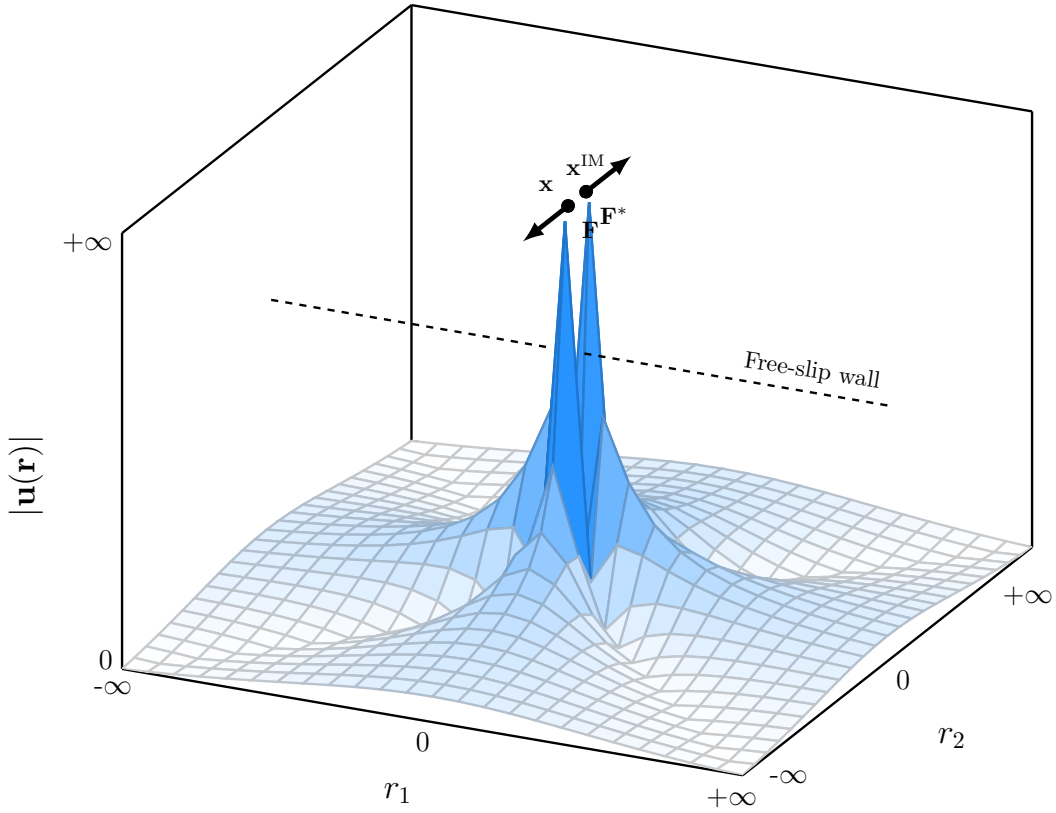

Figure 2.4. Spatial distribution of the norm of the velocity vector associated with the Green's function J_{ij}^{G} in (2.6a). The free-slip wall is at $r_2 = 0$ between the two line forces at $\mathbf{x}$ and $\mathbf{x}^{\mathrm{IM}}$. The line force acts normal to the wall ($F_1 = 0$) and $F_2 = \eta = 1$, so that $u_i = J_{ij}^{\mathrm{G}}$.

$$K_{ijk}^{\mathrm{G}}(\mathbf{r}) = K_{ijk}(\mathbf{r}) + (-1)^{j+1} K_{ijk}(\mathbf{r}^{\mathrm{IM}}), \tag{2.6b}$$

where $\mathbf{r}^{\mathrm{IM}} = \mathbf{y} - \mathbf{x}^{\mathrm{IM}}$ and $J_{ij}(\mathbf{r})$ and $K_{ijk}(\mathbf{r})$ are the Green's functions given above in (2.5) for an infinite fluid.

Now, because of the presence of the image singularity $J_{ij}(\mathbf{r}^{\mathrm{IM}})$ in eq. (2.6a), the logarithmic divergence for $|\mathbf{r}| \to \infty$ can be canceled out and Stokes's paradox resolved (Ribe, 2015). However, we need to pay attention to the orientation of the line forces as the solution of the governing equations exists only when the net force on the fluid is zero. Therefore, if for example we refer to the configuration of figure 2.3, a Stokes flow solution exists only if the Stokeslet has no horizontal component ($F_1 = 0$, see figure 2.4) or if we replace the free-slip wall with a no-slip wall that can sustain the horizontal stress. Similarly, considering the 2-D Stokes flow around an infinitely long cylinder, the solution exists in case of cylinder sinking perpendicular to a free-slip wall because the integrated normal stress over the wall turns out to be exactly equal and opposite to the drag on the cylinder. In

the case of a cylinder moving parallel to the wall, instead, a no-slip wall becomes necessary in order to counterbalance the horizontal drag on the cylinder.

2.2 Boundary-integral representation

By combining different types of singular solutions we can build a useful representation of Stokes flow, called the boundary-integral representation. Unlike the classical partial differential equations, which describe the spatial gradient of the velocity over the whole fluid domain V, the boundary-integral representation expresses the velocity at any point in V in terms of the velocity u_i and the stress σ_{ij} on the surface S bounding the fluid domain. This representation of the Stokes flow is particularly convenient as it reduces the dimensionality of the problem by one (we solve line integrals in a 2D domain or surface integrals in a 3D domain). Thus, it makes possible a powerful numerical technique, called the boundary-element method, which does not require the discretization of the whole flow domain (Pozrikidis, 1992).

The starting point for deriving the boundary-integral representation is the integral form of the Lorentz reciprocal theorem (Ribe, 2015)

$$\int_S u_i^* \sigma_{ij} n_j dS + \int_V f_j u_j^* dV = \int_S u_i \sigma_{ij}^* n_j dS + \int_V f_j^* u_j dV, \tag{2.7}$$

which relates two Stokes flow (u_i, σ_{ij}, f_i) and $(u_i^*, \sigma_{ij}^*, f_i^*)$.

Let (u_i, σ_{ij}) be the flow of interest with no body forces ($f_i = 0$), and $u_i^* \equiv J_{ij}(\mathbf{y}-\mathbf{x})F_j/\eta$ and $\sigma_{ik}^* \equiv K_{ijk}(\mathbf{y}-\mathbf{x})F_j$ be the flow induced by a line force $f_i^* \equiv F_i\delta(\mathbf{y}-\mathbf{x})$ located at $\mathbf{x}$. Substituting these expressions into (2.7) and dropping the arbitrary vector F_j yields

$$\frac{1}{\eta}\int_S J_{ij}(\mathbf{y}-\mathbf{x})\sigma_{ik}(\mathbf{y})n_k(\mathbf{y})dS(\mathbf{y}) - \int_V u_j(\mathbf{y})\delta(\mathbf{y}-\mathbf{x})dV(\mathbf{y}) = \\ = \int_S K_{ijk}(\mathbf{y}-\mathbf{x})u_i(\mathbf{y})n_k(\mathbf{y})dS(\mathbf{y}) \tag{2.8}$$

where the normal vector $\mathbf{n}$ points out of the fluid domain V. The second integral on the left-hand side can be rewritten as (Pozrikidis, 1992)

$$\int_V u_j(\mathbf{y})\delta(\mathbf{y}-\mathbf{x})dV(\mathbf{y}) = \chi(\mathbf{x})u_j(\mathbf{x}) \tag{2.9}$$

where $\chi(\mathbf{x}) = 0,\ 1/2,\ 1$ depending on whether $\mathbf{x}$ lies outside V, right on S, or inside V, respectively. Then substituting eq. (2.9) into eq. (2.8), we finally get the

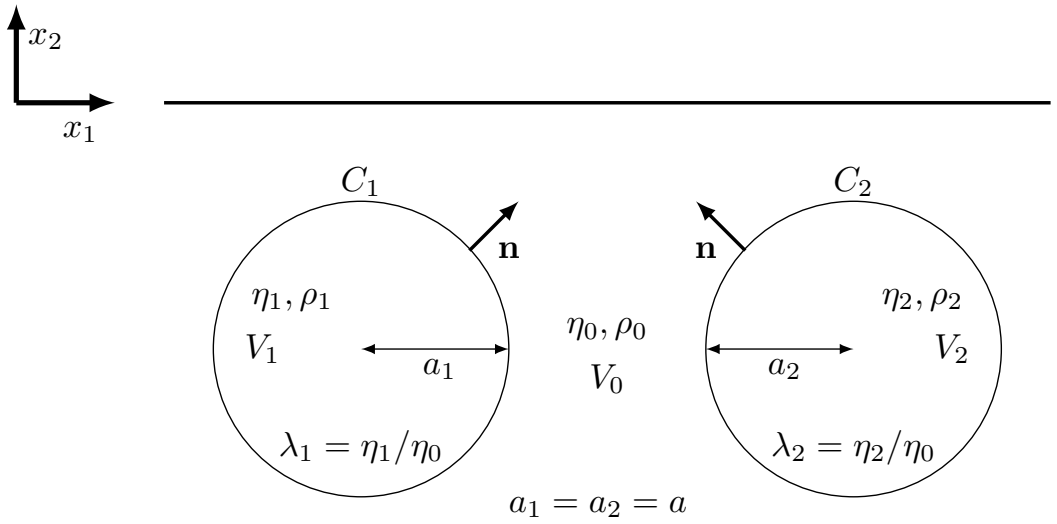

Figure 2.5. Two-dimensional model of two fluid drops immersed in an infinitely deep ambient fluid bounded at $x_2 = 0$ by a free-slip surface. The two drops, of radius a, have viscosity $\eta_i = \lambda_i \eta_0$ and density ρ_i, where $i = 1, 2$. η_0 and ρ_0 are the viscosity and the density, respectively, of the ambient fluid. The drops are bounded by the contours C_1 and C_2 whose normal vector $\mathbf{n}$ points out of their volumes V_1 and V_2.

boundary-integral representation

$$\frac{1}{\eta}\int_S J_{ij}\sigma_{ik}n_k dS - \int_S u_i K_{ijk} n_k dS = \chi(\mathbf{x})u_j(\mathbf{x}) \tag{2.10}$$

where the arguments $(\mathbf{y})$ for n_k, σ_{ik}, u_i and $(\mathbf{y} - \mathbf{x})$ for J_{ij} and K_{ijk} have been suppressed to lighten the notation. In (2.10), the first integral, called the single-layer potential, represents the velocity given by a surface distribution of point forces with density $\sigma_{ik}n_k dS$. The second integral, called the double-layer potential, represents the velocity field induced by a superposition of sources, sinks and force dipoles. A detailed description of the two integrals can be found in Pozrikidis (1992).

2.2.1 2-D Boundary-integral representation of two fluid drops immersed in a fluid half-space

In the light of the boundary-integral representation (2.10), we derive here the integral representation of the system depicted in figure 2.5 that represents the basis of the subduction model we have developed for our work. In figure 2.5 we have two viscous drops immersed in a infinitely deep ambient fluid, bounded at the top by a free-slip surface. The force triggering the motion is the negative/positive

buoyancy of the two drops associated with their higher/lower density surplus with respect to the ambient fluid. All the other parameters describing the system are listed in the caption of figure 2.5.

We begin by writing the boundary-integral representation for each of the three fluid domains appearing in the model. According to eq. (2.10), it is:

for the fluid drop 1:

$$\frac{1}{\eta_1}\int_{C_1}\mathbf{J}(\mathbf{y}-\mathbf{x})\cdot\boldsymbol{\sigma}^{(1)}(\mathbf{y})\cdot\mathbf{n}(\mathbf{y})\,\mathrm{dl}(\mathbf{y})-\int_{C_1}\mathbf{u}^{(1)}(\mathbf{y})\cdot\mathbf{K}(\mathbf{y}-\mathbf{x})\cdot\mathbf{n}(\mathbf{y})\,\mathrm{dl}(\mathbf{y})= \\ =\chi_1(\mathbf{x})\mathbf{u}^{(1)}(\mathbf{x}), \tag{2.11}$$

for the fluid drop 2:

$$\frac{1}{\eta_2}\int_{C_2}\mathbf{J}(\mathbf{y}-\mathbf{x})\cdot\boldsymbol{\sigma}^{(2)}(\mathbf{y})\cdot\mathbf{n}(\mathbf{y})\,\mathrm{dl}(\mathbf{y})-\int_{C_2}\mathbf{u}^{(2)}(\mathbf{y})\cdot\mathbf{K}(\mathbf{y}-\mathbf{x})\cdot\mathbf{n}(\mathbf{y})\,\mathrm{dl}(\mathbf{y})= \\ =\chi_2(\mathbf{x})\mathbf{u}^{(2)}(\mathbf{x}), \tag{2.12}$$

and for the ambient fluid:

$$-\frac{1}{\eta_0}\int_{C_1}\mathbf{J}(\mathbf{y}-\mathbf{x})\cdot\boldsymbol{\sigma}^{(0)}(\mathbf{y})\cdot\mathbf{n}(\mathbf{y})\,\mathrm{dl}(\mathbf{y})-\frac{1}{\eta_0}\int_{C_2}\mathbf{J}(\mathbf{y}-\mathbf{x})\cdot\boldsymbol{\sigma}^{(0)}(\mathbf{y})\cdot\mathbf{n}(\mathbf{y})\,\mathrm{dl}(\mathbf{y})+ \\ +\int_{C_1}\mathbf{u}^{(0)}(\mathbf{y})\cdot\mathbf{K}(\mathbf{y}-\mathbf{x})\cdot\mathbf{n}(\mathbf{y})\,\mathrm{dl}(\mathbf{y})+\int_{C_2}\mathbf{u}^{(0)}(\mathbf{y})\cdot\mathbf{K}(\mathbf{y}-\mathbf{x})\cdot\mathbf{n}(\mathbf{y})\,\mathrm{dl}(\mathbf{y})=\chi_0(\mathbf{x})\mathbf{u}^{(0)}(\mathbf{x}). \tag{2.13}$$

We emphasize that $\mathbf{J}(\mathbf{y}-\mathbf{x})$ and $\mathbf{K}(\mathbf{y}-\mathbf{x})$ are the Green's function defined in (2.6), properly modified in order to satisfy the free-slip boundary condition at $x_2=0$.

Next, taking the linear combination λ_1(2.11) + λ_2(2.12) + (2.13) we obtain (Manga & Stone, 1993):

$$\chi_0(\mathbf{x})\mathbf{u}^{(0)}(\mathbf{x})+\chi_1(\mathbf{x})\lambda_1\mathbf{u}^{(1)}(\mathbf{x})+\chi_2(\mathbf{x})\lambda_2\mathbf{u}^{(2)}(\mathbf{x})= \\ =\frac{\Delta\rho_1}{\eta_0}\int_{C_1}(\boldsymbol{g}\cdot\mathbf{y})\mathbf{n}\cdot\mathbf{J}\mathrm{dl}+\frac{\Delta\rho_2}{\eta_0}\int_{C_2}(\boldsymbol{g}\cdot\mathbf{y})\mathbf{n}\cdot\mathbf{J}\mathrm{dl}+ \\ +(1-\lambda_1)\int_{C_1}\mathbf{u}^{(1)}\cdot\mathbf{K}\cdot\mathbf{n}\,\mathrm{dl}+(1-\lambda_2)\int_{C_2}\mathbf{u}^{(2)}\cdot\mathbf{K}\cdot\mathbf{n}\,\mathrm{dl}, \tag{2.14}$$

where $\Delta\rho_i=(\rho_i-\rho_0)$, with $i=1,2$, are the density differences and we drop the

arguments $(\mathbf{y})$ for $\mathbf{n}$, $\mathbf{u}^{(1)}$, $\mathbf{u}^{(2)}$ and $(\mathbf{y}-\mathbf{x})$ for $\mathbf{J}$ and $\mathbf{K}$ to simplify the notation. We also made use of the matching condition on the normal stress across the fluid/fluid interface

$$\left(\boldsymbol{\sigma}^{(0)} - \boldsymbol{\sigma}^{(i)}\right)\cdot\mathbf{n} = -\Delta\rho_i\,(\boldsymbol{g}\cdot\mathbf{y})\cdot\mathbf{n}, \quad (i = 1,2). \tag{2.15}$$

Finally, adopting the dimensionless variables

$$(\hat{\mathbf{x}},\hat{\mathbf{y}}) = a^{-1}(\mathbf{x},\mathbf{y}), \quad \hat{\mathbf{u}}^{(\mathbf{i})} = \frac{\eta_0}{a^2 g\Delta\rho_1}\mathbf{u}^{(i)} \quad (i = 1,2) \tag{2.16}$$

we rewrite eq. (2.14) in its dimensionless form (hat symbols suppressed):

$$\int_{C_1} -(\boldsymbol{e}_2\cdot\mathbf{y})\mathbf{n}\cdot\mathbf{J}\,\mathrm{dl} - \Gamma\int_{C_2}(\boldsymbol{e}_2\cdot\mathbf{y})\mathbf{n}\cdot\mathbf{J}\,\mathrm{dl} + (1-\lambda_1)\int_{C_1}\mathbf{u}^{(1)}\cdot\mathbf{K}\cdot\mathbf{n}\,\mathrm{dl} +$$
$$+(1-\lambda_2)\int_{C_2}\mathbf{u}^{(2)}\cdot\mathbf{K}\cdot\mathbf{n}\,\mathrm{dl} = \begin{cases} \mathbf{u}^{(0)}(\mathbf{x}) & \text{if} \quad \mathbf{x}\in V_0 \\ \lambda_1\mathbf{u}^{(1)}(\mathbf{x}) & \text{if} \quad \mathbf{x}\in V_1 \\ \lambda_2\mathbf{u}^{(2)}(\mathbf{x}) & \text{if} \quad \mathbf{x}\in V_2 \\ (1+\lambda_1)/2\ \ \mathbf{u}^{(1)}(\mathbf{x}) & \text{if} \quad \mathbf{x}\in C_1 \\ (1+\lambda_2)/2\ \ \mathbf{u}^{(2)}(\mathbf{x}) & \text{if} \quad \mathbf{x}\in C_2 \end{cases} \tag{2.17}$$

where $\mathbf{e}_2 = -\mathbf{g}/g$ is the (upward-pointing) vertical unit vector and $\Gamma \equiv \Delta\rho_2/\Delta\rho_1$. Equations (2.17) allow for a complete calculation of the flow field in the whole space domain. The first step is to compute the interfacial velocities $\mathbf{u}^{(1)}$ and $\mathbf{u}^{(2)}$ considering material points $\mathbf{x}\in C_1$ and $\mathbf{x}\in C_2$, for which (2.17) reduces to a pair of coupled Fredholm integral equations of the second kind. As $\mathbf{y}$ and $\mathbf{x}$ can lie on the same contour, the resolution of such a system requires the regularization of the corresponding integrals by 'subtracting the singularity' at $\mathbf{y} = \mathbf{x}$. According to Pozrikidis (1992), this procedure yields

$$\int_{C_i}(\mathbf{e}_2\cdot\mathbf{y})\mathbf{n}\cdot\mathbf{J}\,\mathrm{dl} = \int_{C_i}\mathbf{e}_2\cdot(\mathbf{y}-\mathbf{x})\mathbf{n}\cdot\mathbf{J}\mathrm{dl} \tag{2.18}$$

$$\int_{C_i}\mathbf{u}^{(i)}(\mathbf{y})\cdot\mathbf{K}\cdot\mathbf{n}\,\mathrm{dl} = \int_{C_i}[\mathbf{u}^{(i)}(\mathbf{y}) - \mathbf{u}^{(i)}(\mathbf{x})]\cdot\mathbf{K}\cdot\mathbf{n}\,\mathrm{dl} - \frac{1}{2}\mathbf{u}^{(i)}(\mathbf{x}) \tag{2.19}$$

where $i = 1,2$. Thus, we can write:

$$P_{11} = \int_{C_1} -[(x_{2y}) - (x_{2x})]\,\mathbf{n}\cdot(\mathbf{y})\mathbf{J}(\mathbf{y}-\mathbf{x})\mathrm{dl}(\mathbf{y}), \quad \text{for} \quad \mathbf{x}\in C_1 \wedge \mathbf{y}\in C_1 \tag{2.20a}$$

$$S_{21} = \int_{C_2} -(x_{2y})\mathbf{n}\cdot(\mathbf{y})\mathbf{J}(\mathbf{y}-\mathbf{x})\mathrm{dl}(\mathbf{y}), \quad \text{for} \quad \mathbf{x}\in C_1 \wedge \mathbf{y}\in C_2 \tag{2.20b}$$

$$Q_{11} = \int_{C_1} [\mathbf{u}(\mathbf{y}) - \mathbf{u}(\mathbf{x})]\cdot\mathbf{K}(\mathbf{y}-\mathbf{x})\cdot\mathbf{n}(\mathbf{y})\mathrm{dl}(\mathbf{y}) \quad \text{for} \quad \mathbf{x}\in C_1 \wedge \mathbf{y}\in C_1 \tag{2.20c}$$

$$D_{21} = \int_{C_2} \mathbf{u}(\mathbf{y})\cdot\mathbf{K}(\mathbf{y}-\mathbf{x})\cdot\mathbf{n}(\mathbf{y})\mathrm{dl}(\mathbf{y}) \quad \text{for} \quad \mathbf{x}\in C_1 \wedge \mathbf{y}\in C_2 \tag{2.20d}$$

$$S_{12} = \int_{C_1} -(x_{2y})\mathbf{n}\cdot(\mathbf{y})\mathbf{J}(\mathbf{y}-\mathbf{x})\mathrm{dl}(\mathbf{y}), \quad \text{for} \quad \mathbf{x}\in C_2 \wedge \mathbf{y}\in C_1 \tag{2.20e}$$

$$P_{22} = \int_{C_2} -[(x_{2y}) - (x_{2x})]\,\mathbf{n}(\mathbf{y})\cdot\mathbf{J}(\mathbf{y}-\mathbf{x})\mathrm{dl}(\mathbf{y}), \quad \text{for} \quad \mathbf{x}\in C_2 \wedge \mathbf{y}\in C_2 \tag{2.20f}$$

$$D_{12} = \int_{C_1} \mathbf{u}(\mathbf{y})\cdot\mathbf{K}(\mathbf{y}-\mathbf{x})\cdot\mathbf{n}(\mathbf{y})\mathrm{dl}(\mathbf{y}) \quad \text{for} \quad \mathbf{x}\in C_2 \wedge \mathbf{y}\in C_1 \tag{2.20g}$$

$$Q_{22} = \int_{C_2} [\mathbf{u}(\mathbf{y}) - \mathbf{u}(\mathbf{x})]\cdot\mathbf{K}(\mathbf{y}-\mathbf{x})\cdot\mathbf{n}(\mathbf{y})\mathrm{dl}(\mathbf{y}) \quad \text{for} \quad \mathbf{x}\in C_2 \wedge \mathbf{y}\in C_2 \tag{2.20h}$$

where eq. (2.18) and eq. (2.19) have been used when points $\mathbf{x}$ and $\mathbf{y}$ are on the same contour and we indicate with x_{2y} the vertical coordinate of the point $\mathbf{y}$ deriving from the dot product $\boldsymbol{e}_2\cdot\mathbf{y} = \boldsymbol{e}_2\cdot(x_1\boldsymbol{e}_1 + x_2\boldsymbol{e}_2)$. The same is valid for $\boldsymbol{e}_2\cdot\mathbf{x} \to x_{2x}$. Combining (2.20) and (2.17), we obtain

$$\begin{cases} P_{11} + \Gamma S_{21} + (1-\lambda_1)\left[Q_{11} - \dfrac{1}{2}\mathbf{u}^{(1)}(\mathbf{x})\right] + (1-\lambda_2)D_{21} = \dfrac{1+\lambda_1}{2}\mathbf{u}^{(1)}(\mathbf{x}) \\ S_{12} + \Gamma P_{22} + (1-\lambda_1)D_{12} + (1-\lambda_2)\left[Q_{22} - \dfrac{1}{2}\mathbf{u}^{(2)}(\mathbf{x})\right] = \dfrac{1+\lambda_2}{2}\mathbf{u}^{(2)}(\mathbf{x}). \end{cases} \tag{2.21}$$

Simplifying leads to the final formulation

$$\begin{cases} P_{11} + \Gamma S_{21} + (1-\lambda_1)Q_{11} + (1-\lambda_2)D_{21} = \mathbf{u}^{(1)}(\mathbf{x}) \\ S_{12} + \Gamma P_{22} + (1-\lambda_1)D_{12} + (1-\lambda_2)Q_{22} = \mathbf{u}^{(2)}(\mathbf{x}) \end{cases} \tag{2.22}$$

where the first equation of the system is obtained for $\mathbf{x}\in C_1 \wedge \mathbf{y}\in C_{1,2}$, while the second is for $\mathbf{x}\in C_2 \wedge \mathbf{y}\in C_{1,2}$. Once $\mathbf{u}^{(1)}$ and $\mathbf{u}^{(2)}$ are known, the velocity within the drops or in the ambient fluid can be determined if desired by solving the equations (2.17) for the regions of interest.

2.3 Thin viscous-sheet theory

A lithospheric plate is ≈ 100 Km thick and $\approx 1,000 - 10,000$ km wide. It moves and interacts with neighboring plates, deforming in a purely viscous manner on

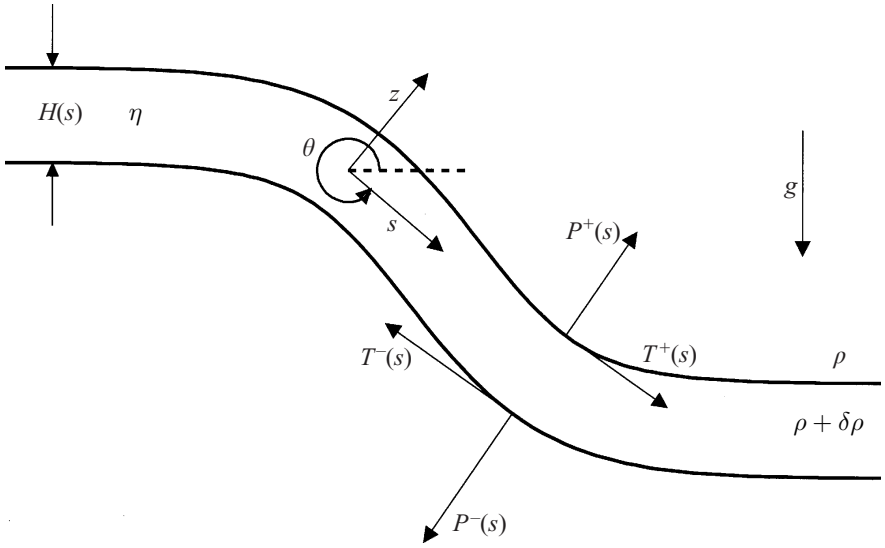

Figure 2.6. From Ribe (2001): Model of a two-dimensional thin sheet of viscous fluid with variable thickness $H(s)$, constant viscosity η and constant excess density $\delta\rho$. s and z define the local coordinate system related to the sheet's midsurface, located at $z = 0$. The midsurface has inclination $\theta(s)$ from the horizontal and curvature $K(s) = \mathrm{d}\theta/\mathrm{d}s$. In the most general case, inertialess flow in the sheet is driven both by its buoyancy and by externally applied normal $P^{\pm}(s)$ and tangential $T^{\pm}(s)$ stresses.

geological time scales. Due to these features, its long-term and large-scale dynamics can be investigated with the help of thin viscous-sheet theory (England & McKenzie, 1982, 1983; Ribe, 1992; Weinstein & Olson, 1992; Ribe, 2001, 2002). In this section I will show several results that have been systematically adopted in this thesis. For further details, refer to Ribe (2001).

2.3.1 Exact governing equations

Figure 2.6 shows a characteristic 2-D configuration of a thin sheet of a highly viscous fluid. The sheet is assumed Newtonian, with a constant viscosity η, and is denser by an amount $\delta\rho$ than the ambient fluid in which it is immersed. It has thickness $H(s)$, variable along the arclength coordinate s of the sheet's midsurface, and it extends over a characteristic horizontal length scale L, such that $\varepsilon \equiv H/L \ll 1$, where ϵ defines the slenderness of the sheet. The $s-$ and $z-$directions constitute the local reference frame relative to the sheet's midusrface which lies at $z = 0$, halfway between the sheet's upper and lower surfaces. The midsurface has inclination $\theta(s)$ from the horizontal and curvature $K(s) = \mathrm{d}\theta/\mathrm{d}s$. The inertialess flow within the sheet has tangential component $u(s, z)$ and normal component $w(s, z)$. The velocities at the midsurface are $U(s) = u(s, 0)$ and $W(s) = w(s, 0)$. In the most general case, the creeping flow within the sheet is driven both by its buoyancy

and by extrenally applied normal $P^{\pm}(s)$ and tangential $T^{\pm}(s)$ stresses. The exact equations governing its motion are

$$\frac{\partial u}{\partial s} + \frac{\partial}{\partial z}(hw) = 0 \tag{2.23a}$$

$$\frac{\partial \sigma_{ss}}{\partial s} + \frac{\partial}{\partial z}(h\sigma_{zs}) + \sigma_{zs}\frac{\partial h}{\partial z} = -hg_s\delta\rho \tag{2.23b}$$

$$\frac{\partial}{\partial z}(h\sigma_{zz}) + \frac{\partial \sigma_{zs}}{\partial s} - \sigma_{ss}\frac{\partial h}{\partial z} = -hg_z\delta\rho \tag{2.23c}$$

where σ_{ij} is the stress tensor. Its components are

$$\sigma_{ss} = -p + \frac{2\eta}{h}\left(\frac{\partial u}{\partial s} - Kw\right), \quad \sigma_{zz} = -p + 2\eta\frac{\partial w}{\partial z}, \tag{2.24a}$$

$$\sigma_{zs} = \eta\left[\frac{1}{h}\frac{\partial w}{\partial s} + h\frac{\partial}{\partial z}\left(\frac{u}{h}\right)\right], \tag{2.24b}$$

where $h = 1 - zK$ and $g_s\mathbf{s} + g_z\mathbf{z} = -g(\mathbf{s}\sin\theta + \mathbf{z}\cos\theta)$, where $\mathbf{s}$ and $\mathbf{z}$ are unit vectors in the s- and z- directions.

Assuming for simplicity that the forces exerted on the sheet by the ambient fluid are negligible relative to the bouyancy force, we integrate the momentum equations (2.23b) and (2.23c) across the sheet, obtaining the global force balances

$$\frac{dN}{ds} - KQ = -Hg_s\delta\rho \tag{2.25a}$$

$$\frac{dQ}{ds} + KN = -Hg_z\delta\rho, \tag{2.25b}$$

where

$$N = \int_{-H/2}^{H/2}\sigma_{ss}dz, \quad Q = \int_{-H/2}^{H/2}\sigma_{zs}dz \tag{2.26}$$

are the 'resultants' of the fibre stress σ_{ss} and the shear stress σ_{zs}, respectively. Next, multypling (2.23b) by z and then integrating, we get an expression describing the global torque balance

$$\frac{dM}{ds} - Q = \frac{1}{12}KH^3g_s\delta\rho \quad \Rightarrow \quad \frac{dM}{ds} \approx Q \tag{2.27}$$

where we have used $KH \ll 1$. The quantity M is the first moment of the fibre stress

$$M = \int_{-H/2}^{H/2} z\sigma_{ss}dz, \tag{2.28}$$

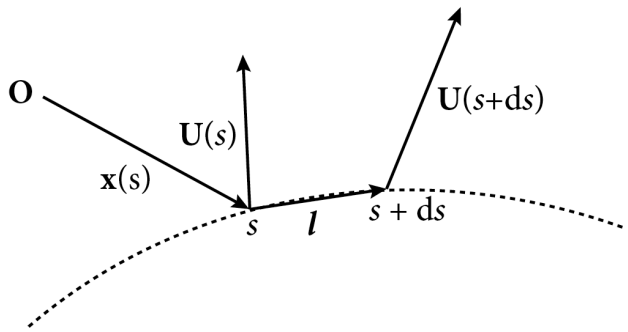

Figure 2.7. Time evolution of two material points on the sheet's midsurface, belonging to the midsurface element **l**. Credits: Neil M. Ribe.

which represents the sheet's bending moment. By analogy with the above expression, we refer to N of eq. (2.26), the "zeroth" moment of $\sigma_{ss}(z)$, as the sheet's stretching moment.

2.3.2 Midsurface kinematics and constitutive relations for N and M

Thin-sheet theory is based on the insight that characterizing the deformation of its midsurface suffices to understand the deformation of the whole sheet. This means that the stretching (N) and the bending (M) moments defined in the previous paragraph can be expressed in terms of the midsurface velocities $U(s)$ and $W(s)$ and their arcwise derivatives. To understand how the midsurface deforms we look at figure 2.7. The sketch shows the evolution of two endpoints of a line element **l** on the midsurface, evolving from the position $x(s)$ and $x(s)+\mathbf{l}$ at $t=0$ to the position $x(s)+\mathbf{U}(s)\mathrm{d}t$ and $x(s)+\mathbf{l}+\mathbf{U}(s+\mathrm{d}s)\mathrm{d}t$ at the new time $t+\mathrm{d}t$, where $\mathbf{U}=U\mathbf{s}+W\mathbf{z}$ represents the midsurface velocity vector. The variation of the midsurface element $\mathrm{d}\mathbf{l}$ is thus

$$\mathrm{d}\mathbf{l}=[\mathbf{U}(s+\mathrm{d}s)-\mathbf{U}(s)]\mathrm{d}t \tag{2.29}$$

which when divided by $\mathrm{d}s$ and $\mathrm{d}t$ becomes

$$\frac{1}{|\mathbf{l}|}\frac{\mathrm{d}\mathbf{l}}{\mathrm{d}t}=\frac{\mathbf{U}(s+\mathrm{d}s)-\mathbf{U}(s)}{\mathrm{d}s}\equiv\mathbf{U}'\equiv(U\mathbf{s}+W\mathbf{z})', \tag{2.30}$$

where $|\mathbf{l}|=\mathrm{d}s$ and a prime indicates a derivative with respect to arclength $\mathrm{d}/\mathrm{d}s$. Noting further that the unit vectors $\mathbf{s}$ and $\mathbf{z}$ vary as $\mathbf{s}'=K\mathbf{z}$ and $\mathbf{z}'=-K\mathbf{s}$, we can

expand the derivatives in. (2.30) obtaining

$$\frac{1}{|\mathbf{l}|}\frac{\mathrm{d}\mathbf{l}}{\mathrm{d}t} = \Delta\mathbf{s} + \omega\mathbf{z} \tag{2.31}$$

where

$$\Delta \equiv U' - KW, \quad \omega \equiv W' + KU. \tag{2.32}$$

The parameters Δ and ω are the basic quantities that characterize the midsurface deformation. Specifically, Δ measures the rate of stretching of the midsurface while ω measures its rate of rotation.

With the definitions (2.32) in hand, we seek now for the constitutive relations describing the stretching (N) and the bending (M) moments of a thin viscous sheet. We begin by assuming that the deformation of the thin sheet is dominated by the component σ_{ss} of the stress tensor, such that σ_{sz} and σ_{zz} can be neglected and set to zero. Recalling the definitions given in (2.24), the first hypothesis $\sigma_{sz} = 0$ implies

$$\frac{\partial}{\partial z}\left(\frac{u}{h}\right) = -\frac{1}{h^2}\frac{\partial w}{\partial s}. \tag{2.33}$$

Setting $w = W(s)$ on the RHS of (2.33) and considering the first-order Taylor expansion of h^{-2} around the point $z = 0$,

$$h^{-2} = \frac{1}{1 - 2zK - (zK)^2} \approx 1 + 2zK + \mathcal{O}(zK)^2, \tag{2.34}$$

eq. (2.33) becomes

$$\frac{\partial}{\partial z}\left(\frac{u}{h}\right) = -W'(1 + 2zK). \tag{2.35}$$

Now we integrate (2.35) subject to $u(0) = U$ and keep only terms that are linear in z, to obtain

$$u = U - (W' + KU)z + \mathcal{O}(z^2) \equiv U - \omega z. \tag{2.36}$$

The next step is to exploit the vanishing of $\sigma_{zz} = 0$ to get an expression for the pressure

$$p = 2\eta\frac{\partial w}{\partial z}. \tag{2.37}$$

From the continuity equation (2.23a), we find

$$\frac{\partial w}{\partial z} = \frac{Kw - \partial u/\partial s}{h}. \tag{2.38}$$

As done before, we set $w = W(s)$ on the RHS of the equation and, noticing that $h^{-1} \approx 1 + zK + \mathcal{O}(zK)^2$, we obtain

$$\frac{\partial w}{\partial z} = (KW - \partial u/\partial s)(1 + zK). \tag{2.39}$$

Finally, using (2.36) for $\partial u/\partial s$ and dropping the quadratic terms in z we get

$$\frac{\partial w}{\partial z} = -\Delta(1 + zK) + \omega' z + \mathcal{O}(z^2) \equiv -\Delta(1 + zK) + \omega' z, \tag{2.40}$$

which when substituted in (2.37) yields

$$p = 2\eta\left[-\Delta(1 + zK) + \omega' z\right]. \tag{2.41}$$

We can now use (2.41) and (2.36) in the expression for σ_{ss}, obtaining

$$\begin{aligned}
\sigma_{ss} &= -p + \frac{2\eta}{h}\left(\frac{\partial u}{\partial s} - Kw\right) \\
&\approx -p + 2\eta\left(\frac{\partial u}{\partial s} - KW\right)(1 + zK) && (2.42)\\
&\approx 4\eta(1 + zK)\Delta - 4\eta\omega' z + \mathcal{O}(z^2). && (2.43)
\end{aligned}$$

Thus, the stretching and the bending moments of the thin viscous sheet are

$$N = \int_{-H/2}^{H/2} \sigma_{ss} dz \approx 4\eta H\Delta \tag{2.44a}$$

$$M = \int_{-H/2}^{H/2} z\sigma_{ss} dz \approx -\frac{\eta H^3}{3}(\omega' - K\Delta) \equiv -\frac{\eta H^3}{3}\dot{K}, \tag{2.44b}$$

where we introduce in (2.44b) the 'curling rate' $\dot{K}$, which measures the rate of change of curvature of the sheet's midsurface.

2.3.3 Viscous dissipation and bending length

Viscous sheets deform by some combination of bending and stretching. For some applications such as subduction modeling, it is interesting to understand which mechanism of deformation dominates. This can be done by calculating separately the rates of energy dissipation associated with deformation by bending and

Table 2.1. Complete set of equations for an evolving thin viscous sheet.

Force balance:	$N' - KQ = -Hg_s\delta\rho$, $Q' + KN = -Hg_z\delta\rho$
Torque balance:	$M' = Q$
Midsurface kinematics:	$\Delta = U' - KW$, $\omega = W' + KU$, $\dot{K} = \omega' - K\Delta$
Stretching moment:	$N = 4\eta H\Delta$
Bending moment:	$M = -\left(\eta H^3\dot{K}\right)/3$
Viscous dissipation due to stretching:	$\phi_s = 4\eta H\Delta^2$
Viscous dissipation due to bending:	$\phi_b = \left(\eta H^3\dot{K}^2\right)/3$
Evolution of the midsurface shape:	$\mathrm{D}\mathbf{x}/\mathrm{D}t = U\mathbf{s} + W\mathbf{z}$
Evolution of the thickness:	$\mathrm{D}H/\mathrm{D}t = -H\Delta$

stretching. Given the thin sheet approximation and the consequent negligible contribution of shear strains to the dissipation, the calculation turns out to be quite simple. In fact, taking into account the energy balance of an inertialess flow (1.11) and given the expression for e_{ss} that one obtains from (2.42), the dissipation rate per unit volume of the sheet is to lowest order

$$4\eta e_{ss}^2 \approx 4\eta\left(\Delta - z\dot{K}\right)^2. \tag{2.45}$$

Integrating (2.45) across the sheet, we obtain the dissipation rate per unit area of the midsurface

$$\phi(s) = \frac{1}{3}\eta H^3\dot{K}^2 + 4\eta H\Delta^2 = \phi_b + \phi_s, \tag{2.46}$$

which is the sum of two contributions associated with deformation by bending (ϕ_b) and stretching (ϕ_s). Eq. (2.46) is the last expression we need in order to fully characterize the dynamics of a thin viscous sheet. The complete set of thin-sheet equations obtained in the present section is summarized in table 2.1. The derivation of the last two expressions describing the evolution of the sheet's geometry can be found in § 6 of Ribe (2001).

To conclude this chapter we show how we can exploit the formula for the bending moment to determine the crucial length scale characterizing the bending

response of a subducting lithospheric plate. Indeed, equation (2.44b) shows that $M(s) \sim \dot{K}(s)$. Therefore, we might compute $\dot{K}(s)$ along the sheet's midsurface in order to see if the bending moment concentrates in some specific portion of the sheet. This is done in figure 2.8a, which refers to the subduction model investigated in Ribe (2010). The figure reports the variation of the normalized curling rate $\dot{K}$ as a function of the dimensionless arclength s/h of a subducting sheet whose thickness is h. Each curve refers to a particular value of the viscosity ratio (γ) between the subducting sheet and the surrounding fluid. The plot clearly highlights that there is a zone along the midsurface where the function $\dot{K}$ is much higher than in the rest. This is the portion of the sheet where significant bending occurs, and its characteristic length scale is called the'bending length' ℓ_b (Ribe, 2010). Its precise mathematical definition is illustrated in figure 2.8a for the case $\gamma = 10^2$: it is the distance from the rightmost end of the sheet's midsurface to the first zero of $\dot{K}(s)$ to the left of the point where this function has its global minimum. In geodynamical terms, ℓ_b is the sum of the slab length plus the length of the region seaward of the trench where flexural bulging occurs (figure 2.8b). The important point here is that the bending length ℓ_b is the proper length scale characterizing the bending response of a subducting plate deforming under the action of gravity. This follows from the fact that unlike in an elastic body, where M is proportional to the local curvature K, in a viscous sheet M is proportional to the rate of change of the curvature $\dot{K}$. In the elastic case, the bending response is properly described by a purely geometric length scale such as the minimum radius of curvature ($R_{\min}$ in figure 2.8b). On the contrary, in the viscous case we need a 'dynamic' length scale as the bending length which arises only after we actually solve the equations describing the system. For more details on this last argument, refer to § 8 of Ribe (2010).

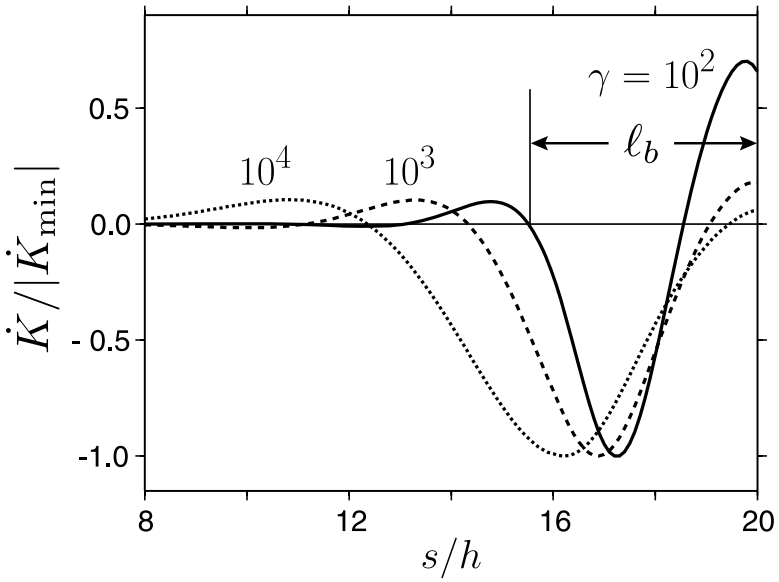

(a) From Ribe (2010): Normalized curling rate $\dot{K}$ plotted against the dimensionles arclength s/h, where h is the sheet's thickness. The three curves refer to different setups of the subduction model presented in the paper which differ only in the value of the vicosity ratio γ between the subducting sheet and the surrounding fluid. The latter is reported beside each curve. The definition of the bending length ℓ_b is indicated for the case $\gamma = 10^2$.

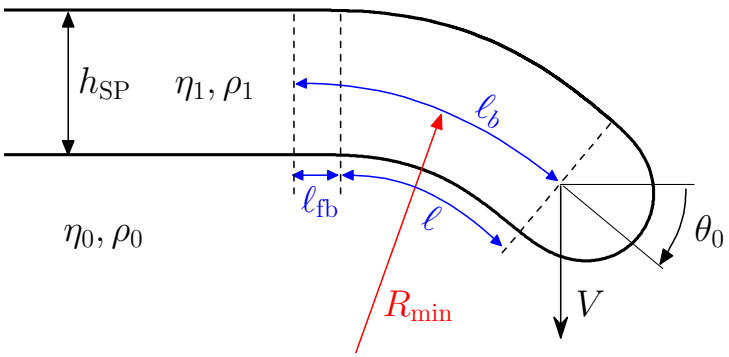

(b) Sketch of the leading end of a subducting viscous sheet characterized by a slab of length ℓ, an angle of subduction θ_0 and a characteristic sinking speed V. In blue is highlighted the bending length ℓ_b, the sum of the slab length ℓ and of the length ℓ_{fb} of the region seaward of the trench where flexrual bulging occurs. The red line shows the minimum radius of curvature $R_{\min}$ of the sheet's midsurface.

Figure 2.8. Mathematical (a) and geodynamical (b) definitions of the bending length ℓ_b in a subducting viscous sheet.

Chapter 3

Mechanics of subduction

This chapter contains the results published in: Gerardi G. and Ribe N. M. Boundary Element Modeling of Two-Plate Interaction at Subduction Zones: Scaling Laws and Application to the Aleutian Subduction Zone. *Journal of Geophysical Research: Solid Earth*, 123(6):5227-5248, 2018. The outline of the chapter follows the one of the paper. The 'Introduction' section has been omitted in order to avoid redundancy.

Here we investigate the mechanics underlying the phenomenon of subduction using a 2-D numerical model of free subduction in which a Subducting Plate (SP) and an Overriding Plate (OP) interact across a relatively weak interface. After introducing the model setup and the numerical technique adopted in the work (the Boundary Element Method, BEM), we set the stage with an overview of time-dependent subduction without (SP Only case) and with (SP+OP case) an OP. This section makes clear the critical influence of the subduction interface strength which, unlike many previous studies (e.g. van Hunen *et al.*, 2000; Babeyko & Sobolev, 2008; Rodríguez-González *et al.*, 2012; Holt *et al.*, 2015), is treated here as a variable. Next, we exploit the quasi-static character of Stokes flow to examine instantaneous solutions of the model equations, for both the SP Only and the SP+OP cases. A key result here is that the surface speed of the SP always depends logarithmically on the ratio of the surface plate length to the slab length. We also determine a scaling law for the convergence rate of the sinking slab as a function of the flexural stiffness of the SP and the dimensionless subduction interface thickness. We then turn to an analysis of the deformation state of the OP, using instantaneous BEM solutions interpreted in terms of thin viscous-sheet theory. These solutions show that the deformation of the OP is dominated by compression, bending, and (in some cases) extension as one moves from the forearc to the backarc region. Finally, we apply our results by using BEM solutions with realistic geometry to infer the long-term strength of the subduction interface in

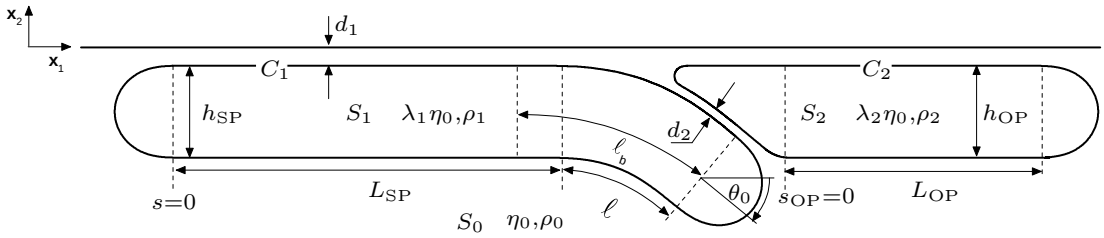

Figure 3.1. 2D model geometry of free subuduction of a dense subducting plate (SP) with viscosity $\eta_1 = \lambda_1\ \eta_0$ and density ρ_1 beneath an overriding plate (OP) with viscosity $\eta_2 = \lambda_2\ \eta_0$ and density ρ_2 in an ambient fluid with viscosity η_0 and density ρ_0. The ambient fluid is infinitely deep and is bounded at x_2=0 by a free-slip surface. The arclength coordinate along the SP's midsurface is $s \in [0, L_{\rm SP} + \ell]$, while it is $s_{\rm OP} \in [0, L_{\rm OP}]$ for the OP arclength coordinate. The symbol ℓ_b identifies the 'bending length' of the SP, equal to the sum of the slab length and the length of the seaward portion of the SP where flexural bulging occurs (see section 2.3.3 for more details).

the central Aleutian subduction zone.

3.1 Model setup

Figure 3.1 shows the initial configuration ($t = 0$) of the model, and table 3.1 summarizes the notation adopted. The domain is 2D, infinitely deep and bounded at $x_2 = 0$ by a free-slip surface (i.e. impermeable and free of shear traction). Two thin sheets are immersed in the ambient fluid half-space. Their cross-sectional areas are S_1, S_2 and their interfacial contours are C_1, C_2, respectively, where the subscript 1 represents the SP and 2 the OP.

The viscosity of the SP is $\eta_1 = \lambda_1\ \eta_0$, where η_0 is the ambient fluid viscosity. Its density is $\rho_1 = \rho_0 + \Delta\rho_1$, where ρ_0 is the ambient fluid density and $\Delta\rho_1 > 0$ is the density excess of the SP relative to the ambient fluid. The viscosity of the OP is $\lambda_2\eta_0$ and its density ρ_2 can be equal or smaller than ρ_0, depending on whether the OP is neutrally or positively buoyant, respectively.

The SP comprises a flat portion of length $L_{\rm SP}$ and a bent piece (the slab) of length ℓ whose leading end subducts with an initial angle θ_0. The plate has a constant thickness $h_{\rm SP}$ except for the two rounded ends. The SP's midsurface lies halfway between its upper and lower surfaces, and the arclength coordinate along the midsurface is $s \in [0, L_{\rm SP} + \ell]$. At $t = 0$, the shape of the slab's midsurface is analytically specified by its dip $\theta(s)$, given by

$$\theta(s) = \theta_0 \hat{s}^2 \left(3\ell - 2\hat{s}\right) / \ell^3 \tag{3.1}$$

where $\hat{s} = s - L_{\rm SP}$. Eq. (3.1) ensures that the midsurface curvature $K(s) = -\mathrm{d}\theta/\mathrm{d}s$

Table 3.1. Notation

Variable	Definition	Units
d_1	Lubrication layer thickness above the plates	[m]
d_2	Lubrication layer thickness between the plates	[m]
h_{SP}	SP thickness	[m]
h_{OP}	OP thickness	[m]
L_{SP}	SP length	[m]
L_{OP}	OP length	[m]
ℓ	Slab length	[m]
θ_0	Initial dip of the slab's tip	[-]
s	Arclength coordinate along SP midsurface	[m]
s_{OP}	Arclength coordinate along OP midsurface	[m]
C_1	SP contour	[m]
C_2	OP contour	[m]
S_1	SP area	[m^2]
S_2	OP area	[m^2]
η_0	Ambient fluid viscosity	[Pa s]
ρ_0	Ambient fluid density	[kg m^{-3}]
ρ_1	SP density	[kg m^{-3}]
η_1	SP viscosity	[Pa s]
λ_1	$\equiv \eta_1/\eta_0$; SP viscosity contrast	[-]
ρ_2	OP density	[kg m^{-3}]
η_2	OP viscosity	[Pa s]
λ_2	$\equiv \eta_2/\eta_0$; OP viscosity contrast	[-]
ℓ_b	Bending length	[m]

is initially zero at both $s = L_{\mathrm{SP}}$ and $s = L_{\mathrm{SP}} + \ell$.

The OP comprises at $t = 0$ a central flat portion with constant thickness h_{OP} and length L_{OP}, bounded on the right by a rounded end and on the left by a triangular portion separated from the SP by a gap (lubrication layer) of constant width d_2. The exact shape of the triangular piece depends on the choice of ℓ and d_2. Sharp corners that could reduce the accuracy of the numerical method are avoided by rounding two of the corners of the triangular piece. The arclength coordinate on the OP's midsurface is $s_{\mathrm{OP}} \in [0, L_{\mathrm{OP}}]$.

Referring again to figure 3.1, we point out that another lubrication layer of thickness d_1 is present above the SP and the OP. Its role is to allow an 'earthlike' lateral movement of the plates. According to lubrication theory, strong normal stresses develop in the thin layer and resist the vertical motion of the plates when they are subjected to a vertical force. In the case of the negatively buoyant SP, an upward-directed normal stress $\sim h_{\mathrm{SP}} g \Delta\rho_1$ is set up in the layer and exactly compensates the negative buoyancy of the flat portion of the plate, which is then

free to move laterally in response to slab pull (Ribe, 2010). The situation is opposite for a positively buoyant OP: downward-directed normal stresses $\sim h_{\mathrm{OP}} g \Delta\rho_2$ prevent the OP from rising towards the free-slip surface, and allow it to deform freely in response to its buoyancy and the influence of the nearby slab.

3.2 BEM formulation

Because inertia is negligible in the mantle, the flow within the plates and outside them is governed by the Stokes equation of motion. Stokes flow problems with deformable fluid/fluid interfaces can be efficiently solved using the boundary-element method (BEM). This numerical technique is based on the boundary-integral representation of Stokes flow derived in § 2.2. The method is especially well adapted to tracking fluid-fluid interfaces having continuous curvature, like the ones shown in figure 3.1. The BEM has several advantages: unwanted wall effects are entirely absent, the dimensionality of the problem is reduced by one (from 2-D to 1-D in our case), and it is easy to obtain high (fourth-order) accuracy of the solutions for the velocity at each time step.

The model problem sketched in figure 3.1 comprises three distinct fluid regions, two of which are singly connected. For this geometry, the (dimensionless) boundary-integral representation of the flow is the one given in eq. (2.17), where the dimensionless variables are now defined as follows:

$$(\hat{\mathbf{x}}, \hat{\mathbf{y}}) = h_{\mathrm{SP}}^{-1}(\mathbf{x}, \mathbf{y}), \quad \hat{\mathbf{u}}^{(i)} = \frac{\eta_0}{h_{\mathrm{SP}}^2 g \Delta\rho_1} \mathbf{u}^{(i)} \quad (i = 1, 2). \tag{3.2}$$

When interested in time dependent solutions, we advance in time the material points $\mathbf{x} \in C_1$ and $\mathbf{x} \in C_2$ according to:

$$\frac{\mathrm{d}\mathbf{x}}{\mathrm{d}t} = \mathbf{u}(\mathbf{x}) \tag{3.3}$$

where the dimensionless time is

$$\hat{t} = \frac{h_{\mathrm{SP}} g \Delta\rho_1}{\eta_0} t. \tag{3.4}$$

As described in § 2.2.1, in order to obtain the flow field of our subduction model, we first need to compute the interfacial velocities of the plates solving the coupled integral equations (2.22). For the numerical resolution, the contours C_1 and C_2 are discretized using three-node curved elements $C_{n_1} (n_1 = 1, 2, ..., N_1)$ and

$C_{n_2}(n_2 = 1, 2, ..., N_2)$, over each of which $\mathbf{y}$, $\mathbf{n}$ and $\mathbf{u}$ vary as

$$\mathbf{y}(\xi) = \sum_{m=1}^{3} \phi_m(\xi)\mathbf{y}_m, \quad \mathbf{n}(\xi) = \frac{\partial_\xi \mathbf{y} \times \mathbf{e}_3}{|\partial_\xi \mathbf{y} \times \mathbf{e}_3|},$$
$$\mathbf{u}(\xi) = \sum_{m=1}^{3} \phi_m(\xi)\mathbf{u}_m, \tag{3.5}$$

where $\mathbf{y}_m$ are the (known) nodal coordinates, $\mathbf{u}_m$ are the (unknown) nodal velocities and $\phi_m(\xi)$ are quadratic basis functions defined on a master element $\xi \in [-1, 1]$. Substitution of (3.5) into (2.22) transforms the integrals over C_1 and C_2 into sums over the elements C_{n_1} and C_{n_2}, each of which is evaluated on $\xi \in [-1, 1]$ using 6-point Gauss-Legendre quadrature. The resulting system of $4(N_1+N_2)$ coupled linear equations is solved iteratively using the biconjugate gradient algorithm of Press *et al.* (1992), yielding the nodal velocities $\mathbf{u}_m$ with fourth-order-accuracy. Finally, the evolution in time of the shape of the plates is obtained by solving (3.3) with a second-order Runge-Kutta (midpoint) method.

We emphasize that the element size (mesh resolution) is variable along the two contours, being smaller along the portions that adjoin the thin lubrication layers. This is done in order to avoid the loss of numerical accuracy that occurs when the distance between the observation point $\mathbf{y}$ and the source point $\mathbf{x}$ of the Green's functions is smaller then the element size (see Appendix C for more details).

To test the accuracy of the model, we ran simulations for a geometry comprising two effectively solid ($\lambda_1 = \lambda_2 = 10^5$) cylinders of radius R with $\Gamma = 1$, located at the same depth and separated by a horizontal distance d_2. We computed the horizontal (u_1) and vertical (u_2) components of the velocity of the cylinders as well as their spin ω, as functions of increasing d_2. In the limit $d_2/R \gg 1$, $u_1 \to 0$ and $\omega \to 0$, and u_2 approaches the prediction of the analytical solution of Wakiya (1975) for a solid cylinder sinking normal to a free-slip surface.

3.3 Unsteady subduction

We begin our study with an overview of the qualitative features of the temporal evolution of the system. For reference, we first examine the unsteady subduction of an isolated SP (from now on the SP ONLY case), adding the OP later to see how its presence influences the dynamics. We shall refer to the latter case as the SP+OP case.

Figure 3.2 shows the initial and final states of three simulations starting from initial configurations given in table 3.2. Figure 3.2a shows the subduction of an isolated SP to $\hat{t} = 21.5$, at which time the slab's tip is at a depth $6.8h_{SP}$

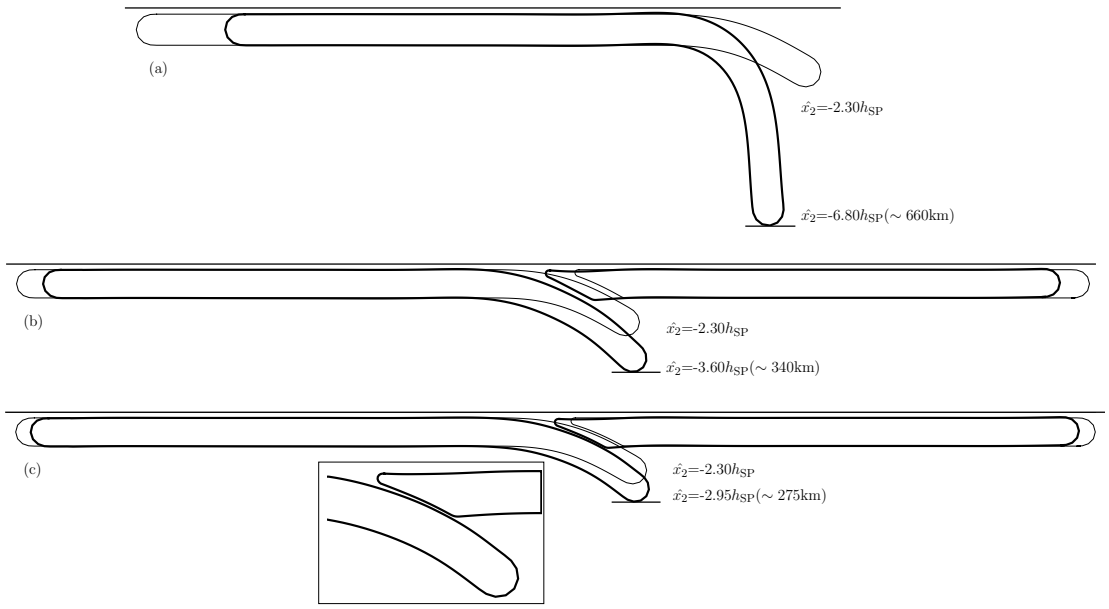

Figure 3.2. Time evolution of free subduction for different configurations: (a) SP ONLY case, (b) SP+OP case with d_2/h_{SP}=0.2, (c) SP+OP case with d_2/h_{SP}=0.08. In all cases the thin solid line represents the initial configuration of the system specified in table 3.2, while the thick solid line corresponds to the final state of the sheets at the dimensionless time $\hat{t} = t h_{SP} g \Delta\rho_1/\eta_0 = 21.5$. The vertical coordinate $\hat{x}_2$ of the deepest point on the slab and its equivalent in km are indicated. The inset of (c) is a zoomed-in view of the final state of the system.

(corresponding to a dimensional depth 660 km for h_{SP} = 100 km and $d_1/h_{SP} = 0.2$.) We then add the OP and run the simulation for the same dimensionless time $\hat{t} = 21.5$. The cases shown in figs. 3.2b and 3.2c differ only in the thickness d_2 of the lubrication layer between the plates, which is $0.2h_{SP}$ for the former case and $0.08h_{SP}$ for the latter.

Comparing the SP ONLY case and both SP+OP cases, we immediately see that the presence of the OP leads to an overall slowing down of the subduction process, as indicated by the reduced convergence rate and trench rollback speed. Moreover, the slowing-down is more pronounced for the smaller lubrication gap thickness. This is indicated by the depths reached by the slabs at $\hat{t} = 21.5$, which

Table 3.2. Initial configurations

	SP				OP				
	θ_0	L_{SP}/h_{SP}	ℓ/h_{SP}	λ_1	d_2/h_{SP}	L_{OP}/h_{SP}	h_{OP}/h_{SP}	λ_2	Γ
figure 3.2a	30°	16	5	300	-	-	-	-	-
figure 3.2b	30°	16	5	300	0.2	16	1	300	-0.25
figure 3.2c	30°	16	5	300	0.08	16	1	300	-0.25

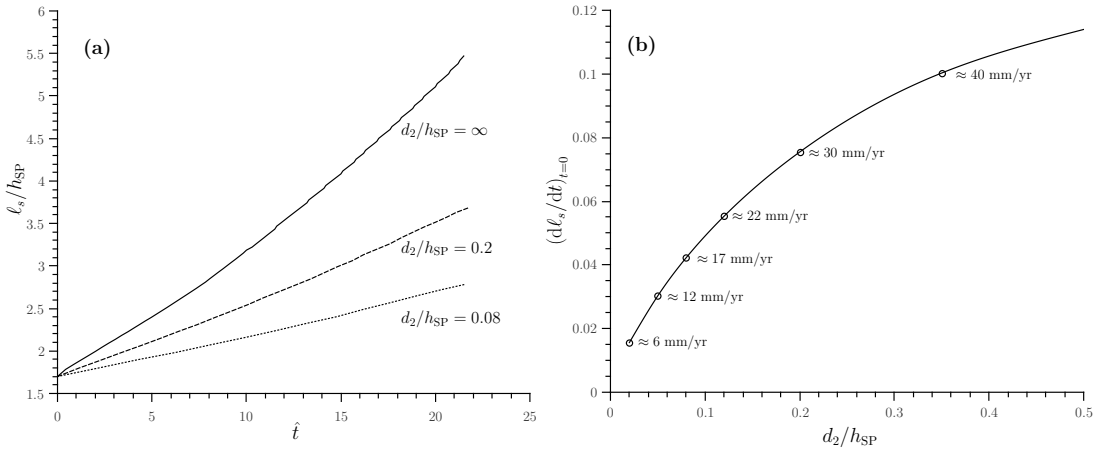

Figure 3.3. Dependence of the convergence rate on the the thickness of the subduction interface. (a) Subducted length ℓ_s of the midsurface of the SP as a function of time for the three cases of fig. 3.2. The values of d_2/h_{SP} indicated are initial values (t = 0). (b) Instanstaneous convergence rate of the initial configuration as a function of the dimensionless gap width d_2/h_{SP}. The dimensional convergence rates indicated are calculated from eq. (3.2) assuming h_{SP} =100 km, $\eta_0 = 5.44 \times 10^{20}$ Pa s, and $\Delta\rho_1$ = 70 kg m^{-3}.

are 340 km for d_2/h_{SP}=0.2 and 275 km for d_2/h_{SP}=0.08. Furthermore, the OP moves seaward as subduction proceeds, indicating the strong mechanical coupling of the OP and the SP across the lubrication gap separating them.

A useful parameter for illustrating the evolution of subduction is the length ℓ_s of the sheet's midsurface that is below the depth $x_2 = -h_{SP} - d_1$ of the base of the plate. The derivative $d\ell_s/dt$ is then the instantaneous convergence rate. Figure 3.3(a) shows $\hat{\ell}_s = \ell_s/h_{SP}$ for the three cases of figure 3.2. The convergence rate is an increasing function of d_2 at all times. This reflects the influence of the viscous drag exerted on the SP by the subduction interface, which increases as d_2 decreases for a given magnitude of the relative tangential velocity between the SP and the OP. The subduction interface drag force works against the slab pull, leading to slower subduction. This effect is emphasized in figure 3.3b, which shows the instantaneous convergence rate $(d\ell_s/dt)_{t=0}$ at the initial time as a function of the dimensionless thickness of the subduction interface. The convergence rate strongly decreases as the subduction interface becomes thinner.

The dominant role of the parameter d_2/h_{SP} becomes even clearer if we examine the influence of the geometry and physical properties of the OP on the evolution of ℓ_s. To do so, we fix the value of d_2/h_{SP} = 0.2 and we explore indivdually the effect of the OP length $L_{OP}/h_{SP} \in [8-32]$, of its thickness $h_{OP}/h_{SP} \in [0.75-1.25]$, of its viscosity $\lambda_2 \in [150-600]$ and of its density $\Gamma \in [-0.5-0]$. It arises that all the different curves $\ell_s(t)$ remain identical to the one depicted in fig. 3.3(a), thus

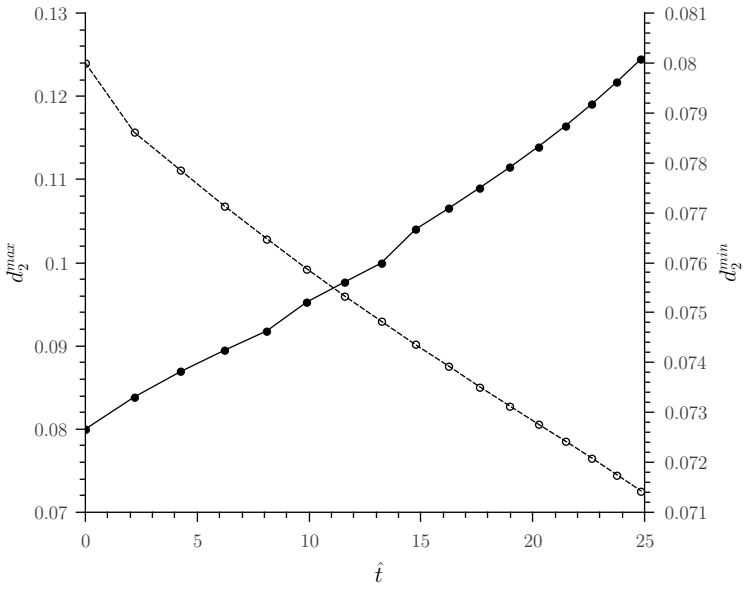

Figure 3.4. Time evolution of the minimum (dashed line-right axis) and maximum (solid line-left axis) thickness for the model of fig. 3.2c.

proving that none of the OP properties listed above have any consequence on the convergence rate. Only the thickness h_{OP} shows a certain effect for long times ($\hat{t} \geq 10$), with a higher value of h_{OP} resulting in a lower value of the subducted length $\hat{\ell}_s$ and viceversa. However, this variation is small (2-3%) compared to the effect of varying d_2/h_{SP}, which is therefore the dominant parameter controlling $\ell_s(t)$.

To conclude this section, we highlight an interesting feature of the geometry of the lubrication gap at the end of our SP+OP simulations. While the gap initially has a constant thickness d_2, it evolves during subduction so that it is narrower at the bottom than at the top (inset of 3.2c). This aspect is quantified in figure 3.4 where we track the time evolution of the maximum ($d_2^{\max}$) and minimum ($d_2^{\min}$) thickness of the subduction interface for the model of figure 3.2c. The lubrication layer quickly widens at the top (increasing $d_2^{\max}$) while thinning at the bottom (decreasing $d_2^{\min}$). This means that subduction of the SP drags fluid from the wider to the narrower part of the gap. According to lubrication theory, this is precisely the condition required to build up a positive excess pressure in the gap that keeps the two plates apart.

3.4 Thin-sheet analysis: SP kinematics

We begin by recalling the property of instantaneity of slow viscous flow with negligible inertia. A consequence of this property is that the dynamics of the two

interacting plates are entirely determined at each instant by the geometry of the system at that instant and by the fluid properties (i.e. density and viscosity of the ambient fluid and of the plates). Thus, in order to study the mechanics of SP-OP interaction it makes sense first to examine quasi-static configurations, without the added complexity of the purely kinematic time evolution. Following this approach, in this section and in § 3.5 we shall refer only to instantaneous solutions of the model (eq. (2.17)) whose geometrical parameters (e.g. θ_0, ℓ, L_{SP}, h_{OP} etc.) will be varied in order to represent different subduction zones at some arbitrary instant in time.

In order to better highlight the effect of the OP, we first review the case of free subduction of an isolated SP, recalling existing results and obtaining some new ones.

3.4.1 Instantaneous solutions: SP only

The crucial dimensionless parameter that controls the free subduction of an isolated SP can be determined using a simple scaling analysis of the forces acting on the portion of the SP that deforms by bending (Ribe, 2010). The analysis is carried out for a subducting plate whose leading end dips at an angle θ_0 and sinks with a vertical velocity V_{Sink}. Three forces act on the bending portion of the plate: the negative buoyancy of the slab, the internal viscous resistance to bending, and the traction applied by the external fluid. Balancing the negative buoyancy and the external traction yields a typical sinking speed $V_{\mathrm{Sink}} \sim V_{\mathrm{Stokes}}$, where

$$V_{\mathrm{Stokes}} = \frac{h_{\mathrm{SP}} \ell g \Delta\rho_1}{\eta_0}. \tag{3.6}$$

The characteristic ratio of the internal viscous resistance to the external traction is the 'flexural stiffness'

$$\mathrm{St} = \frac{\eta_1}{\eta_0} \left(\frac{h_{\mathrm{SP}}}{\ell_b} \right)^3, \tag{3.7}$$

where ℓ_b is the 'bending length', defined as the distance from the leading end of the SP's midsurface to one characteristic zero of the function $\dot{K}(s)$ that quantifies the rate of curling of the SP's midsurface. In geodynamical terms, ℓ_b is the sum of the slab length and the length of the region seaward of the trench where flexural bulging occurs (see § 2.3.3 for details). Ribe (2010) showed that the sinking speed V_{Sink} obeys a scaling law of the form

$$\frac{V_{\mathrm{Sink}}}{V_{\mathrm{Stokes}}} = \mathrm{fct}(\mathrm{St}, \theta_0), \tag{3.8}$$

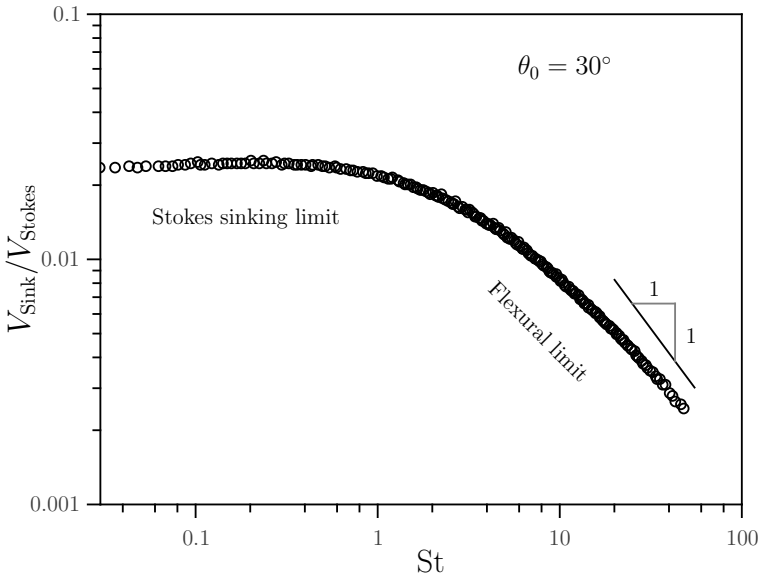

Figure 3.5. Dimensionless sinking speed $V_{\text{Sink}}/V_{\text{Stokes}}$ as a function of the plate stiffness St for $\theta_0 = 30°$. Numerical solutions were obtained for $L_{\text{SP}}/h_{\text{SP}}$=16, $d_1/h_{\text{SP}} \in [0.1, 0.2]$, $\ell/h_{\text{SP}} \in [5, 10]$, and $\lambda_1 \in [50, 10^5]$. As demonstrated in Ribe (2010), the only effect of the lubrication layer thickness d_1 is to modify ℓ_b, hence the flexural stiffness St.

which states that two SPs are dynamically similar if they have the same values of St and θ_0. The requirement that θ_0 be the same for both SPs is the condition for geometrical similarity of the slab's midsurface. Numerical solutions (Ribe, 2010) show that V_{Sink} does not depend on L_{SP}, which implies that geometrical similarity of the midsurface of the whole plate is not required.

As an illustration of the scaling law (3.8), fig. 3.5 shows $V_{\text{Sink}}/V_{\text{Stokes}}$ vs. St for $\theta_0 = 30°$, obtained from BEM solutions for different values of d_1/h_{SP}, ℓ/h_{SP}, and η_1/η_0. All the points collapse onto a single master curve, validating (3.8). The master curve has two distinct limits. In the 'Stokes' limit $\text{St} \leq 1$, the slab's negative buoyancy is balanced by the external traction. The slope of the curve is zero, meaning that the sinking speed is controlled entirely by the viscosity η_0 of the ambient fluid. In the 'flexural' limit $\text{St} \gg 1$, by contrast, the negative buoyancy is balanced by the internal resistance to bending. The slope of the curve is -1, and the sinking speed is controlled by the viscosity η_1 of the SP.

With the definition of St in hand, we now determine a scaling law for the plate speed U_{SP}, defined as the average horizontal velocity of the midsurface of the flat portion of the SP. Unlike V_{Sink}, U_{SP} depends on the plate length L_{SP}, because a longer plate is subject to a greater drag force from the underlying mantle. Accordingly, the analog of the scaling law (3.8) is

$$\frac{U_{\text{SP}}}{V_{\text{Stokes}}} = \text{fct}\left(\text{St}, \theta_0, \frac{L_{\text{SP}}}{\ell}\right). \tag{3.9}$$

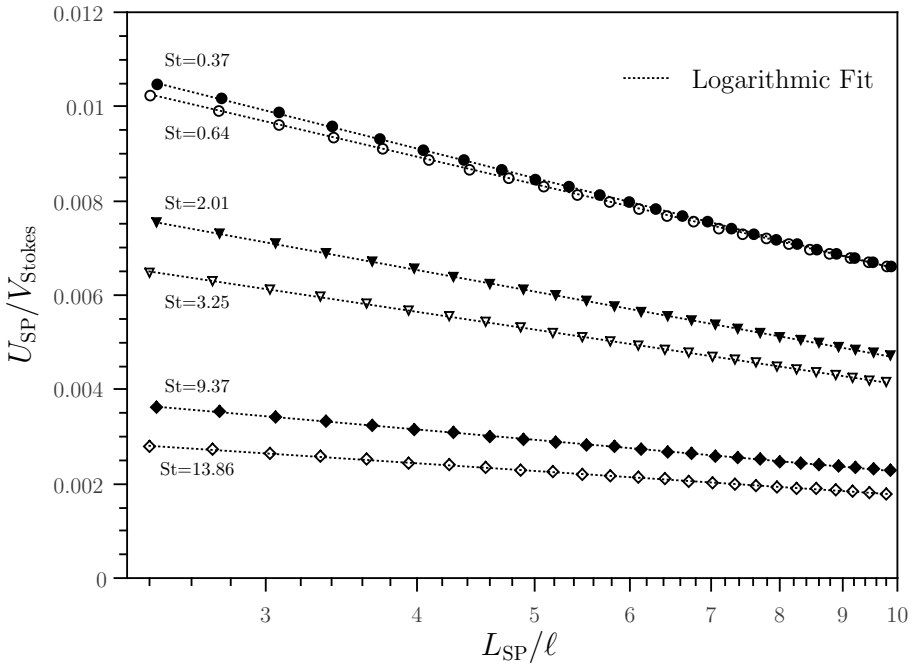

Figure 3.6. Dimensionless plate speed U_{SP}/V_{Stokes} as a function of L_{SP}/ℓ for several values of St and $\theta_0 = 30°$ (semi-log plot). Values of St $\in [0.37, 14]$ were obtained using the following parameters: ℓ/h =7 (●,▼,◆), ℓ/h =5 (○,▽,◇) and λ=10^2 (●,○), λ=10^3 (▼,▽), λ=10^4 (◆,◇).

Both θ_0 and L_{SP}/ℓ appear in the list of arguments because both are necessary to define the geometrical similarity of the sheet's whole midsurface.

Guided by the proposed scaling law (3.9), we plot in fig. 3.6 the dimensionless SP speed U_{SP}/V_{Stokes} as a function of L_{SP}/ℓ for several values of St and $\theta_0 = 30°$. The flexural stiffness St was adjusted by varying both the viscosity ratio λ_1 and the slab length ℓ, which directly affects ℓ_b. Three aspects of the results are noteworthy. First, the six curves in fig. 3.6 are nonintersecting and appear from top to bottom in order of increasing St, which validates the assumed form (3.9) of the scaling law. Second, each curve on this semi-log plot is a nearly perfect straight line, indicating that the plate speed depends logarithmically on the plate length for a wide range of values of St. Third, the transition from the Stokes to the flexural limit is manifest in the decreasing slopes of the curves from top to bottom. For low values of St, an increase of L_{SP} increases the drag force on the base of the plate, and therefore strongly affects U_{SP} since it is the external viscosity η_0 that governs the plate's dynamics. On the other hand, for St $\gg 1$ U_{SP} becomes much less sensitive to L_{SP} since it is the internal viscosity η_1 (and no longer the basal drag) that controls the plate motion.

Both the slope α and the intercept β of the lines in fig. 3.6 obviously depend

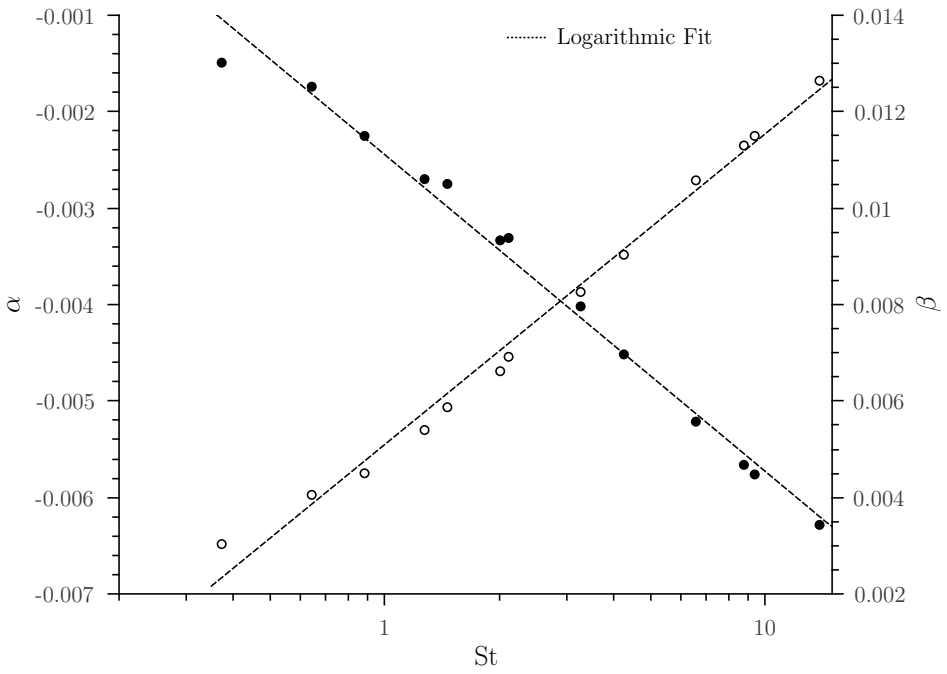

Figure 3.7. Values of the slope (left y-axis) and the intercept (right y-axis) extrapolated from the logarithmic fit of curves $U_{\mathrm{SP}}/V_{\mathrm{Stokes}} = \mathrm{fct}\,(L_{\mathrm{SP}}/\ell)$ as the ones shown in figure 3.6. St varies within the range ~ [0.3-14].

on St. Quantifying these relations, we find the more detailed scaling law

$$\frac{U_{\mathrm{SP}}}{V_{\mathrm{Stokes}}} = \beta(\mathrm{St}) + \alpha(\mathrm{St}) \log\left(L_{\mathrm{SP}}/\ell\right) \tag{3.10}$$

where $\alpha(\mathrm{St})$ and $\beta(\mathrm{St})$ are shown in fig. 3.7. For $\mathrm{St} \in [0.1, 20]$ and $L_{\mathrm{SP}}/\ell \in [2, 10]$, the numerical solutions for $U_{\mathrm{SP}}/V_{\mathrm{Stokes}}$ collapse onto the universal curve (3.10) to within an error of ± 5 %.

To conclude our analysis of the SP ONLY case, we quantify the convergence speed $V_{\mathrm{Conv}} \equiv \mathrm{d}\ell_s/\mathrm{d}t$. A numerically stable value of this speed is obtained by running the code for three time steps and defining V_{Conv} as the best-fitting slope of the curve $\ell_s(t)$. The results are shown in fig. 3.8. The numerical solutions show that V_{Conv}, like V_{Sink}, does not depend on the plate length L_{SP}. However, we find that V_{Conv} depends on the ratio ℓ/h. The scaling law therefore has the general form

$$\frac{V_{\mathrm{Conv}}}{V_{\mathrm{Stokes}}} = \mathrm{fct}\left(\mathrm{St}, \theta_0, \frac{\ell}{h}\right). \tag{3.11}$$

The presence of ℓ/h in the list of arguments means that dynamical similarity depends on the geometry of the whole slab, and not just the geometry of its midsurface.

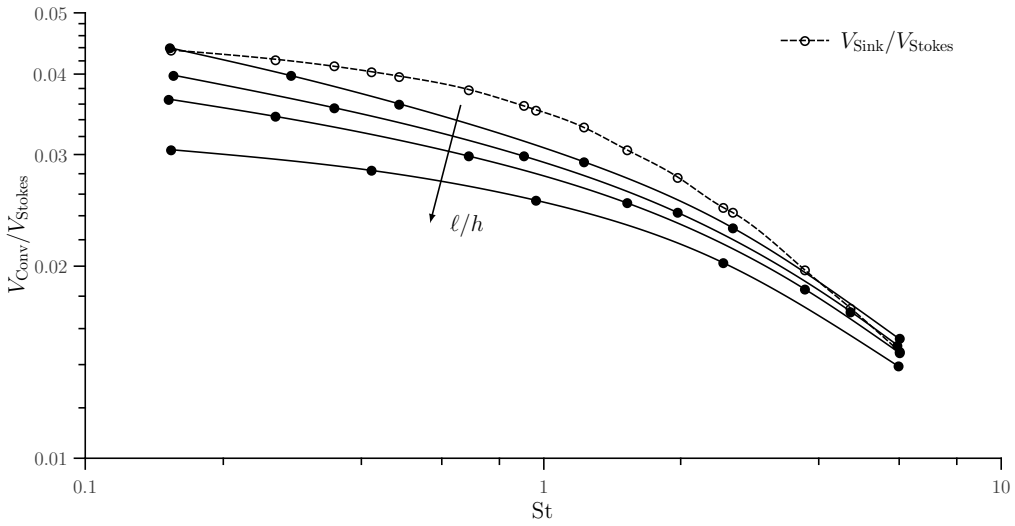

Figure 3.8. Dimensionless convergence speed $V_{\mathrm{Conv}}/V_{\mathrm{Stokes}}$ as a function of the flexural stiffness St for $\ell/h = 5, 6, 7, 9$. The corresponding curve $V_{\mathrm{Sink}}/V_{\mathrm{Stokes}}$ vs. St is shown for comparison. The slab dip is fixed at $\theta_0 = 60°$.

3.4.2 Instantaneous solutions: SP+OP

The next task is to determine how the presence of the OP influences the reference scaling laws (3.9) and (3.11) for the SP alone. In order to reduce the number of parameters involved, we shall vary only the OP geometry and the width of the lubrication layer between the two plates, leaving fixed the OP viscosity ratio $\lambda_2 = 10^4$ (quasi-rigid OP) and its buoyancy ratio $\Gamma = 0$ (neutrally buoyant OP). This choice is partly motivated by previous results showing that the viscosity and buoyancy of the OP play a crucial role in determining its stress state but only weakly influence the SP kinematics (Holt *et al.*, 2015).

We begin by examining the influence of different geometrical parameters on the dimensionless plate speed $U_{\mathrm{SP}}/V_{\mathrm{Stokes}}$, following the approach used to build figure 3.6. However, we now fix both the dip of the slab (=30°) and its viscosity ratio (=10^3), which give a nearly constant value of St for all configurations having the same slab length. While St depends somewhat on the OP thickness and the thickness of the lubrication layer between the two plates, the dependence on ℓ/h_{SP} and λ_1 is much stronger, and so it is plausible to consider St constant unless otherwise specified.

Fig. 3.9 shows the dimensionless plate speed $U_{\mathrm{SP}}/V_{\mathrm{Stokes}}$ as a function of L_{SP}/ℓ for the SP+OP case. The two solid lines are for the SP ONLY and SP+OP reference cases whose parameters are given in table 3.3. The four dashed lines are for variations of the SP+OP reference case with respect to the parameter indicated.

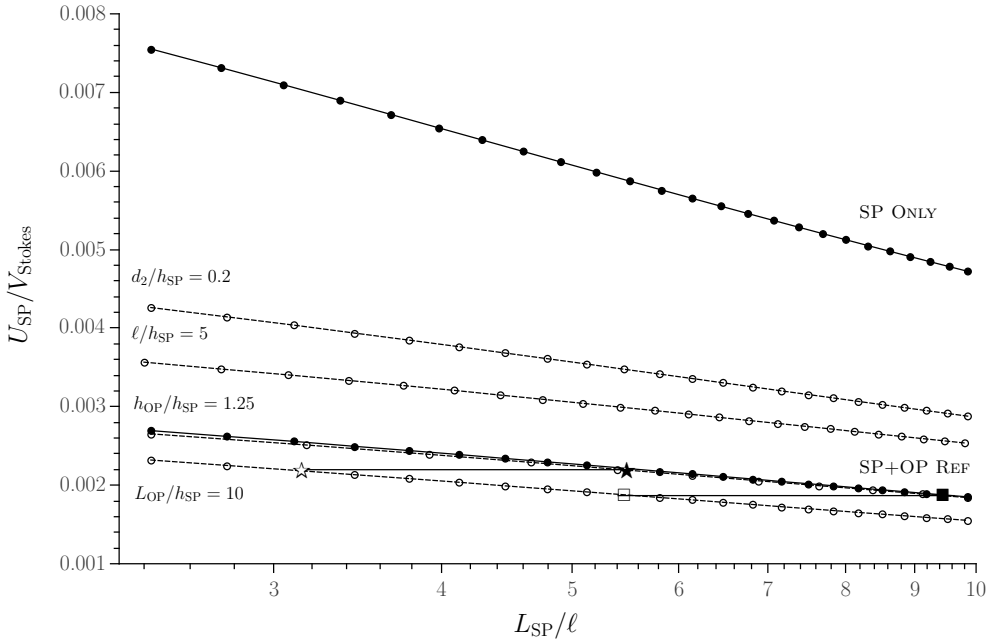

Figure 3.9. Dimensionless plate speed U_{SP}/V_{Stokes} as a function of L_{SP}/ℓ (semi-log plot) for the SP+OP case. Solid lines: SP Only and SP+OP reference cases whose configuration is given in table 3.3. Dashed lines: variations of the SP+OP reference case with respect to the parameter indicated. $L_{SP}/L_{OP} \approx 2$ along the line (★,☆), while $L_{SP}/L_{OP} \approx 4$ along the line (■,□).

Table 3.3. Configuration of the reference cases

	SP			OP		
	θ_0	ℓ/h_{SP}	λ_1	d_2/h_{SP}	L_{OP}/h_{SP}	h_{OP}/h_{SP}
SP Only	30°	7	10^3	-	-	-
SP+OP Ref	30°	7	10^3	0.1	16	1

The first noteworthy aspect of fig. 3.9 is that all the curves are straight lines. The dimensionless plate speed therefore depends logarithmically on L_{SP}/ℓ, just as it did for the SP ONLY case. We find that this dependence is general, independently of the geometry of the system.

Next, we focus on the two solid lines of figure 3.9 labeled as SP+OP REF and SP ONLY, whose parameters are given in table 3.3. We see that the presence of the OP decreases U_{SP}, but more strongly for a shorter SP. This means that the dimensionless SP speed depends on the ratio L_{SP}/L_{OP} of the lengths of the two plates. This is confirmed by comparing the SP+OP REF curve with the curve for a shorter overriding plate ($L_{OP}/h_{SP} = 10$). We choose the point with $L_{SP}/\ell = 5.45$ on the SP+OP REF curve (black star), and draw a horizontal line that meets the curve for $L_{OP}/h_{SP} = 10$ at the point with $L_{SP}/\ell = 3.15$ denoted by the white star. We find that the two starred points have similar values of the ratio $L_{SP}/L_{OP} \in [2.2, 2.4]$.

Turning to the dependence of U_{SP} on the other geometrical parameters, we see first that it is essentially independent of h_{OP}. Next, the normalized SP speed U_{SP}/V_{Stokes} increases when the slab length decreases from $7h_{SP}$ to $5h_{SP}$. This is surprising at first sight, since for a SP alone a shorter (hence stiffer) slab is associated with a lower value of U_{SP}/V_{Stokes} (fig. 3.6). The cause of this counterintuitive behavior lies in the presence of the OP, whose trenchward velocity decreases when ℓ/h_{SP} decreases (figure 3.10a). Since the SP and the OP are strongly coupled by the lubrication force in the gap between them, the SP necessarily moves faster (to the right in fig. 3.1) when the OP moves more slowly (to the left).

Finally, we see in fig. 3.9 that an increase in the lubrication gap thickness d_2 from $0.1h_{SP}$ to $0.2h_{SP}$ increases U_{SP} by a large factor ~ 1.6. This occurs because increasing d_2 decreases the lubrication force at the subduction interface that is responsible for the coupling between the two plates.

In view of the discussion above, we can finally write the scaling law for the SP speed in the presence of an OP in the general form

$$U_{SP}/V_{Stokes} = \text{fct}\left(\text{St}, \theta_0, \frac{L_{SP}}{\ell}, \frac{\ell}{h_{SP}}, \frac{L_{SP}}{L_{OP}}, \frac{d_2}{h_{SP}}\right). \tag{3.12}$$

Obviously a scaling law with six arguments is too complicated to explore fully, and so we content ourselves with the results presented above.

Before turning to an examination of the convergence rate V_{Conv}, we mention two interesting features that have emerged from our analysis of the SP speed. The first concerns the driving mechanism for the motion of the OP. Two forces act on the OP: the tractions applied by the subduction-induced flow beneath its base, and the

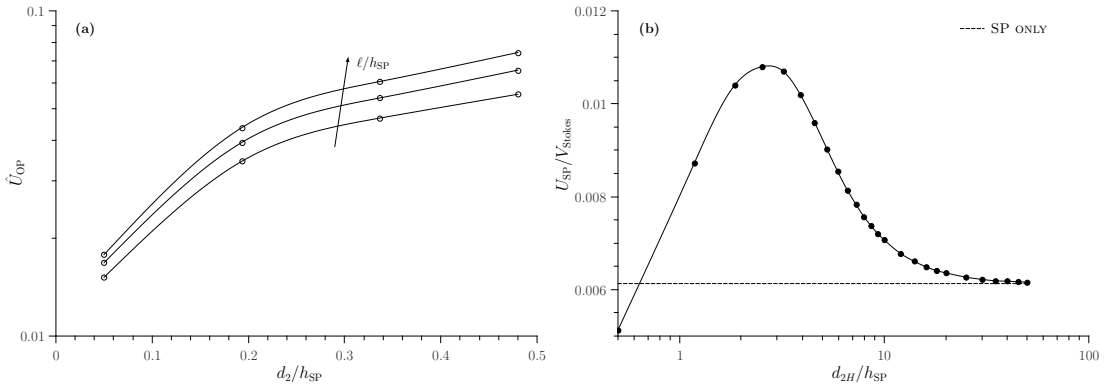

Figure 3.10. **(a)** Dimensionless OP speed vs. dimensionless subduction interface thickness d_2/h_{SP}, for $\ell/h_{SP} = 5, 6, 7$. The ratio $L_{SP}/\ell = 3.2$ is constant. The parameters not specified explicitly are given in table 3.3. **(b)** Dimensionless plate speed U_{SP}/V_{Stokes} as a function of d_{2H}/h_{SP} for the reference case, where d_{2H} is the horizontal (as opposed to normal) separation between the SP and the OP. The slab length is $\ell/h_{SP} = 5$ and $L_{SP}/\ell = 3$. The other parameters are those given in table 3.3. The dashed line indicates the value of U_{SP}/V_{Stokes} for the corresponding SP ONLY case.

lubrication force in the subduction interface. The subduction-induced tractions are obviously the driving force, as confirmed by the fact that the OP speed is an increasing function of the parameter ℓ/h_{SP} that represents the importance of slab pull (fig. 3.10a). Because the sum of the forces is zero, the lubrication force must necessarily be a resisting force. This is confirmed by the fact that U_{OP} decreases as the subduction interface becomes narrower (fig. 3.10a). Figure 3.11 shows the subduction-induced flow for $\ell/h_{SP} = 7$ along with the velocity at the lower surface of the OP. The vertical gradient of the horizontal velocity near the SP corresponds to a shear stress that drives the OP leftward.

The second feature concerns the dependence of U_{SP} on the interplate gap width for values $d_2 > 0.2h_{SP}$. Fig. 3.10b shows the dimensionless SP speed U_{SP}/V_{Stokes} as a function of d_{2H}/h_{SP} for the reference case, where d_{2H} is the horizontal separation between the SP and the OP. The dashed line shows the value of U_{SP}/V_{Stokes} for the corresponding SP ONLY case. Surprisingly, we find that the presence of the OP slows down the SP only for small separations $d_{2H}/h_{SP} \leq 0.65$. For larger separations, the presence of the OP makes the SP move faster by up to 75%. In the limit $d_{2H}/h_{SP} \to \infty$ the SP ONLY case is recovered.

We now turn to the influence of the OP on the dimensionless convergence speed V_{Conv}/V_{Stokes}. Numerical solutions show that V_{Conv} is controlled only by the geometries of the slab's midsurface and the lubrication gap, and is independent of L_{SP}, L_{OP}, and h_{OP}. In the presence of the OP, therefore, the generalized form of

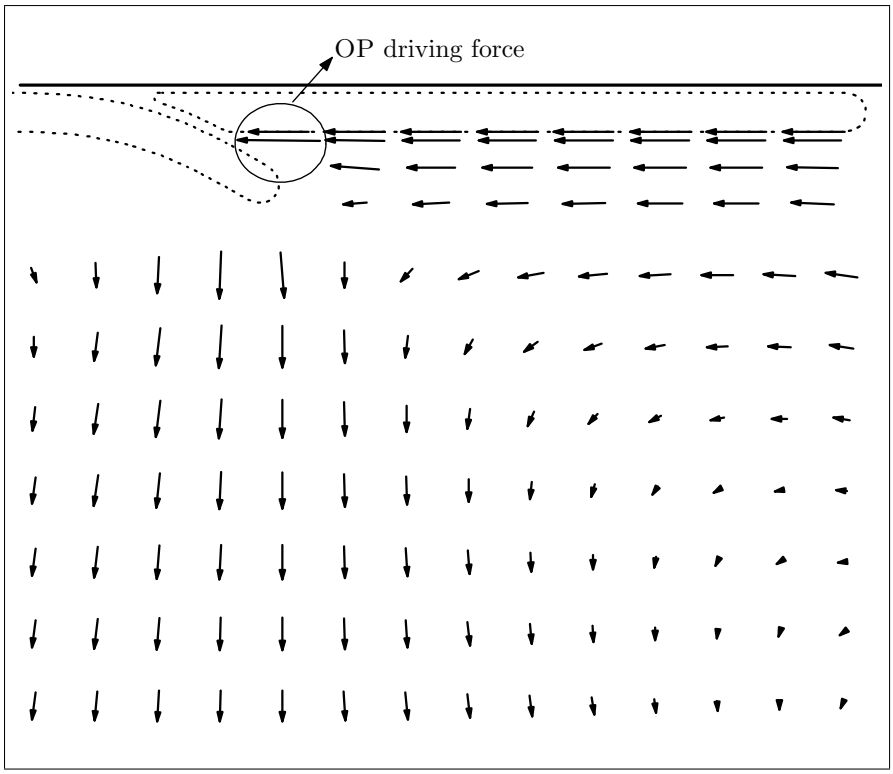

Figure 3.11. Mantle flow generated by the sinking slab at $t = 0$ for the parameters of table 3.The oval indicates the velocity gradient corresponding to a shear stress that drives the OP leftward.

the scaling law (3.11) is

$$V_{\text{Conv}}/V_{\text{Stokes}} = \text{fct}\left(\text{St}, \theta_0, \frac{\ell}{h_{\text{SP}}}, \frac{d_2}{h_{\text{SP}}}\right). \tag{3.13}$$

Since the gap thickness d_2 controls the lubrication forces arising at the subduction interface, we expect that parameter to be a critical determinant of the convergence speed. Fig. 3.12 shows $V_{\text{Conv}}/V_{\text{Stokes}}$ as a function of the dimensionless horizontal SP/OP separation d_{2H}/h_{SP} for four values of the flexural stiffness and $\theta_0 = 60°$. $V_{\text{Conv}}/V_{\text{Stokes}}$ increases strongly with the gap width $d_{2H}/h_{\text{SP}} \in [0.05, 0.35]$, and then reaches a plateau for $d_{2H}/h_{\text{SP}} \approx 1$ where the SP ONLY case (open squares) is recovered. Unlike the SP speed (fig. 3.10b), the convergence speed V_{Conv} never exceeds its SP ONLY value.

As a final remark, we note that fig. 3.12 confirms the crucial role played by the plate's stiffness St in controlling the kinematics of the SP, as we already saw in fig. 3.6 for the SP speed U_{SP}. Both V_{Conv} and U_{SP} decrease strongly as St increases, reflecting the overall slowing down of subduction associated with greater plate stiffness (fig. 3.5).

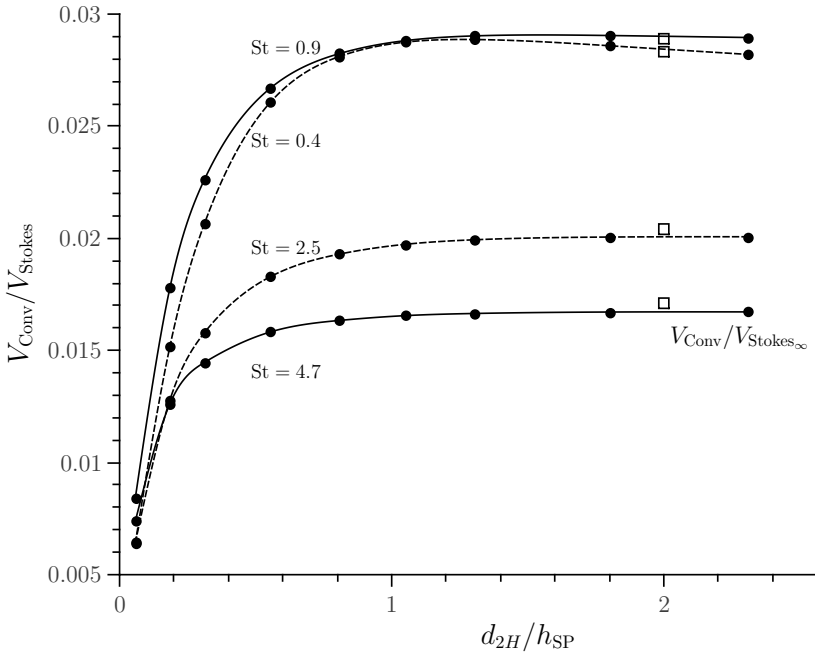

Figure 3.12. Dimensionless convergence speed $V_{\mathrm{Conv}}/V_{\mathrm{Stokes}}$ vs. dimensionless horizontal SP/OP separation d_{2H}/h_{SP}, for several values of the flexural stiffness St and $\theta_0 = 60°$. The dimensionless slab length $\ell/h_{\mathrm{SP}} = 9$ (dashed lines) or 6 (solid lines). The open squares indicate the values of $V_{\mathrm{Conv}}/V_{\mathrm{Stokes}}$ for the SP ONLY case ($d_{2H}/h_{\mathrm{SP}} \to \infty$).

3.5 Thin-sheet analysis: OP deformation

In this section we focus on the subduction-induced deformation of the OP. As in the previous section, we consider only instantaneous solutions of the Stokes equations for the geometry shown in fig. 3.1. To simplify the notation, the arclength coordinate s_{OP} will be denoted by s.

To understand the deformation of a thin viscous sheet, it suffices to characterize the deformation of its midsurface. To do this, we solve equation (2.17) for points $\mathbf{x}$ located on the OP midsurface to obtain the midsurface velocity $U(s)\mathbf{s} + W(s)\mathbf{z}$, where $\mathbf{s}$ and $\mathbf{z}$ are unit vectors parallel to and perpendicular to the midsurface, respectively. The deformation of the midsurface is then characterized by the rate of stretching Δ and the rate of change of curvature ('curling rate') $\dot{K}$, which for a flat sheet are

$$\Delta = U', \qquad \dot{K} = W'', \tag{3.14}$$

where primes denote $\mathrm{d}/\mathrm{d}s$. The quantities Δ and $\dot{K}$ measure the rates of deformation of the midsurface by stretching (or shortening) and by bending, respectively.

Useful measures of the intensities of the stretching and bending deformations of a thin sheet are the rates of viscous dissipation of energy associated with each.

Per unit area of the OP midsurface, these are

$$\phi_s = 4\eta_2 h_{\mathrm{OP}}\Delta^2, \qquad \phi_b = \frac{1}{3}\eta_2 h_{\mathrm{OP}}^3 \dot{K}^2, \tag{3.15}$$

where the subscripts s and b refer to stretching/shortening and bending, respectively. The relative magnitudes of $\phi_b(s)$ and $\phi_s(s)$ indicate which mode of deformation is dominant as a function of arclength. We note for future reference that

$$\phi_b = -M\dot{K}, \qquad M = -\frac{1}{3}\eta_2 h_{\mathrm{OP}}^3 \dot{K}, \tag{3.16}$$

where M is the bending moment.

In the rest of this section, all quantities referred to are dimensionless, having been nondimensionalized using h_{SP} as the length scale and $g\Delta\rho_1 h_{\mathrm{SP}}^2/\eta_0$ as the velocity scale. Consequently, the rates of viscous dissipation of energy will scale as:

$$\hat{\phi} = \frac{\eta_0}{h_{\mathrm{SP}}^3 \left(g\Delta\rho_1\right)^2}\phi. \tag{3.17}$$

Our first task is to explore how the properties of the SP influence the deformation of the OP. Our numerical simulations show that the OP deformation depends neither on L_{SP} nor on L_{OP}, and so we set these arbitrarily to $L_{\mathrm{SP}} = L_{\mathrm{OP}} = 16h_{\mathrm{SP}}$. We then fix the viscosity ratios of both plates ($\lambda_1 = \lambda_2 = 350$), the OP thickness ($h_{\mathrm{OP}} = h_{\mathrm{SP}}$) and the interplate gap width ($d_2/h_{\mathrm{SP}} = 0.1$), which allows us to focus on the SP dip θ_0 and slab length ℓ/h_{SP}.

Fig. 3.13, at the top, shows $\dot{K}(s)$ and $\Delta(s)$ as function of θ_0 for $\ell/h_{\mathrm{SP}} = 7$ and $\Gamma = 0$. The steeper the subduction, the higher the magnitude of the bending moment in the OP. However, the length of the portion of the OP where the bending moment is significant (= bending length) is independent of θ_0. The stretching rate Δ does not vary monotonically with the slab dip: its magnitude increases from $\theta_0 = 30°$ to 60°, and then decreases from 60° to 90°. For $\theta_0 = 30°$ there is weak backarc extension for $s > 2.7$.

The bottom part of fig. 3.13 shows $\dot{K}(s)$ and $\Delta(s)$ as functions of ℓ/h_{SP} for $\theta_0 = 30°$ and $\Gamma = 0$. The magnitude of the bending moment does not vary significantly with the slab length, but the bending portion of the OP becomes longer as the slab length increases. The magnitude of the compression $\Delta < 0$ is greater for longer slabs, while shorter slabs cause weak extension in the OP. The shorter the slab, the longer the portion of the OP deforming in extension ($s > 1.5$ for $\ell/h_{\mathrm{SP}} = 5$, $s > 2.7$ for $\ell/h_{\mathrm{SP}} = 7$.)

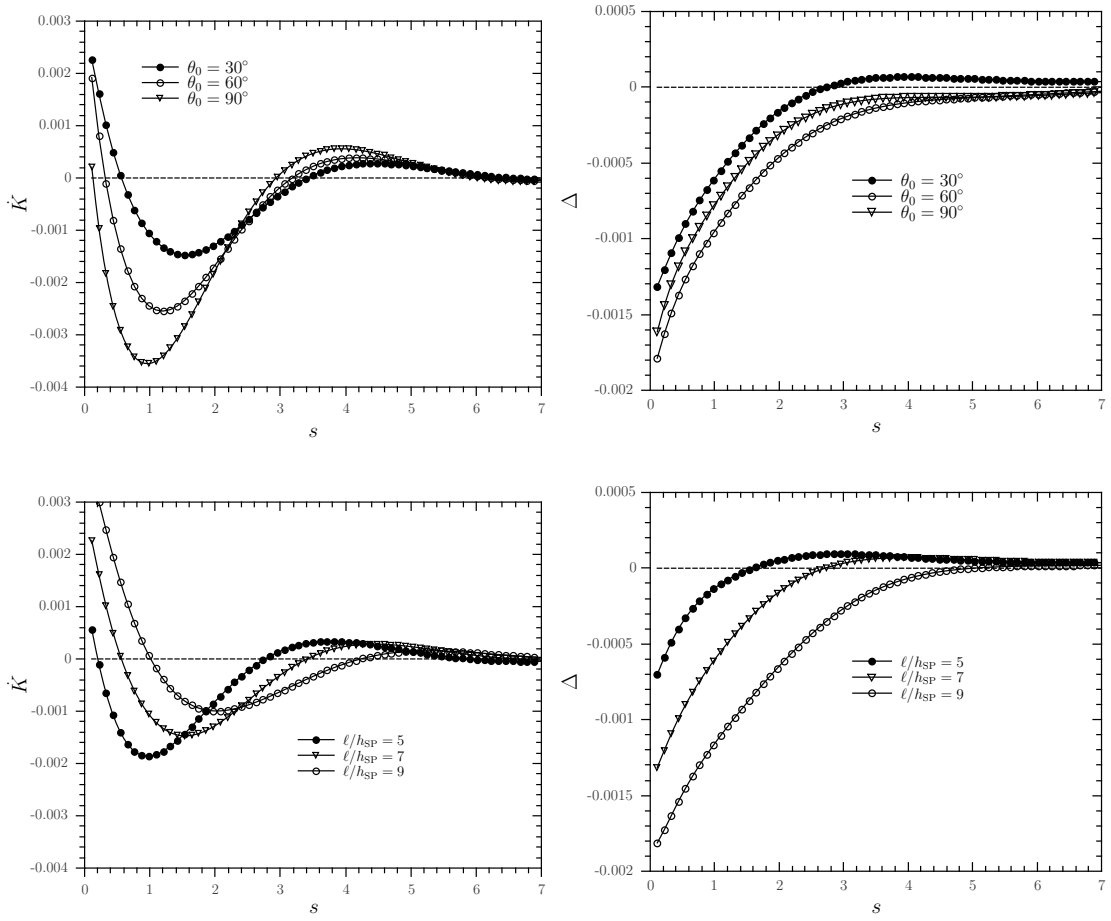

Figure 3.13. Curling rate $\dot{K}$ and stretching rate Δ along the midsurface of the OP for three different values of θ_0, $\ell/h_{\mathrm{SP}} = 7$, and $\Gamma = 0$ (top figure) and for three different values of ℓ/h_{SP}, $\theta_0 = 30°$, and $\Gamma = 0$ (bottom figure). The other parameters are given in the text.

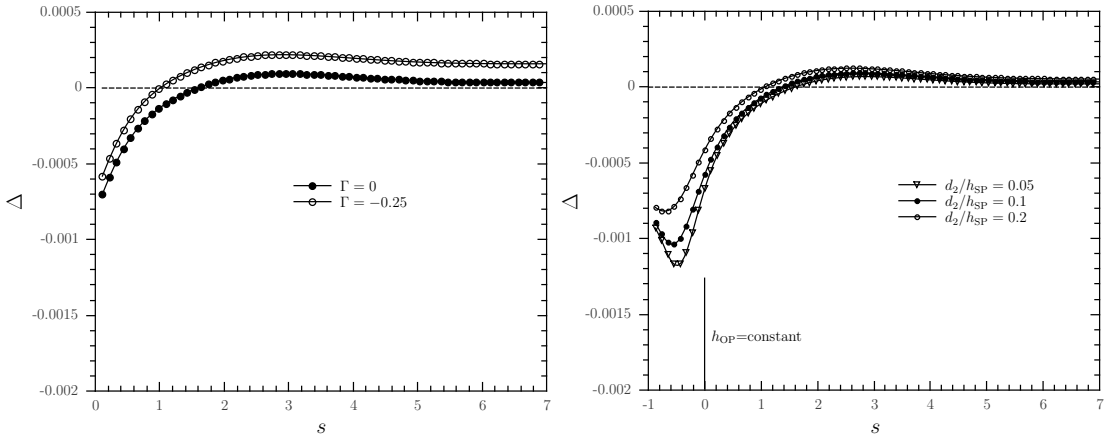

Figure 3.14. Top figure: Curling rate $\dot{K}$ and stretching rate Δ along the midsurface of a neutrally buoyant ($\Gamma = 0$) or positively buoyant ($\Gamma = -0.25$) OP. For both cases $\ell/h_{SP} = 5$ and $\theta_0 = 30°$. The other parameters are given in the text. Bottom figure: Curling rate $\dot{K}$ and stretching rate Δ for different values of d_2/h_{SP}, with $\ell/h_{SP} = 5$, $\theta_0 = 30°$ and $\Gamma = 0$. Arclengths $-1 \le s \le 0$ correspond to a leftward extension of the midsurface into the triangular endpiece of the OP (fig. 3.1).

At the top of fig. 3.14 are shown $\dot{K}(s)$ and $\Delta(s)$ for two values of Γ, $\theta_0 = 30°$, and $\ell/h_{SP} = 5$. In the previous figures, we saw that a short and shallowly dipping slab leads to relatively small bending and stretching deformations of the OP. However, the same two conditions are precisely those that lead to back-arc extension (around 300 km from the trench assuming $h_{SP} = 100$ km). Fig. 3.14 (top) shows that the transition between compression and extension is further encouraged by OP buoyancy. For example, when $\Gamma = -0.25$ ($\Delta\rho_2 = -18$ kg/m^3 assuming $\Delta\rho_1 = 70$ kg/m^3), the stretching rate curve shifts upward and the length of the extension zone increases. The curling rate $\dot{K}$, however, is unaffected.

Fig. 3.15 shows the rates of energy dissipation ϕ_b and ϕ_s for the configurations of the top part of fig. 3.14. The deformation changes from compression-dominated close to the trench to bending-dominated further away, a general pattern that we find for many choices of the dimensionless parameters of the model. Only for steep angles of subduction and (mainly) long slabs is the deformation of the OP almost exclusively compression-dominated. For the particular case of a positively buoyant OP ($\Gamma < 0$), fig. 3.15 shows that there is an additional extension-dominated domain in the backarc region beyond the bending zone.

To conclude this section, we examine the influence of the thickness of the OP and of the interplate gap on the OP deformation. As one would expect, varying the OP thickness within the range $h_{OP} \in [0.75, 1.25]$ changes $\dot{K}$ and Δ substantially, simply because the resistance of the OP to deformation is proportional to h_{OP} (for stretching) and h_{OP}^3 (for bending).

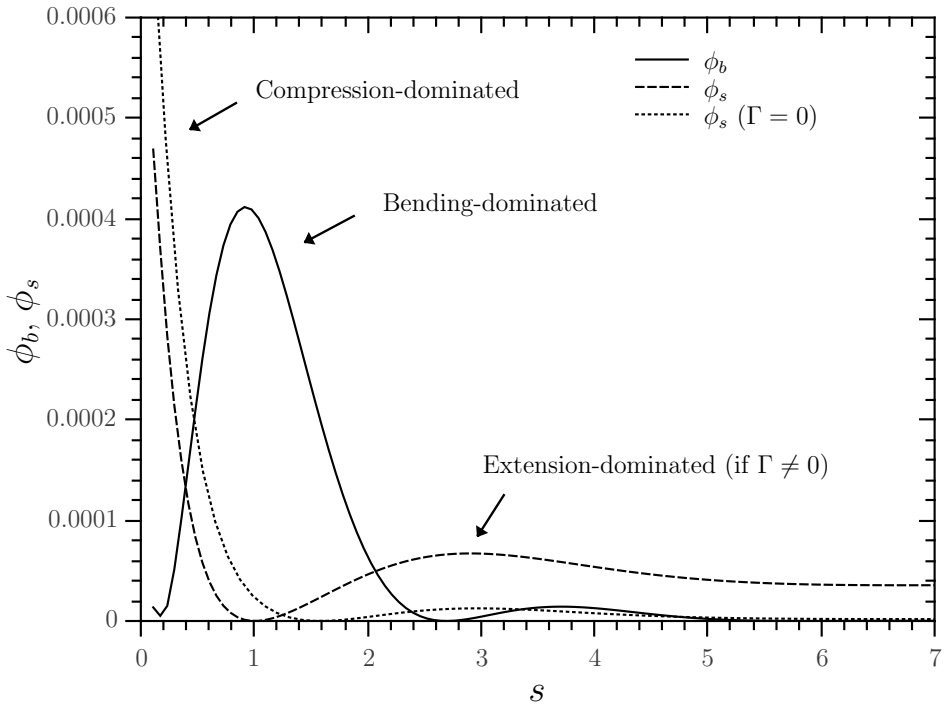

Figure 3.15. Rates of energy dissipation due to bending (ϕ_b, solid line) and stretching/shortening (ϕ_s, dashed line) of a positively buoyant OP with $\Gamma = -0.25$. For comparison, the dotted line shows the stretching/shortening curve for a neutrally buoyant OP ($\Gamma = 0$).

As for the effect of the subduction channel width d_2, it is significant only very close to the trench. To show this, we extend leftward the OP midsurface (figure 3.1) into the triangular endpiece, which allows us to calculate $\dot{K}$ and Δ for $-1 \leq s \leq 0$. The bottom part of fig. 3.14 shows $\dot{K}$ and Δ for three different values of d_2/h_{SP} for a case with $\ell/h_{SP} = 5$, $\theta_0 = 30°$ and $\Gamma = 0$. The differences among the three curves are confined essentially to $-1 \leq s \leq 1$. In the near-trench (forearc) region $-1 \leq s \leq 0$, both $\dot{K}$ and Δ increase in magnitude as d_2/h_{SP} diminishes, reflecting the increase of the lubrication pressure in the subduction interface. The influence of the lubrication force on the deformation of the OP essentially disappears beyond $s = 1$.

3.6 Geophysical application: evaluation of the interface viscosity of the central Aleutian slab

In this section we apply our BEM model to a real subdction zone in order to constrain the effective value of the strength of the subduction interface. We start by defining the dimensionless interface strength of a subduction zone as

$$\gamma = \frac{\eta_{SI}}{\eta_0}\frac{h_{SP}}{d_2}, \tag{3.18}$$

where η_{SI} is the viscosity of the fluid in the subduction interface channel. Equation (3.18) arises from the definition of the shear force acting on the SP across the subduction interface, and implies that the interface strength can be increased either by increasing its viscosity or decreasing its thickness d_2. In our model, $\eta_{SI} \equiv \eta_0$ is constant, but this does not matter because only the ratio η_{SI}/d_2 is dynamically significant. Thus we can vary the strength of the subduction interface by varying d_2 alone.

The next step is to choose a subduction zone that can be reasonably approximated by our model. Perusing the database of Lallemand *et al.* (2005), we decided to focus on the central Aleutian subduction zone. There are two main reasons for this choice. First, this portion of the Aleutian slab is far from the edges of the subduction zone, making it reasonable to use a 2-D model with no toroidal flow. This approximation is validated by the similarity of the geometries and subduction rates among the three neighboring central Aleutian transects listed in table 3.4. Second, the central Aleutian slab extends to depths of only 500-550 km, and so has not yet interacted with a potential viscosity jump at the 660 km discontinuity. Our model with a constant mantle viscosity is therefore reasonable for subduction in the Aleutian region. The particular value of the viscosity that we choose is

Table 3.4. Geometry and convergence rates of the 3 transects of the central Aleutian slab derived from Lallemand *et al.* (2005). We assume h_{SP} ~ 100 km. The last line ('BEM-segment') describes the configuration adopted for the simulation and it reports the corresponding value of V_{Conv} adopted for the comparison.

Observed parameters				
	V_{Conv} [mm yr^{-1}]	θ_0	ℓ [km]	Depth [km]
CALE4	61.00	58.00°	704	550
CALE5	61.00	59.00°	708	550
CALE6	59.00	62.00°	640	500

Simulation parameters							
	V_{Conv} [mm yr^{-1}]	θ_0	ℓ/h_{SP}	L_{SP}/h_{SP}	L_{OP}/h_{SP}	h_{OP}/h_{SP}	Γ
'BEM-segment'	60.33	59.67°	6.84	100.00	70.00	1.25	-0.25

discussed below.

Having selected the subduction zone, we specify the corresponding configuration of our BEM model by averaging the properties given for the three transects CALE4, CALE5 and CALE6 tabulated by Lallemand *et al.* (2005). Table 3.4 gives the relevant parameters for these transects, together with a list ('BEM-segment') of the parameters adopted for the simulation. The lengths L_{SP} and L_{OP} of the two plates have been computed as the square roots of the approximate areas of the subducting Pacific plate ($\approx 10^8$ km^2) and the overriding North American plate ($\approx 8\times10^7$ km^2). However, the choice of the two lengths is somewhat arbitrary since the target parameter of our analysis, V_{Conv}, depends neither on L_{SP} nor on L_{OP} (§ 3.4.2).

Having defined the geometry of the subduction zone, we then run the model for a reasonable range (Ribe, 2010) of the viscosity ratios of the two plates, $\lambda_1 = \lambda_2 \in$ [150-450], and for a range of values of the dimensionless interface strength $\gamma \in$ [0.5-20]. This yields curves of the dimensionless convergence rate as a function of γ. Next, we dimensionalize the calculated convergence rates by multiplying by the velocity scale V_{Stokes} given by equaion (3.6). To calculate V_{Stokes}, we assume h_{SP} = 100 km and $\Delta\rho_1$ = 70 kg m^{-3}, and take η_0 to be the depth-averaged viscosity in the range 0-1000 km inferred by Mitrovica & Forte (2004). Taking into account the error bars on the viscosities estimated by Mitrovica & Forte (2004), we find that the minimum, best-estimate, and maximum values of η_0 are

$$\eta_{0(-)} \sim 3.92\times10^{20}\text{Pa s}, \quad \eta_{0(\text{Best})} \sim 5.44\times10^{20}\text{Pa s}, \quad \eta_{0(+)} \sim 6.95\times10^{20}\text{Pa s}. \quad (3.19)$$

Thus, we can now obtain the corresponding value of V_{Conv}/V_{Stokes} for the 'BEM-segment' as a function of the mantle viscosities given in 3.19) and find the range

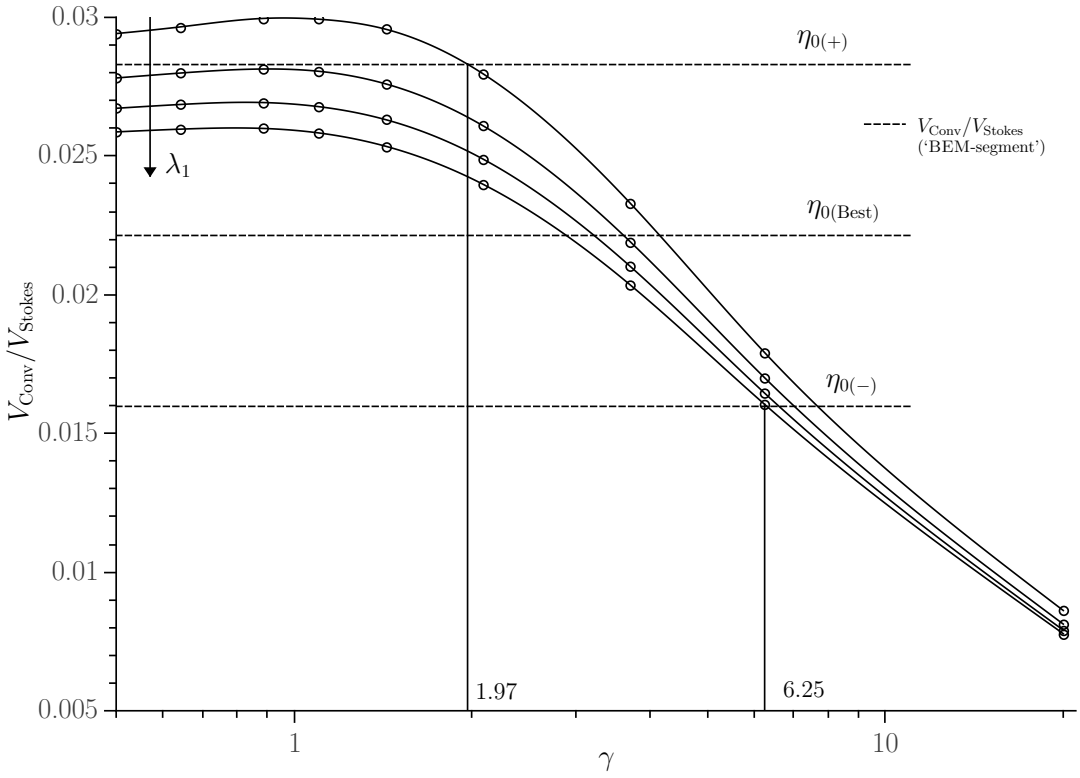

Figure 3.16. Dimensionless convergence speed plotted against dimensionless interface strength for different values of the viscosity ratio of the plates: $\lambda_1 = 150, 250, 350, 450$. The horizontal dashed lines represent the values of $V_{\mathrm{Conv}}/V_{\mathrm{Stokes}}$ that correspond to the true convergence rate of the 'BEM-segment', nondimensionalized using the range of mantle viscosities given by Mitrovica & Forte (2004). See text for more details.

of γ on the curves $V_{\mathrm{Conv}}/V_{\mathrm{Stokes}}$ = fct (γ) that predicts the observed convergence rate. Figure 3.16 shows the final result, where we find $\gamma \in [1.97\text{-}6.25]$. To estimate the corresponding viscosity of the subduction interface, we assume $d_2/h_{\mathrm{SP}} \sim 0.07$, which is equivalent to assuming that the subduction interface is the oceanic crust. We then find from equation (3.18) that $\eta_{\mathrm{SI}} = 0.96\text{-}1.72\times10^{20}$ Pa s.

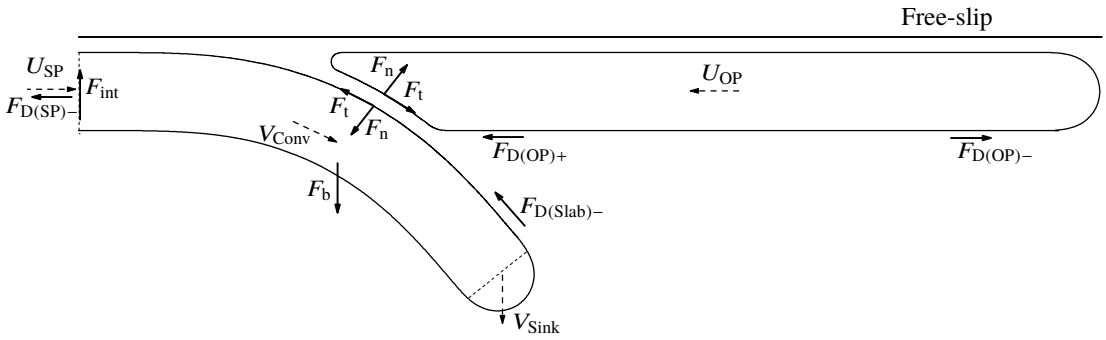

Figure 3.17. Principal forces and velocities associated with subduction. The dashed lines indicate the characteristic velocities of the two plates, and the thick lines indicate the forces acting on them. $F_{\mathrm{D(OP)+}}$ is the drag force driving the OP motion while the different forces $F_{\mathrm{D}(xxx)-}$ represent the drag resisting the displacement of the portion of the plate to which they refer. F_{n} and F_{t} are the lubrication forces acting on the two plates, equal in magnitude and opposite in direction. F_{int} is the internal force of the SP opposing its bending and F_{b} is the slab's negative buoyancy driving the entire system. The portion of the SP shown, of length ℓ_b, is the portion where the bending moment is significant.

3.7 Discussion

The main goal of this study has been to get a clearer picture of the mechanics of subduction, and particularly to explore the role played by the subduction interface. Figure 3.17 is a schematic diagram of the overall dynamical picture that arises from our work.

Consider first the SP and its characteristic velocities V_{Conv} and U_{SP}. Figure 3.17 helps understand the critical role of the subduction interface thickness ratio d_2/h_{SP} that appears in the scaling laws (3.13) for V_{Conv} and (3.12) for U_{SP}. Once the slab's geometrical parameters (θ_0 and ℓ/h_{SP}) are fixed and a certain value of the flexural stiffness ($\mathrm{St} \equiv F_{\mathrm{int}}/F_{\mathrm{D(Slab)}-}$) is obtained, the remaining forces affecting the SP are the drag force $F_{\mathrm{D(SP)}-}$ on its trailing (non-bending) portion and the lubrication forces F_{t} and F_{n} on the interface. However, we saw in § 3.4.2 that the length of the trailing part of the SP, and therefore also the drag force $F_{\mathrm{D(SP)}-}$, has no influence on V_{Conv}. Accordingly, it is mainly the shear force F_{t} that opposes the convergence. Since $F_{\mathrm{t}} \propto \eta_{\mathrm{SI}}/d_2$, V_{Conv} is smaller for a thinner (stronger) lubrication gap and larger for a thicker (weaker) one. Turning now to U_{SP} we recall that this velocity, unlike V_{Conv}, does depend on the trailing plate length and hence also on $F_{\mathrm{D(SP)}-}$. More precisely, U_{SP} is influenced by the sum of $F_{\mathrm{D(SP)}-}$ and the horizontal resultant of the lubrication forces F_{t} and F_{n}. Thus, again, lower values of d_2 will generally decrease U_{SP}, while higher ones will increase it.

Table 3.5. Horizontal speed ratio of the configurations shown in § 3.4.2 fig. 3.9

Points	L_{SP}/L_{OP}	U_{SP}/U_{OP}
★, ☆	2	0.49
■, □	4	0.38

In the derivation of the scaling law (3.12) for U_{SP}, two other interesting features have emerged. The first is that U_{SP}, unlike V_{Conv}, depends also on the horizontal speed of the OP as explained in § 3.4.2. It follows that two different geometrical configurations will have the same value of U_{SP} only if the value of U_{OP} does not change, i.e., if U_{SP}/U_{OP} is constant. This explains why the ratio L_{SP}/L_{OP} appears in the scaling law (3.12). Among the forces acting on the OP, the only one that depends on L_{OP} is the resisting drag $F_{D(OP)-}$, since the driving shear force $F_{D(OP)+}$ is determined by the mantle return flow within the wedge and is always confined to the forearc region of the OP. Thus when we vary L_{SP} or L_{OP} with all other geometrical parameters held constant, only the two drag forces that oppose the motion of the two horizontal plates change. Accordingly, configurations with the same ratio L_{SP}/L_{OP} will also have the same ratio $F_{D(SP)-}/F_{D(OP)-}$ and, consequently, a constant speed ratio U_{SP}/U_{OP}. This is confirmed by table 3.5 for the configurations with different values of L_{SP}/L_{OP} that were shown in § 3.4.2, fig. 3.9.

The second noteworthy aspect of the scaling law (3.12) is the near-perfect logarithmic dependence of U_{SP} on the ratio L_{SP}/ℓ. Although U_{SP} is still correlated with the negative buoyancy ($F_b \propto \ell$) that drives the plate and with the resisting drag force measured by the plate length L_{SP}, the dependence between these two quantities turns out to be surprisingly weak, namely logarithmic. This feature seems to agree with observations in nature, where the speeds of plates attached to subducting slabs are poorly correlated with their lengths (Conrad & Hager, 1999a).

Turning now to the OP, our first result concerns the forces that drive its motion. Some studies (e.g. Chen *et al.*, 2015) conclude that the interplate lubrication force, depending on the configuration of the system, may drive, rather than resist, the motion of the OP. However, we find that the opposite is always the case. As shown in fig. 3.2c (inset), the subduction interface evolves so that it is narrower at the bottom than at the top. The downgoing plate therefore drags fluid from the wider to the narrower part of the gap. According to lubrication theory, this is just the condition for the existence of a positive pressure within the gap, which is what keeps the two plates apart. Accordingly, the normal force in the gap resists, rather than drives, the leftward motion of the OP, regardless of the geometry of

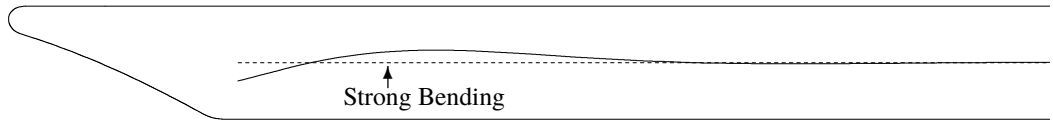

Figure 3.18. Deformation of the OP midsurface. The dashed line represents the initial shape of the midsurface, while the solid line indicates its new position after one time step. The vertical displacement of the midsurface has been exaggerated by a factor ~ 10^2. The model is the case ℓ/h_{SP} = 5, θ_0 = 30° shown in fig. 3.13 (at the bottom).

the plates or the initial gap thickness. The role of the gap thickness is underlined by fig. 3.10a, which shows that U_{OP} decreases as the lubrication force increases with decreasing d_2. Now, since $F_{D(OP)-}$ represents an additional resisting force associated with the mantle flow below most of the OP, we conclude that the sole driving force is the shear force $F_{D(OP)+}$. This force is related to the vertical gradient of horizontal velocity beneath the forearc region of the OP (visible in fig. 3.11). This means that the only way to increase U_{OP} is to increase the slab length ℓ, which leads to a more vigorous return flow below the OP and a larger $F_{D(OP)+}$.

A second result concerns the mechanism of deformation of the OP. According to thin viscous-sheet theory, the deformation of a thin sheet occurs by a combination of stretching/shortening and bending. The relative importance of these two deformation modes is measured by the rates of viscous dissipation of energy (ϕ_s and ϕ_b, respectively) associated with them. Calculating these as a function of arclength along the midsurface of the OP, we found the general pattern shown in fig. 3.15. Within a distance 1-1.5h_{SP} from the trench (s = 0-0.5h_{SP}) the deformation is always dominated by compression. This is due to the opposing actions of the (rightward) horizontal resultant of the interplate lubrication force and the (leftward) driving shear force below the forearc region. Further from the trench, bending usually becomes dominant (fig. 3.18). The exception is for larger values of the slab length ℓ and the initial dip θ_0, for which compression may dominate over bending everywhere. This is seen in table 3.6, where the case ℓ/h_{SP}=7 and θ_0= 60° has no region dominated by bending.

Still further from the trench, in the back-arc region of the OP, both compression and bending are negligible if the OP is neutrally buoyant (Γ = 0). However, when the OP is positively buoyant (Γ < 0), significant stretching of the back-arc region occurs (fig. 3.14, at the top). In particular, a simple lubrication-theory model for an isolated OP (Appendix A) shows that the dimensionless stretching rate Δ of the back-arc region is

$$\Delta = -\frac{d_1\Gamma}{4\lambda_2}, \tag{3.20}$$

Table 3.6. Length of the OP midsurface that identifies the width of the OP zone where the deformation is bending-dominated. We report 4 different ℓ/h_{SP}, θ_0 pairs. The other parameters of the model are the ones corresponding to the cases shown in fig. 3.13.

ℓ/h_{SP}	θ_0	Width
5	30°	$s \in [0.5 - 2.5]$
5	60°	$s \in [0.8 - 2.5]$
7	30°	$s \in [1.5 - 3.0]$
7	60°	none

which is positive (extensional) if $\Gamma < 0$. This result is only indicative because the model of an isolated OP treated in Appendix A ignores the substantial shear traction generated below the forearc region of the OP by the slab-induced mantle flow. Nevertheless, eq. (3.20) is consistent with the fact that back-arc extension only occurs in numerical solutions when $\Gamma < 0$. A similar result has been reported by Holt *et al.* (2015) for a model in which the upper surface of the OP is itself a free-slip surface. We show in Appendix B that the horizontal extensional stress found numerically by Holt *et al.* (2015) agrees almost exactly with the prediction of a simple plug-flow model for a spreading viscous gravity current.

The last result regarding the OP deformation concerns the influence of the subduction interface. Our model confirms the short-range nature of the lubrication forces that develop within the subduction interface, as also reported by Duarte *et al.* (2013) and Chen *et al.* (2015). In particular, fig. 3.14 (at the bottom) shows that varying the thickness of the lubrication layer (i.e. the magnitude of the lubrication forces)influences both the shortening and the bending of the OP, but only in the forearc region.

In conclusion, we compare the range of values of the dimensionless interface strength γ constrained by our work with values assumed in or constrained by other published subduction models. As shown in table 3.7, these values vary by a factor $90/0.13 \sim 700$, with our inferences (2.0-6.3) being squarely in the middle of the range. Two important aspects of the numbers in table 3.7 require some comments.

First, we note that three studies (denoted by asterisks) infer values of γ from natural data. Of these, the study of Duarte *et al.* (2015) stands out on account of its very large estimate $\gamma \approx 90$. However, in this study there is a large uncertainty concerning the characterization of the interface between the two plates. The laboratory experiment starts with the two plates separated by a horizontal distance $d_{2H} \sim 1$ cm that is comparable to the thickness $h_{\mathrm{SP}} \sim 1.6$ cm of the SP. As subduction proceeds, the two plates move closer together, until they are separated by a thin (≈ 1 mm) interface when the SP approaches the bottom of the tank. The

Table 3.7. Dimensionless interface strength of different subduction models. The asterisk indicates studies where γ has been inferred by comparison with observed geophysical data. N=Numerical, E=Experimental. The work of Klein *et al.* (2016) is based on the inversion from GPS data.

Study	Type	γ	λ_1	Rheology
This study*	N	1.97-6.25	150-450	Linear
Meyer & Schellart (2013)	E	0.13-0.43	200	Linear
Duarte *et al.* (2015)*	E	≤ 90	160	Linear (visco-plastic interface)
Chen *et al.* (2015)	E	5.3-10.00	200	Linear (visco-plastic interface)
Holt *et al.* (2015)	N	0.73-1.80	100-2000	Visco-plastic
Klein *et al.* (2016)*	N	0.17-1.3	Elastic lithosphere	Visco-elastic asthenosphere

ratio d_2/h_{SP} thus varies within a range $[0.06, 0.63]$ in the course of the experiment. The value $\gamma \approx 90$ in table 3.7 is calculated for the smallest value of $d_2/h_{SP} = 0.06$.

Second, when plate velocities observed in nature are used to infer γ the assumed value of the viscosity ratio λ_1 between the SP and the mantle is critical (Duarte *et al.*, 2015). This is clear in fig. 3.16, where the point of intersection between the horizontal lines (= real velocity of the transect) and the curves for different λ_1 varies significantly. This can be explained using the scaling law (3.13) for the convergence speed of the SP. Once the slab's geometry is fixed, V_{Conv} depends on the flexural stiffness St and the ratio d_2/h_{SP} (or γ if we also take into account the viscosity ratio η_{SI}/η_0). Now since the geometry is fixed, eq. (3.7) shows that St depends only on λ_1, because the bending length ℓ_b itself does (Ribe, 2010). We can therefore write

$$V_{Conv} = \text{fct}\,(\lambda_1, \gamma) \tag{3.21}$$

for a model configuration where the geometry is known. Thus, if we fix V_{Conv} to a value obtained from natural data, the value of λ_1 will be crucial in determining the corresponding value of γ. In physical terms, lower values of λ_1 speed up the SP so that a stronger interface (higher γ) is needed for a given V_{Conv}, and vice versa. Accordingly, a better constraint on the interface strength of real subduction zones requires a more precise knowledge of the viscosity ratio between the SP and the underlying mantle.

3.8 Conclusions

In this work we studied the dynamics of subduction by means of a numerical model based on the boundary-element method (BEM). Systematically interpreting the results in the light of thin-viscous sheet theory, we explored the kinematics of the SP and the deformation of the OP, particularly focusing on the influence of the subduction interface on those aspects.

Regarding the kinematics of the SP, we first found a scaling law that describes the convergence speed of the descending slab. Neither the length of the SP nor that of the OP influences the convergence rate, which is instead controlled by the slab's shape, the flexural stiffness St of the plate, and the strength of the subduction interface. The convergence rate increases as either the stiffness of the plate or the strength of the subduction interface decreases. Next, we considered the horizontal speed U_{SP} of the flat portion of the plate. For the case of an isolated SP, U_{SP} obeys the scaling law $U_{\mathrm{SP}}/V_{\mathrm{Stokes}} = \alpha(\mathrm{St}) + \beta(\mathrm{St})\log(L_{\mathrm{SP}}/\ell)$, where α and β are logarithmic functions of St. Adding the OP to the system, the scaling law becomes rather complex, with both the strength of the interface and the length of the OP now being dynamically relevant. However, numerical solutions still show a perfect logarithmic dependence of $U_{\mathrm{SP}}/V_{\mathrm{Stokes}}$ on L_{SP}/ℓ. This very weak correlation between plate speed and plate length for plates attached to subducting slabs seems to be in agreement with natural observations.

Turning to the OP, we found a three-zone pattern of deformation that is similar for the majority of cases we explored. Close to the trench, the OP is always under strong compression due to the opposing actions of the horizontal resultant of the lubrication force within the subduction interface and the shear force below the forearc region of the OP. The latter force derives from the mantle return flow and is the sole force driving OP motion. Further from the trench is a second zone of deformation dominated by bending, except for long subducting slabs and steep subduction angles for which compression continues to dominate. Finally, significant extension appears in the back-arc region when the OP is positively buoyant, a result that we explained using simple analytical thin-layer models.

We concluded by using the BEM model to constrain the interface viscosity η_{SI} of a natural subduction zone, the central portion of the Aleutian subduction zone. For a realistic range of values of the viscosity ratio between the SP and the underlying mantle, we found $\eta_{\mathrm{SI}} = 0.96 - 1.72 \times 10^{20}$ Pa s for a corresponding range of mantle viscosities $\eta_0 = 3.92 - 6.95 \times 10^{20}$ Pa s.

Chapter 4

Energetics of subduction and large-scale mantle convection

In this chapter I present the results of the work: Gerardi G., Ribe N. M., & Tackley P. J. Plate bending, energetics of subduction and modeling of mantle convection: a boundary element approach. The manuscript is currently under review for *Earth and Planetary Science Letters*. Together with the 'Introduction' section, here I omit also the 'Model setup and BEM formulation' section included in the original version of the manuscript.

In this chapter we look at the energetics of subduction using the BEM model presented in § 3.2. We begin by performing a scaling analysis of instantaneous solutions of the Stokes equations for plates with a specified geometry. Here, we find that the fraction R of the total energy dissipation that occurs in the upper convective boundary layer is controlled by three key parameters: the flexural stiffness of the SP, the strength of the subduction interface and the shape (dip) of the descending slab. Next, we examine the time evolution of $R(t)$ during unsteady subduction of plates with medium/high viscosity. Time dependent solutions show that R remains always below 0.5, the value corresponding to equipartition of the dissipation between the boundary layer and the ambient mantle. In conclusion, we explore the consequences of this result for the Nusselt number/Rayleigh number relationship $\mathrm{Nu} \sim \mathrm{Ra}_\mathrm{m}^{\beta}$ for a convecting system with plates of moderate to high strength. A crucial result here is that the exponent β can change dramatically depending on the length scale used to describe the dissipation due to bending of the SP.

4.1 Rates of viscous dissipation of energy

The main goal of this work is to quantify the amount of energy dissipated in a subduction zone and to understand how that dissipation is partitioned among the different elements of the system. Accordingly, we write the total dissipation rate D_{Total} as a sum of four contributions, viz.,

$$D_{\text{Total}} = D_{\text{SP}} + D_{\text{OP}} + D_{\text{SI}} + D_{\text{M}} \tag{4.1}$$

where the terms on the right-hand side represent the rates of viscous dissipation due to the deformation of the subducting plate (D_{SP}), the overriding plate (D_{OP}), the subduction interface (D_{SI}) and the ambient mantle (D_{M}).

Consider first the total dissipation rate D_{Total}. The balance of mechanical energy for a Stokes flow in a volume V bounded by a surface S is

$$2\eta \int_V e_{ij} e_{ij} dV = \int_S u_i \sigma_{ij} n_j dS + \int_V u_j f_j \mathrm{d}V. \tag{4.2}$$

Eq. (4.2) states that the total rate of dissipation in a volume V (left-hand side) is the sum of the rate at which the fluid stress σ_{ij} does work on S (first term on the right-hand side) plus the rate at which the gravitational body force $f_j = -\rho g \delta_{j3}$ does work on V (second term). Now introduce the modified pressure $\bar{p} = p + \rho g x_3$ and the corresponding modified stress tensor $\bar{\sigma}_{ij} = -\bar{p}\delta_{ij} + 2\eta e_{ij} = \sigma_{ij} - \rho g x_3 \delta_{ij}$. Eq. (4.2) then takes the simpler form

$$2\eta \int_V e_{ij} e_{ij} dV = \int_S u_i \bar{\sigma}_{ij} n_j \mathrm{d}S, \tag{4.3}$$

which states that the total rate of viscous dissipation in V is equal to the rate at which the modified stress performs work on S. For the three-fluid domain with a free-slip upper surface shown in figure 3.1,

$$D_{\text{M}} + D_{\text{SI}} = \int_{C_1} u_i \bar{\sigma}_{ij}^{(0)} (-n_j) dC + \int_{C_2} u_i \bar{\sigma}_{ij}^{(0)} (-n_j) \mathrm{d}C, \tag{4.4a}$$

$$D_{\text{SP}} = \int_{C_1} u_i \bar{\sigma}_{ij}^{(1)} n_j \mathrm{d}C, \quad D_{\text{OP}} = \int_{C_2} u_i \bar{\sigma}_{ij}^{(2)} n_j \mathrm{d}C, \tag{4.4b}$$

where $\bar{\sigma}_{ij}^{(i)}$ (i=0,1 or 2) is the modified stress tensor of fluid i. The quantity $-n_j$ appears in (4.4a) because the normal vector that points out of the volume S_0 is opposite to $\mathbf{n}$, which was defined as pointing out of the plates. Now substitute eq. (4.4) into eq. (4.1) and apply the normal stress matching conditions $\left(\bar{\sigma}_{ij}^{(k)} -\right.$

$\bar{\sigma}_{ij}^{(0)}\big)n_j = n_i\Delta\rho_k g y_j$ for points on C_k ($k = 1$ or 2). The result is

$$D_{\text{Total}} = \Delta\rho_1 g \int_{C_1} u_i n_i y_j \mathrm{d}C + \Delta\rho_2 g \int_{C_2} u_i n_i y_j \mathrm{d}C. \tag{4.5}$$

Because we know (i.e., have calculated) the velocity $\mathbf{u}$ on C_1 and C_2, (4.5) implies that the total dissipation rate can be obtained simply by evaluating two integrals over the fluid/fluid interfaces. In this study, however, we shall assume a neutrally buoyant OP ($\Delta\rho_2 = 0$), whereupon the second integral in (4.5) vanishes.

We now turn to the dissipation rates D_{SP} and D_{OP} within the two plates. In principle these could be calculated from (4.3). However, determination of the stress $\bar{\sigma}_{ij}$ on C_1 and C_2 requires the solution of Fredholm integral equations of the first kind, which are notorious for their numerical instability. Accordingly, we exploit thin viscous-sheet theory (see table 2.1 in § 2.3.3) to write

$$D_{\text{SP}} = \int_0^{L_{\text{SP}}+\ell} \left(4\eta_1 h_{\text{SP}}\Delta^2 + \frac{1}{3}\eta_1 h_{\text{SP}}^3 \dot{K}^2\right) \mathrm{d}s, \tag{4.6a}$$

$$D_{\text{OP}} = \int_0^{L_{\text{OP}}} \left(4\eta_2 h_{\text{OP}}\Delta^2 + \frac{1}{3}\eta_2 h_{\text{OP}}^3 \dot{K}^2\right) \mathrm{d}s, \tag{4.6b}$$

where Δ is the rate of stretching of the midsurface of the sheet and $\dot{K}$ is its rate of change of curvature. The total rate of dissipation within each plate is thus the sum of contributions from deformation by stretching/shortening ($4\eta h\Delta^2$) and by bending ($1/3\eta h^3\dot{K}^2$). The quantities Δ and $\dot{K}$ are calculated by numerical differentiation of the velocity $\mathbf{u}$ on the sheet's midsurface as shown in § 2.3.2.

Next, we calculated the rate of viscous dissipation within the SI from the integral

$$D_{\text{SI}} = 2\eta_0 \int_{A_{\text{SI}}} e_{ij} e_{ij} dA_{\text{SI}}, \tag{4.7}$$

where A_{SI} is the area of the fluid in the lubrication gap between the plates. We evaluated the integral (4.7) by assuming that the fluid velocity varies linearly across the gap between the known values on either side.

Finally, the rate of viscous dissipation in the ambient mantle (D_{M}) is obtained from eq.(4.1) once all the other quantities are known.

4.2 Scaling analysis

In this section we determine the crucial dimensionless parameters that control the energetics of subduction by performing a scaling analysis of instantaneous BEM solutions. Because inertia is negligible in Stokes flow, the energetic state of the

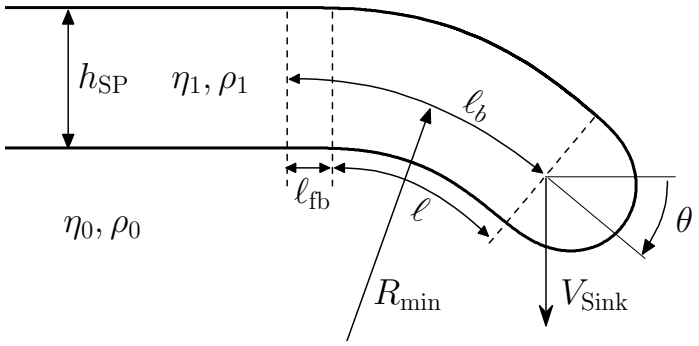

Figure 4.1. Close-up view of the portion of an isolated SP that deforms by bending. Its characteristic length is the bending length ℓ_b, which is the sum of the slab length (ℓ) and width of the zone of flexural bulging (ℓ_{fb}). The minimum raidus of curvature of the plate's midsurface is R_{min}.

system at any instant is fully determined by the geometry of the plates at that instant. Time is therefore a mere parameter, which we here ignore by focussing on the instantaneous geometry shown in figure 3.1.

As a target parameter for our scaling analysis, we define the 'dissipation ratio' R

$$R = \frac{D_{SP} + D_{OP} + D_{SI}}{D_{Total}} \equiv \frac{D_{BL}}{D_{Total}}. \tag{4.8}$$

R is the fraction of the total energy dissipation that occurs in the upper convective boundary layer comprising the two plates plus the SI.

4.2.1 Subduction of an isolated SP

For simplicity we begin by considering the subduction of an isolated SP without an OP or a SI, for which $D_{BL} \equiv D_{SP}$. We call this the SP ONLY case.

Figure 4.1 shows a close-up view of the portion of the SP that deforms by bending. The characteristic length of this portion is the bending length ℓ_b, which is the sum of the length ℓ of the slab and the width ℓ_{fb} of the region seaward of the trench where flexural bulging occurs (Ribe, 2010). If the SP sinks with a characteristic speed V_{Sink}, its rate of change of curvature scales as $\dot{K} \sim V_{Sink}/\ell_b^2$. Neglecting the dissipation due to stretching and integrating over the bending length, we see that (4.6a) implies

$$D_{SP} \sim \eta_1 h_{SP}^3 \left(\frac{V_{Sink}^2}{\ell_b^3}\right) f_1(\theta). \tag{4.9}$$

The unknown function $f_1(\theta)$ accounts for the influence of the shape of the midsurface of the SP on the slab's sinking speed (Ribe, 2010). Next, we estimate

the total dissipation rate in the ambient mantle by scaling (4.2). This yields

$$D_{\mathrm{M}} \sim \eta_0 V_{\mathrm{Sink}}^2 \mathrm{f}_2(\theta), \tag{4.10}$$

which is obtained using the scales $e_{ij} \sim V_{\mathrm{Sink}}/\ell_b$ and $A_{\mathrm{M}} \sim \ell_b^2$. Like (4.9), it contains an unknown function $\mathrm{f}_2(\theta)$.

Now because $D_{\mathrm{BL}} = D_{\mathrm{SP}}$ and $D_{\mathrm{Total}} = D_{\mathrm{SP}} + D_{\mathrm{M}}$, equations (4.9), (4.10) and (4.8) imply

$$R \sim \frac{\mathrm{St}}{\mathrm{St} + \mathrm{F}(\theta)}, \tag{4.11}$$

where $\mathrm{F}(\theta) = \mathrm{f}_2(\theta)/\mathrm{f}_1(\theta)$ and $\mathrm{St} \equiv \eta_1/\eta_0 \, (h_{\mathrm{SP}}/\ell_b)^3$ is the flexural stiffness of the SP that measures its mechanical resistance to bending (Ribe, 2010).

Let us now test the scaling law (4.11) against our BEM solutions. To do this, we run a large number of models for three values of θ_0 and different values of ℓ/h_{SP}, $L_{\mathrm{SP}}/h_{\mathrm{SP}}$ and $\lambda_1 \equiv \eta_1/\eta_0$, computing for each case the flexural stiffness St and the dissipation number R. The results are shown in figure 4.2. The solid symbols show results for which the bending contribution to D_{SP} exceeds 95%. These collapse onto three master curves, one for each value of θ_0, thereby confirming the scaling law (4.11). In the limit of $\mathrm{St} \gg 1$, where we can suppose $\mathrm{St} \gg \mathrm{F}(\theta_0)$, R tends to a constant value that is independent of θ_0, as expected from eq. (4.11). Open symbols, shown for completeness, are for models with a significant ($\geq 5\%$) stretching contribution to D_{SP}, and for that reason obey less well the scaling law (4.11).

The three master curves in figure 4.2 highlight two other interesting features. First, they tell us something about the temporal evolution of the system. In particular, the curves show that R increases if either St or θ_0 increases. Now, during unsteady subduction, St decreases because the slab length increases, whereas θ_0 increases because the slab gets steeper. We therefore expect the system to evolve as indicated by the thick green arrow. We will verify this later during our analysis of time-dependent BEM solutions. Second, the curves show that R never exceeds 0.7 and is typically < 0.5. The latter value represents the 'equipartition limit', where the dissipation is equally shared between the mantle and the plate. Only stiff plates exceed this limit.

4.2.2 Subduction below an OP

We add now the OP to the system. For this SP+OP case, $D_{\mathrm{BL}} \equiv D_{\mathrm{SP}} + D_{\mathrm{OP}} + D_{\mathrm{SI}}$. We expect the OP to have two opposite effects on the dissipation ratio. On the

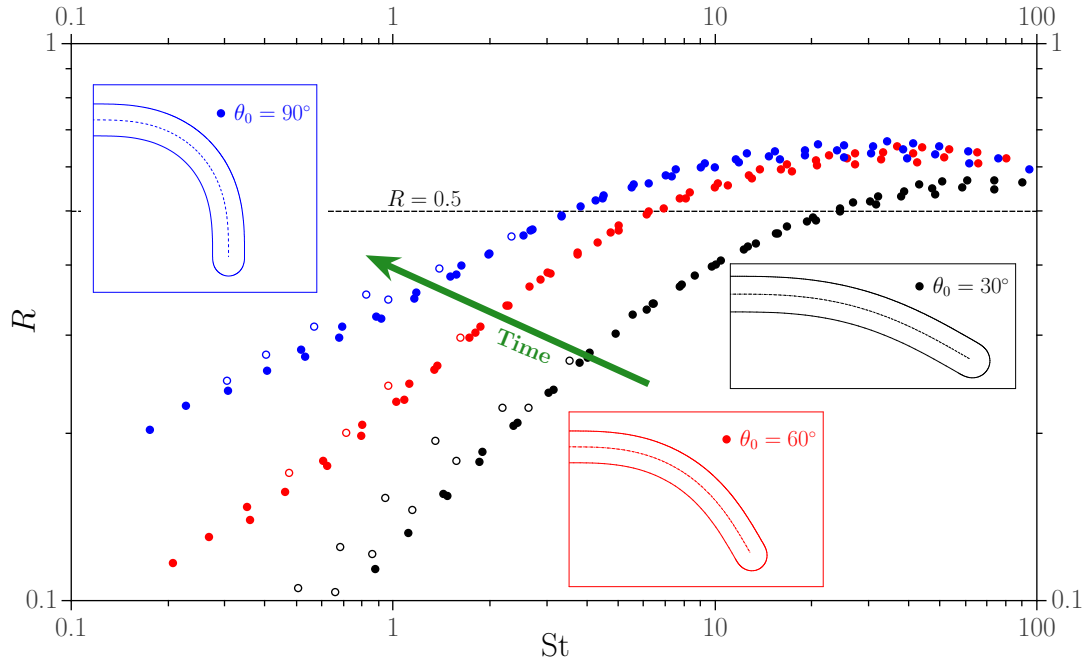

Figure 4.2. Dissipation ratio R as a function of the flexural stiffness St of the SP, predicted by BEM numerical solutions for $\lambda_1 \in [150 - 10^5]$, $\ell/h_{SP} \in [5 - 10]$, $L_{SP}/h_{SP} \in [20 - 32]$ and dip angles $\theta_0 = 30°$(black circles), $60°$(red circles) and $90°$(blue circles). The three insets show the geometry of the plate corresponding to each value of θ_0. Empty circles indicate solutions for which dissipation by stretching of the plate is more than 5% of the total dissipation rate D_{SP}. The green arrow labelled 'Time' indicates the expected time evolution of the system.

one hand, it should increase R because deformation of the subduction interface and of the OP itself leads to higher dissipation within the boundary layer. On the other hand, the OP acts as a no-slip boundary condition on the mantle fluid below, enhancing the dissipation in that region and decreasing R. The inset of figure 4.3 shows a close-up view of the subduction interface (lubrication gap), which has thickness d_2, inclination angle θ_{SI}, and viscosity η_{SI}. Assuming that layer-parallel shear in the gap gives the largest contribution to viscous dissipation, we use (4.7) to scale D_{SI} as

$$D_{\mathrm{SI}} \sim \eta_{\mathrm{SI}} V_{\mathrm{Conv}}^2 \left(\frac{h_{\mathrm{SP}}}{d_2}\right) \sin\left(\theta_{\mathrm{SI}}\right)^{-1}, \tag{4.12}$$

where V_{Conv} is the convergence speed of the descending slab. In writing (4.12), we have assumed that $e_{ij} \sim V_{\mathrm{Conv}}/d_{\mathrm{SI}}$ and $A_{\mathrm{SI}} \sim d_2 h_{\mathrm{SP}}/\sin\left(\theta_{\mathrm{SI}}\right)$. We defined V_{Conv} to

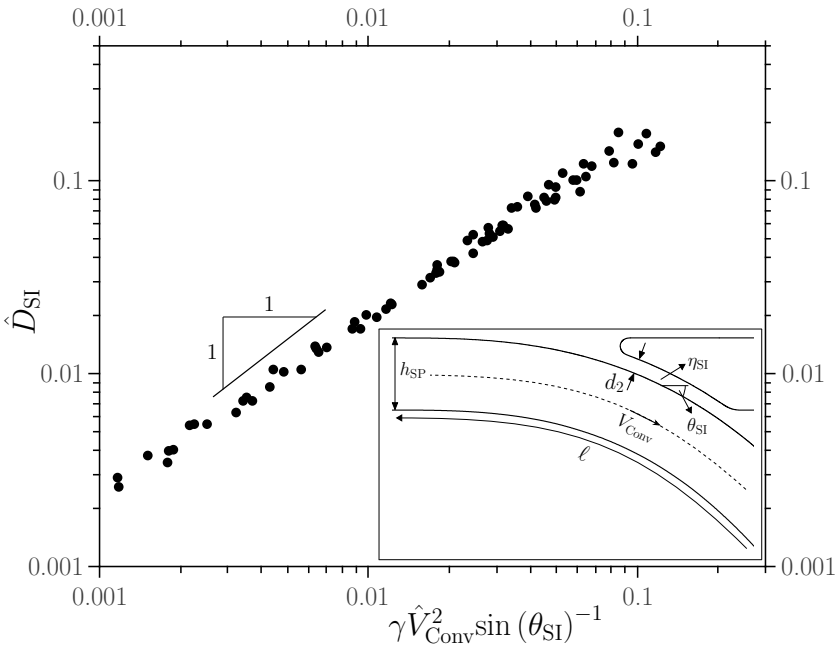

Figure 4.3. Dimensionless subduction interface dissipation rate D_{SI} as a function of the group of parameters on the right-hand side of eq. (4.13), for 108 BEM solutions with $\lambda_1 \in [150 - 10^5]$, $\lambda_2 = 250$, $\ell/h_{\mathrm{SP}} \in [5 - 10]$, $L_{\mathrm{SP}}/h_{\mathrm{SP}} = L_{\mathrm{OP}}/h_{\mathrm{OP}} = 20$, $\gamma \in [2 - 6]$ and $\theta_0 = 60°$. The range of γ used corresponds to that inferred by Gerardi & Ribe (2018) for the central Aleutian subduction zone. Different values of θ_0 shift the curve horizontally. Inset: close-up view of the subduction interface, defined by its thickness d_2, inclination θ_{SI} and viscosity η_{SI}, where $\eta_{\mathrm{SI}} \equiv \eta_0$ for our model. V_{Conv} is the convergence speed of the descending slab.

be the tangential component of the velocity vector on the SP's midsurface where it intersects the depth $x_2 = -h_{\mathrm{SP}} - d_1$ (see inset of figure 4.3). To verify (4.12), we compare it with the predictions of a large number of BEM solutions that include

an OP. For this purpose, we rewrite (4.12) in dimensionless form as

$$\hat{D}_{\mathrm{SI}} \sim \gamma \hat{V}_{\mathrm{Conv}}^2 \sin\left(\theta_{\mathrm{SI}}\right)^{-1}, \tag{4.13}$$

where

$$\hat{D}_{\mathrm{SI}} = \frac{\eta_0}{h_{\mathrm{SP}}^4 \left(g\Delta\rho_1\right)^2} D_{\mathrm{SI}}, \qquad \hat{V}_{\mathrm{Conv}} = \frac{\eta_0}{h_{\mathrm{SP}}^2 \left(g\Delta\rho_1\right)} V_{\mathrm{Conv}}, \qquad \gamma = \frac{\eta_{\mathrm{SI}}}{\eta_0} \frac{h_{\mathrm{SP}}}{d_2}. \tag{4.14}$$

The quantity γ is the dimensionless strength of the SI (Gerardi & Ribe, 2018). Because $\eta_{\mathrm{SI}} = \eta_0$ in our model, we explore the influence of γ by varying d_2 alone (Gerardi & Ribe, 2018). Figure 4.3 shows $\hat{D}_{\mathrm{SI}}$ as a function of $\gamma \hat{V}_{\mathrm{Conv}}^2 \sin\left(\theta_{\mathrm{SI}}\right)^{-1}$ for 108 BEM solutions for the ranges of parameters given in the caption of figure 4.3. All the points collapse onto a straight line with slope of unity, confirming the scaling law (4.13).

Turning now to the rate of dissipation within the OP, our BEM solutions show that the energy dissipated to deform the OP is never more than $0.03 D_{\mathrm{BL}}$, whatever system configuration we use. We can therefore safely assume $D_{\mathrm{BL}} \approx D_{\mathrm{SP}} + D_{\mathrm{SI}}$ for our SP+OP case study.

A natural next step would be to determine a complete scaling law for R that includes the effect of the SI and that reduces to (4.11) in the limit $\gamma = 0$ of an infinitely weak (i.e., thick) SI. However, this turns out to be impractical given the large number of parameters involved. Instead, we show in figure 4.4 how the value of γ influences the dissipation ratio R. Dissipation in the SI can enhance R significantly, but only for low values of the SP's flexural stiffness ($\mathrm{St} \ll 1$). In this limit, D_{SI} can exceed D_{SP} by a factor of two or more. However, as soon as St increases beyond ≈ 2, the effect of γ vanishes and we recover to a good approximation the corresponding SP ONLY case (empty circles in figure 4.4). Moreover, in the limit $\gamma \to 0$ we recover the SP ONLY results for all values of the stiffness St.

4.3 Unsteady subduction

Our next task is to explore how R varies during unsteady subduction, focussing on the more realistic SP+OP case. We consider two examples: 'low viscosity' with $\lambda_1 = 250$ and 'high viscosity' with $\lambda_1 = 2500$. The remaining parameters for both examples are given in table 4.1.

We ran the simulations until the slab's tip reached the depth $x_2 = -6.7 h_{\mathrm{SP}}$, keeping track of $R(t)$ and $\mathrm{St}(t)$. The results are shown in figure 4.5 for $\lambda_1 = 250$

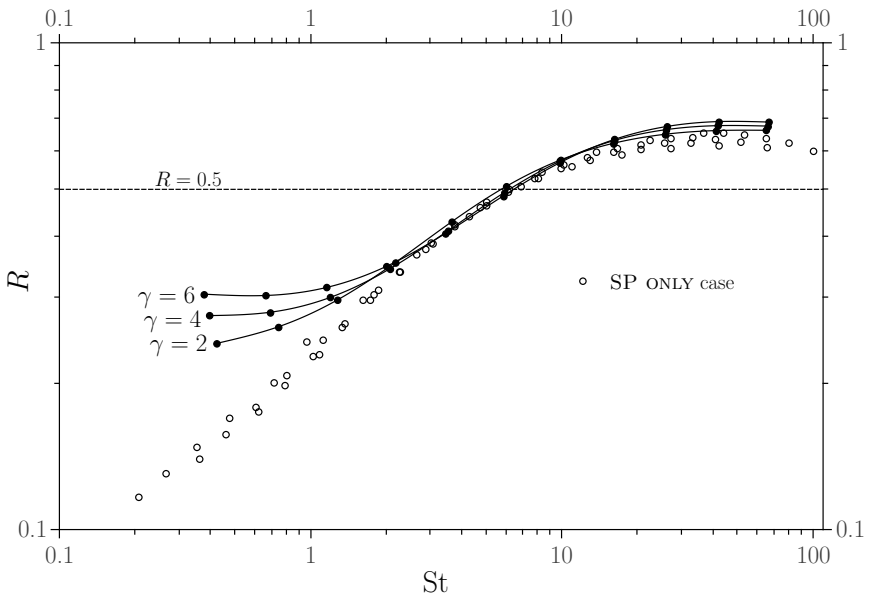

Figure 4.4. Dissipation ratio R as a function of the flexural stiffness St of the SP for three different values of γ. The BEM solutions for the SP+OP system were obtained for $\lambda_1 \in [150 - 10^5]$, $\gamma \in [2 - 6]$, $\ell/h_{SP} = 7$, $\theta_0 = 60°$ and $L_{SP}/h_{SP} = L_{OP}/h_{OP} = 20$. Empty circles trace the corresponding curve for the SP ONLY case with $\theta_0 = 60°$.

Table 4.1. Initial configurations of the models whose time evolutions are shown in figure 4.5.

	SP				OP			
	θ_0	L_{SP}/h_{SP}	ℓ/h_{SP}	λ_1	d_2/h_{SP}	L_{OP}/h_{SP}	h_{OP}/h_{SP}	λ_2
'Low viscosity'	30°	20	5	250	0.25	20	1	250
'High viscosity'	30°	20	5	2500	0.25	20	1	2500

(top) and $\lambda_1 = 2500$ (bottom). Figures 4.5a and 4.5c show the geometry of the system at three characteristic times. Figures 4.5b and 4.5d show the corresponding time evolution of $R(t)$ as a function $\mathrm{St}(t)$ (filled circles). Time increases from right to left along these curves. The fraction D_{SI}/D_{BL} of the boundary-layer dissipation that occurs in the SI is also noted for the three times. Finally, the open circles show $R(\mathrm{St})$ for the same SP but without the OP.

The first important result of figure 4.5 is that R remains always below the value 0.5 corresponding to equipartition of the dissipation between the boundary layer and the ambient mantle. Second, the shapes of the curves concerning the subduction of an isolated SP (figure 4.5b and d, empty circles), which show R increasing as St decreases, agree with what we expected from our earlier SP ONLY solutions (Figure 4.2, § 4.2.1). The behavior of the SP+OP case is more complex (figure 4.5b and d, filled circles). Recall that the temporal evolution of R reflects

a balance between two competing effects: a dynamical one (R decreases as St and D_{SI}/D_{BL} decrease with time) and a geometrical one (R increases as the slab dip increases). For the SP+OP case with $\lambda_1 = 250$, the dynamical effect dominates at first, leading to a steady decrease of R with time. Then, at St ≈ 0.6, the balance is reversed and R starts to increase (figure 4.5b). For $\lambda_1 = 2500$, by constrast, the two effects nearly cancel out, maintaining a constant value $R \approx 0.4$ (figure 4.5d).

Finally, we note that for $\lambda_1 = 2500$ the simulations for the SP+OP and the SP ONLY cases have rather similar variations of R as a function of St, where $2 < \text{St} < 10$. This agrees with the results of figure 4.4, which show that the influence of the OP on the energetics of the system becomes almost negligible for St > 2. This is not the case for $\lambda_1 = 250$, for which the SP+OP and the SP ONLY simulations follow very different paths in the St-R space.

4.4 Parameterized model of mantle convection

We want now to describe the steady-state thermal convection in a cell of length L_h and thickness H (figure 4.6). At the top of cell is the SP which thickens by conductive cooling as it moves toward the trench, reaching a thickness h_{SP} when it enters the subduction zone. We assume no heat sources within the system and we consider a well-mixed mantle (i.e. high mantle Rayleigh numbers, Ra_m) at temperature T_m. The only temperature difference is across the SP, and is $\Delta T = T_m - T_{Surf}$, where T_{Surf} is the temperature at the SP's surface.

We begin by defining the Nusselt number (Nu) of the convection cell as the ratio of the surface heat flow in the presence of convection to that transported purely by conduction (e.g. Turcotte & Schubert, 2014). The numerator is the integral over the length L_h of the vertical temperature gradient predicted by the standard half-space cooling model. The denominator is the heat transported by conduction across the entire thickness of the cell H. We thus have

$$\text{Nu} = 2H \left(\frac{U_{SP}}{\pi \kappa L_h} \right)^{1/2}, \tag{4.15}$$

where κ is the thermal diffusivity and U_{SP} is the horizontal speed of the SP. Scaling the continuity equation in the convection cell, we obtain

$$\frac{U_{SP}}{L_h} \sim \frac{V_{Sink}}{L_z}, \tag{4.16}$$

where L_z is the vertical distance from the slab's tip to the lower surface of the SP

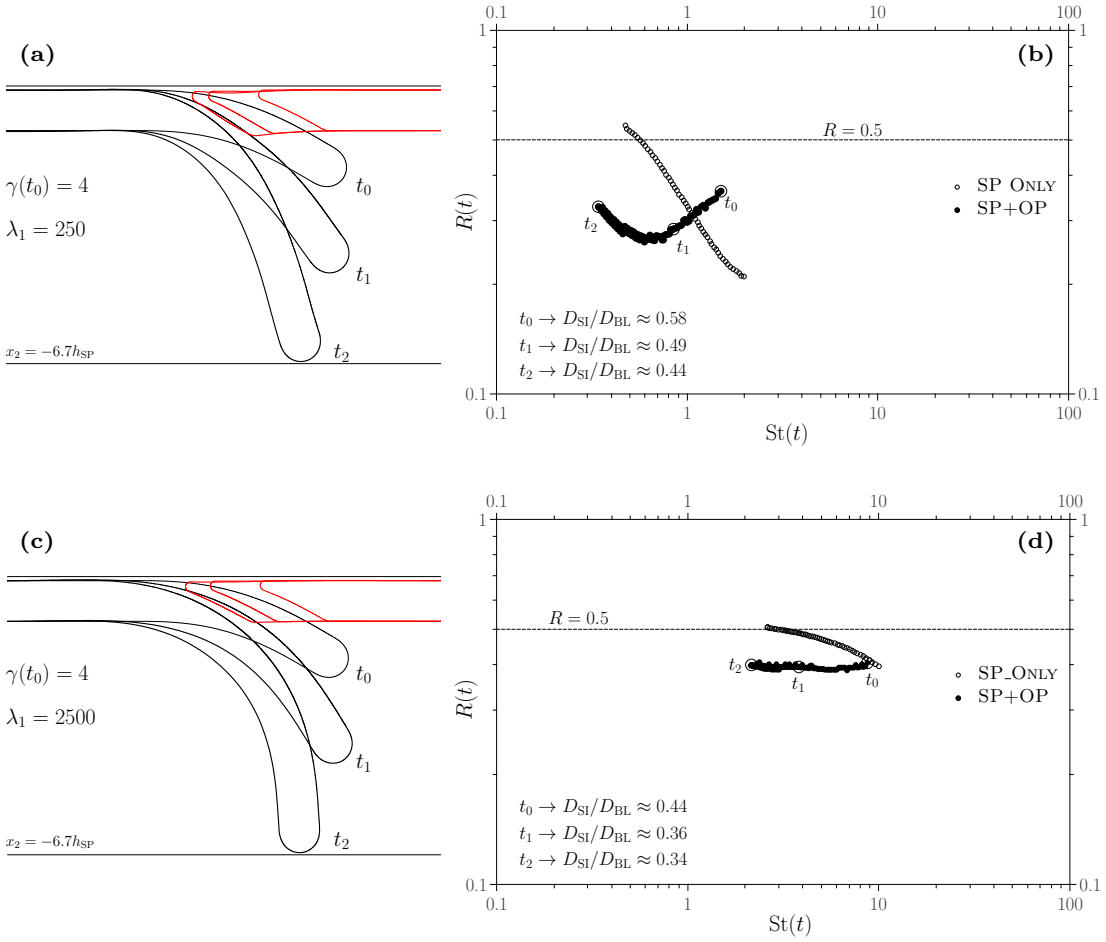

Figure 4.5. Unsteady subduction for two different viscosity ratios of the SP: $\lambda_1 = 250$ (top) and 2500 (bottom). The initial SI strength is $\gamma = 4$ for both cases. **(a)** and **(c)**: system geometry (black line=SP, red line=OP) at three different times t_0 (the initial time), t_1 and t_2. **(b)** and **(d)**: dissipation ratio R as a function of the time-varying flexural stiffness St(t). Also reported is the value of the ratio D_{SI}/D_{BL} at the three times. For comparison, the open circles show R(St) for the same SP but without the OP. Time increases from right to left along these curves.

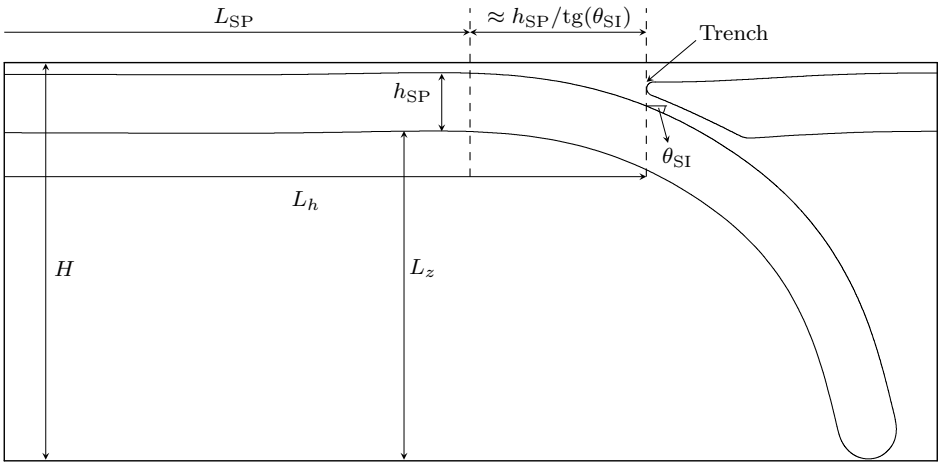

Figure 4.6. Geometrical representation of the convection cell.

(figure 4.6). Equation (4.16) allows us to rewrite (4.15) as

$$\mathrm{Nu} \sim H \left(\frac{V_{\mathrm{Sink}}}{\kappa L_z} \right)^{1/2}. \tag{4.17}$$

The next step is to determine V_{Sink} in terms of the different contributions to the viscous dissipation at the subduction zone. The global balance of mechanical energy is

$$D_{\mathrm{M}} + D_{\mathrm{BL}} \equiv D_{\mathrm{M}} \left(1 + C_{\mathrm{R}}\right) \sim h_{\mathrm{SP}} \ell g \Delta\rho_1 V_{\mathrm{Sink}}, \tag{4.18}$$

where $D_{\mathrm{BL}} \sim C_{\mathrm{R}} D_{\mathrm{M}}$, $C_{\mathrm{R}} \equiv R/(1-R)$, and $D_{\mathrm{Total}} \sim h_{\mathrm{SP}} \ell g \Delta\rho_1 V_{\mathrm{Sink}}$. Making use of (4.10) for D_{M}, we obtain

$$V_{\mathrm{Sink}} \sim \frac{h_{\mathrm{SP}} \ell g \Delta\rho_1}{\eta_0 \mathrm{f}_2(\theta) \left(1 + C_{\mathrm{R}}\right)}. \tag{4.19}$$

Because (4.19) relates the slab's sinking speed to the coefficient C_{R} that describes the partitioning of viscous dissipation between the boundary layer and the mantle, we expect different regimes of mantle convection depending on the value of C_{R}.

4.4.1 Thermal convection dominated by mantle viscous dissipation

In this section we recover the well-known result for the Nusselt number predicted by boundary-layer analysis of an isoviscous system. Here the energy dissipated to deform the lithosphere is negligible (i.e. $D_{\mathrm{M}} \gg D_{\mathrm{BL}}$ and $C_{\mathrm{R}} \to 0$). The thickness of the lithosphere h_{SP} is given by the half-space cooling model as

$$h_{\mathrm{SP}} \sim \left(\frac{\kappa L_h}{U_{\mathrm{SP}}} \right)^{1/2}. \tag{4.20}$$

Substituting (4.16) and (4.19) into (4.20), we obtain

$$\frac{h_{\mathrm{SP}}}{H} \sim \left(\frac{L_z \mathrm{f}_2(\theta)}{\ell \mathrm{Ra}_{\mathrm{m}}} \right)^{1/3}, \tag{4.21}$$

where the Rayleigh number of the entire cell is $\mathrm{Ra}_{\mathrm{m}} \equiv H^3 g \Delta\rho_1/(\kappa\eta_0)$. Then substituting (4.19) into (4.17) and using (4.21), we obtain

$$\mathrm{Nu} \sim {\mathrm{Ra}_{\mathrm{m}}}^{1/3} \left(\frac{\ell}{L_z \mathrm{f}_2(\theta)} \right)^{1/3}, \tag{4.22}$$

which is the standard Nusselt number vs. Rayleigh number scaling for an isoviscous system.

Our next task is to understand what happens when $C_R \neq 0$.

4.4.2 Thermal convection below a strong deforming boundary layer

From the definition $C_R = D_{BL}/D_M$, we observe that

$$C_R \sim \frac{\eta_1}{\eta_0}\left(\frac{h_{SP}}{\ell_b}\right)^3 F(\theta) + \frac{\eta_{SI}}{\eta_0}\left(\frac{h_{SP}}{d_{SI}\sin(\theta_{SI})f_2(\theta)}\right)\left(\frac{V_{Conv}}{V_{Sink}}\right)^2, \tag{4.23}$$

where we have used (4.9), (4.10) and (4.12) to scale the different contributions to the viscous dissipation. Substituting (4.23) into (4.19) we obtain a nonlinear implicit equation for the sinking speed of the slab:

$$V_{Sink} \sim \frac{h_{SP}\ell g\Delta\rho_1}{\eta_0 f_2(\theta)}\left[1 + \frac{\eta_1}{\eta_0}\left(\frac{h_1}{\ell_b}\right)^3 F(\theta) + \frac{\eta_{SI}}{\eta_0}\left(\frac{h_{SP}}{d_{SI}\sin(\theta_{SI})f_2(\theta)}\right)\left(\frac{V_{Conv}}{V_{Sink}}\right)^2\right]^{-1}. \tag{4.24}$$

Following the approach of Conrad & Hager (1999b), we define two additional Rayleigh numbers for the SP and the SI:

$$Ra_{SP} \equiv \frac{\ell_b^3 g\Delta\rho_1}{\kappa\eta_1}, \quad Ra_{SI} \equiv \frac{d_{SI}^3 g\Delta\rho_1}{\kappa\eta_{SI}}. \tag{4.25}$$

These Rayleigh numbers measure the importance of viscous dissipation within the SP and the SI relative to the energy available within the system. They become large in the limits $D_{SP} \to 0$ and/or $D_{SI} \to 0$ for fixed h_{SP}, which limits correspond to decreasing viscosity (η_1 or η_{SI}) and/or increasing length scale (ℓ_b or d_{SI}). In terms of these Rayleigh numbers, (4.24) can be written as

$$V_{Sink} \sim Ra_m \frac{h_{SP}\ell\kappa}{f_2(\theta)H^3}\times$$

$$\times\left[1 + \frac{Ra_m}{Ra_{SP}}\left(\frac{h_{SP}}{H}\right)^3 F(\theta) + \frac{Ra_m}{Ra_{SI}}\left(\frac{h_{SP}}{H}\right)\left(\frac{d_{SI}^2}{H^2\sin(\theta_{SI})f_2(\theta)}\right)\left(\frac{V_{Conv}}{V_{Sink}}\right)^2\right]^{-1}. \tag{4.26}$$

We now investigate two limiting cases of (4.26).

Case 1: convection beneath a plate with a short travel time

Consider first the case of a lithosphere that moves from the ridge to the trench in a time $t = L_h/U_{\mathrm{SP}} < 80$ Myr, the age at which seafloor flattening is observed to begin (e.g. Sclater *et al.*, 1980; Conrad & Hager, 1999b). This implies that h_{SP} increases continually according to the half-space cooling model. Suppose initially that the viscous dissipation in the subduction interface is negligible ($\mathrm{Ra_{SI}} \to \infty$). Simplifying (4.26) accordingly and following the same steps as in § 4.4.1, we find

$$\frac{h_{\mathrm{SP}}}{H} \sim \left(\frac{\mathrm{Ra_{SP}}}{\mathrm{Ra_m}} \frac{L_z \mathrm{f}_2(\theta)}{\mathrm{Ra_{SP}}\ell - \mathrm{f}_1(\theta) L_z} \right)^{1/3}. \tag{4.27}$$

Now using (4.27) and the simplified form of (4.26) in eq. (4.17) we obtain

$$\mathrm{Nu} \sim \left(\frac{\ell}{L_z \mathrm{f}_2(\theta)} - \frac{\mathrm{F}(\theta)}{\mathrm{Ra_{SP}}} \right)^{1/3} {\mathrm{Ra_m}}^{1/3}. \tag{4.28}$$

The Nusselt number still scales as ${\mathrm{Ra_m}}^{1/3}$, but the prefactor decreases as the dissipation rate within the SP increases (i.e., as $\mathrm{Ra_{SP}}$ decreases). This result remains valid as long as the denominator of (4.27) is nonzero, i.e., if $\mathrm{Ra_{SP}} \gg \mathrm{f}_1(\theta) L_z/\ell$. This condition follows from the fact that when $\mathrm{Ra_{SP}}$ decreases the convection progressively slows down, increasing the traveling time of the lithosphere. Because the lithosphere then has more time to thicken, $\mathrm{Ra_{SP}}$ decreases even further, triggering a positive feedback that leads to an unphysical infinite plate thickness (Conrad & Hager, 1999b).

To understand the influence of viscous dissipation in the SI, we adopt (4.26) in its full form. Following again the steps in § 4.4.1 and assuming $\mathrm{Ra_{SP}} \gg \mathrm{f}_1(\theta) L_z/\ell$, we obtain

$$\left(\frac{h_{\mathrm{SP}}}{H}\right)^3 - \left(\frac{h_{\mathrm{SP}}}{H}\right)\left(\frac{d_{\mathrm{SI}}^2}{H^2}\frac{A_1}{\mathrm{Ra_{SI}}}\right) \sim \left(\frac{A_2}{\mathrm{Ra_m}}\right), \tag{4.29}$$

where $A_1 \equiv C_{\mathrm{V}}^2 (L_Z/\ell)/\sin(\theta_{\mathrm{SI}})$, $A_2 \equiv (L_Z/\ell)\mathrm{f}_2(\theta)$ and $C_{\mathrm{V}} \equiv V_{\mathrm{Conv}}/V_{\mathrm{Sink}}$. Our BEM simulations show that C_{V} is always less than unity, and we treat it here as a constant. Obtaining representative values of A_1 and A_2 from our BEM solutions, we solve (4.29) numerically for $\mathrm{Ra_{SI}}(d_{\mathrm{SI}}, \eta_{\mathrm{SI}}) \leq 0.4$ and $\mathrm{Ra_m}(H) \in [1.6 \times 10^5 - 1.3 \times 10^6]$. We find that $h_{\mathrm{SP}}/H \sim {\mathrm{Ra_m}}^{1/3}$ and $\mathrm{Nu} \sim {\mathrm{Ra_m}}^{1/3}$ to within a negligible error. We conclude that for convection below a short SP for which the half-space cooling model applies, the scaling law $\mathrm{Nu} \sim {\mathrm{Ra_m}}^{1/3}$ remains valid even in the presence of viscous dissipation in the subduction interface.

Case 2: convection below a plate with a long travel time

We now assume that the travel time of the plate is sufficiently long (> 80 Myr) that thermal thickening has stopped by the time it reaches the trench. The dependence of h_{SP} on $\mathrm{Ra_m}$ then breaks down and h_{SP}/H becomes a simple constant in the model, with h_{SP} always at its maximum value. Nevertheless, we assume that the amount of heat evacuated by the cell still corresponds to the heat lost during the thickening of the plate, while the amount of heat loss occurring after seafloor flattening occurs remains negligible. This implies that (4.17) continues to apply for our analysis.

Considering both contributions D_{SI} and D_{SP} to the viscous dissipation, we substitute (4.26) into (4.17) and obtain

$$\mathrm{Nu} \sim \left[\mathrm{Ra_m} \left(\frac{\ell}{L_z \mathrm{f_2}(\theta)} \right) \frac{h_{\mathrm{SP}}/H}{\underbrace{1 + \frac{\mathrm{Ra_m}}{\mathrm{Ra_{SP}}} \left(\frac{h_{\mathrm{SP}}}{H} \right)^3 \mathrm{F}(\theta) + \frac{\mathrm{Ra_m}}{\mathrm{Ra_{SI}}} \left(\frac{h_{\mathrm{SP}}}{H} \right) \left(\frac{d_{\mathrm{SI}}^2 C_{\mathrm{V}}^2}{H^2 \sin(\theta_{\mathrm{SI}}) \mathrm{f_2}(\theta)} \right)}_{C_{\mathrm{R}}}} \right]^{1/2}, \tag{4.30}$$

where the bracket highlights the definition of C_{R}. We now use (4.30) to determine the value of the exponent β that would appear in the corresponding Nu-$\mathrm{Ra_m^{\beta}}$ relationship. Observing that Nu-$\mathrm{Ra_m^{\beta}}$ implies $\beta = (\mathrm{dNu}/\mathrm{dRa_m})(\mathrm{Ra_m}/\mathrm{Nu})$, we find that (4.30) implies

$$\beta = \frac{1/2}{1 + C_{\mathrm{R}}}. \tag{4.31}$$

Eq. (4.31) shows that β strongly depends on the dissipation partition coefficient C_{R}. We note that also the models showed in Conrad & Hager (1999b) follow equation (4.31).

4.5 Influence of the lengthscales ℓ_b vs. R_{min} on dissipation partitioning

We now show how the estimates of the dissipation partitioning coefficient C_{R} and the heat transport exponent β change dramatically depending on the length scale (ℓ_b or R_{min}) used to characterize the bending response of the SP. We begin by

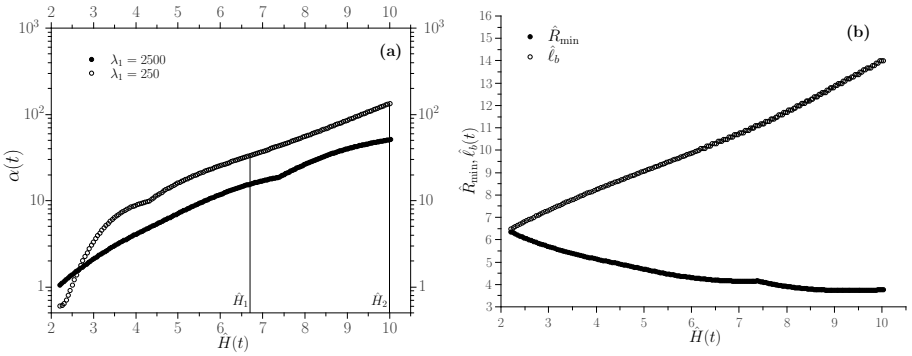

Figure 4.7. **(a)** Overestimation factor α as a function of the dimensionless cell thickness $\hat{H}$ for viscosity ratios $\lambda_1 = 250$ and 2500. Time increases from left to right. The intersections with the vertical straight lines give the values of α for the two characteristic depths $\hat{H}_1$ and $\hat{H}_2$. **(b)** Time evolution of $\hat{R}_{\min}$ (filled circles) and $\hat{\ell}_b$ (empty circles) for $\lambda_1 = 2500$.

defining

$$\alpha \equiv \frac{D_{\mathrm{SP}}|_{R_{\min}}}{D_{\mathrm{SP}}|_{\ell_b}} = \left(\frac{\ell_b}{R_{\min}}\right)^3 \tag{4.32}$$

as the factor by which D_{SP} is overestimated if $R_{\min}$ is adopted instead of ℓ_b, all else being equal. We estimate α in a realistic way by running time-dependent BEM simulations starting from the initial conditions reported in table 4.1. Next, for both the 'low viscosity' and 'high viscosity' cases we stop the simulations at two characteristic depths $H_1/h_{\mathrm{SP}} = \hat{H}_1 = 6.7$ and $H_2/h_{\mathrm{SP}} = \hat{H}_2 = 10.0$. Owing to the quasi-stationarity of Stokes flow, these instantaneous configurations can be assumed to be representative for the purposes of our steady-state analysis.

Figure 4.7a shows that α increases rapidly as the slab progressively sinks, illustrating the strong influence of the chosen length scale in the evaluation of D_{SP}. For the two characteristic depths $\hat{H}_1$ and $\hat{H}_2$, for example, we find $\alpha_1 = 33$ and $\alpha_2 = 134$ respectively when $\lambda_1 = 250$ (empty circles), and $\alpha_1 = 16$ and $\alpha_2 = 51$ respectively when $\lambda_1 = 2500$ (filled circles). The dependence of α on the depth $\hat{H}$ is explained by figure 4.7b, which shows the dimensionless lengths $\hat{\ell}_b$ and $\hat{R}_{\min}$ as functions of $\hat{H}$ for $\lambda_1 = 2500$. As the slab penetrates deeper, the bending length increases while the minimum radius of curvature tends to stabilize to a constant value. The ratio $\ell_b/R_{\min}$, and thus the overestimate of the dissipation D_{SP}, therefore increases with the depth H. For $\lambda_1 = 250$, the gap between the two curves of figure 4.7b becomes even wider, which is why α is larger for the 'low viscosity' case (empty circles, figure 4.7a).

To show how the overestimation of D_{SP} documented above influences the in-

Table 4.2. Values of the coefficient δ, the energetic ratio $C_{\mathrm{R}}|_L$ and the corresponding exponent $\beta|_L$, where $L = \ell_b$ or $R_{\min}$, for four combinations of values of $\hat{H}$ and λ_1.

$\hat{H}$	λ_1	δ	α	$C_{\mathrm{R}}\|_{\ell_b}$	$C_{\mathrm{R}}\|_{R_{\min}}$	$\beta\|_{\ell_b}$	$\beta\|_{R_{\min}}$
6.7	250	0.81	33	0.48	19	0.34	0.03
6.7	2500	0.52	16	0.67	11	0.30	0.04
10.0	250	0.49	134	0.81	90	0.28	≈ 0
10.0	2500	0.62	51	0.97	32	0.25	0.02

ferred value of β, we calculate the quantity

$$C_{\mathrm{R}}|_{R_{\min}} = \left(\frac{\alpha+\delta}{1+\delta}\right) C_{\mathrm{R}}|_{\ell_b}, \tag{4.33}$$

where α, $\delta \equiv D_{\mathrm{SI}}/D_{\mathrm{SP}}|_{\ell_b}$ and $C_{\mathrm{R}}|_{\ell_b}$ are determined from the BEM simulations. The corresponding values of β are then obtained from (4.31). The results are summarized in table 4.2 for our four characteristic combinations of $\hat{H}$ and λ_1. If we use $R_{\min}$ as the bending length scale, the estimate of the boundary-layer dissipation D_{SP} is much higher, resulting in values of β close to zero in all cases. If, however, we adopt the correct length scale ℓ_b, $\beta \in [0.30, 0.34]$ for $\hat{H} = 6.7$ and $\beta \in [0.25, 0.28]$ for $\hat{H} = 10$. This shows that one's assumption about the thickness of the convection cell plays a role in the determination of β.

In light of table 4.2, we conclude that it is crucial to use the dynamic length scale ℓ_b rather than the purely geometric length $R_{\min}$ to characterize the bending response of a viscous plate (Ribe, 2010). This follows from the fact that the bending moment within a viscous plate is proportional to the rate of change of the curvature of its midsurface and not to the curvature itself, as it would be in an elastic plate.

In closing, we remark that the neglect of volumetric heat sources in our parameterized convection model makes it most appropriate for convection in the upper mantle ($H = 670$ km). Internal heating has to be considered in models of whole-mantle convection with $H = 2880$ km (Turcotte & Schubert, 2014).

4.6 Conclusions

In this work we studied the energetics of subduction using a numerical model based on the BEM. We endeavored to shed light on two topics: the partitioning of viscous dissipation among the different elements of a subduction zone (i.e. the subducting plate, the subduction interface and the mantle); and the influence of the energy dissipated in subduction zones on parameterized models of mantle

convection.

By means of a scaling analysis of instantaneous BEM solutions for an isolated SP, we found that the ratio R of the energy dissipated in the upper boundary layer to the total energy dissipation obeys the scaling law $R \sim \mathrm{St}/[\mathrm{St} + \mathrm{F}(\theta)]$, where St (the "flexural stiffness") represents the SP's mechanical resistance to bending and $\mathrm{F}(\theta)$ is a function that accounts for the effect of the dip θ of the descending slab. Adding an OP to the system, we found that R also depends on a third parameter γ, the dimensionless strength of the subduction interface. Turning to unsteady subduction, we observed that the time evolution of $R(t)$ depends on the SP/mantle viscosity ratio λ_1. Nonetheless, for both the 'low viscosity' ($\lambda_1 = 250$) and 'high viscosity' ($\lambda_1 = 2500$) cases explored, we observed that $R(t)$ remains always below the value 0.5 corresponding to equipartition of the dissipation between the boundary layer and the mantle. We conclude that energy dissipation during free subduction is never dominated by the plate bending and interface shearing contributions. Interestingly, we also noticed that the importance of the dissipation in the subduction interface decreases as subduction proceeds.

Turning to the influence of strong subduction zones on mantle convection, we found that it primarily depends on the travel time of the lithosphere from the ridge to the trench. For short travel times ≤ 80 Myr, the thickness h_{SP} of the lithosphere when it enters the subduction zone is described by the classical half-space cooling model and depends on the mantle Rayleigh number $\mathrm{Ra_m}$. The Nusselt number is then $\mathrm{Nu} \sim \mathrm{Ra_m}^{\beta}$ with $\beta = 1/3$, as for an isoviscous mantle. For long travel times, by contrast, h_{SP} is a constant. The heat transfer scaling exponent is then $\beta = 0.5/(1+C_{\mathrm{R}})$, where $C_{\mathrm{R}} \equiv R/(1-R)$ is the ratio of the boundary-layer dissipation rate to that within the surrounding mantle. The partitioning factor C_{R} depends strongly on the length scale one adopts to characterize the bending of the SP. If the minimum radius of curvature R_{min} of the plate is used, as in several previous studies, the bending dissipation of the SP is strongly overestimated and $\beta \to 0$. If however one uses the correct length scale, the "bending length" ℓ_b, $\beta \in [0.30, 0.34]$ for $H/h_{\mathrm{SP}} = 6.7$ and $\beta \in [0.25, 0.28]$ for $H/h_{\mathrm{SP}} = 10$, where H is the depth of the convecting layer. Our overall conclusions are that strong subduction zones do not dominate the viscous dissipation associated with mantle convection, and that subduction zone dissipation leads to relatively small departures from the classical $\mathrm{Nu} \sim \mathrm{Ra_m}^{1/3}$ heat transfer law.

Chapter 5

Laboratory modeling of mantle convection

Together with numerical models, laboratory experiments have long played a central role in mantle convection investigations. A typical setup of a laboratory model consists of a fish tank filled with a fluid at which a gradient of temperature is applied in order to generate the thermal instability. The fluid is characterized by a high Prandtl number (i.e. $Pr > 100$), which ensures the dominance of viscous over inertial effects (Davaille & Limare, 2015). The gradient of temperature and the thickness of the fluid layer are then properly adjusted in order to have a Rayleigh number within the range pertinent for mantle convection. The setup usually follows a Rayleigh-Bénard configuration with the fluid layer heated from below and/or cooled from above (e.g. Nataf & Richter, 1982). However, experiments with internal heating have also been performed (Limare *et al.*, 2015). The majority of studies which can be found in literature adopt Newtonian fluids, such as silicon oils, sugar syrups, glycerol (e.g. Giannandrea & Christensen, 1993; Namiki & Kurita, 1999; Davaille & Vatteville, 2005). Due to their strong strong temperature-dependent viscosity, sugar syrups have proved to be particularly suitable for the modeling of solid-state creep of mantle material (e.g. Nataf & Richter, 1982; Davaille & Jaupart, 1993; Androvandi *et al.*, 2011). In accordance with analytical studies (e.g. Jaupart & Parsons, 1985; Solomatov, 1995), different regimes of thermal convection are observed in a laboratory experiment, depending on the viscosity contrast between the upper and bottom boundary of the fluid layer: the 'whole layer regime', at low viscosity contrasts, where the entire fluid layer takes part in the convective motion; the 'sluggish lid regime', at intermediate viscosity contrasts, where convection occurs beneath a strong upper boundary layer which moves and deforms dissipating a significant amount of energy; the 'stagnant lid

regime', at high viscosity contrasts, where convection takes place under a stagnant lid which passively transports the heat brought from below by convection.

There is a fundamental element of mantle convection that laboratory experiments can not still capture: plate tectonics. In fact, although a strong plate on the surface can be obtained using a fluid with a strong temperature-dependent viscosity, the breakage of such plate (i.e. the lithosphere) and the following regime of 'plate tectonics convection' has not been observed yet. We know that to make plate tectonics works, weakening and shear localization are required. In numerical models weak zones within the lithosphere can be induced implementing pseudoplastic yielding, whereby plate boundaries develop instantaneously when the stress exceed locally a yield stress (Tackley, 2000; Grigné *et al.*, 2005). However, this operation requires the use of yield stress values that are smaller than what is known for mantle material (Kohlstedt *et al.*, 1995). In order to obtain plate boundaries adopting a consistent yield stress, a specific weakening mechanism inducing localized deformation is required and, in the last years, a number of them have been suggested, as for example lattice preferred orientation of olivine (Tommasi *et al.*, 2009), two-phase "self-lubricating" rheology (Bercovici, 2003) or shear heating (Kaus & Podladchikov, 2006; Crameri & Kaus, 2010). Concerning laboratory models, experiments run with aqueous colloidal dispersions of nanoparticles have lately shown several interesting features. Thanks to their particular rheology, these fluids can indeed generate a superficial lid which breaks in different 'plates', leading also to episodic subduction events. Exploring further this type of material seems thus a promising route to follow in order to generate self-consistent plate tectonics in the lab. Clarifying the dynamics underlying these systems might also lead to a better comprehension on the weakening mechanism generating plate boundaries on the Earth.

5.1 Drying of colloidal systems

What makes a colloidal dispersion particularly interesting is the type of rheology which characterized it. In a detailed study, Di Giuseppe *et al.* (2012) investigated the rheological transitions which a colloidal dispersion of silica nanoparticles (commercial name LudoxHS40) undergoes when subject to drying. Removing the water from the samples, thus increasing the solid volume fraction ϕ_p, the authors studied the rheological behavior of the colloid finding the regime diagram reported in figure 5.1a. As one immediately sees, the critical parameter controlling the rheological transitions is ϕ_p. In fact, depending on this parameter, the distance between the nanoparticles changes accordingly, influencing the particle-particle in-

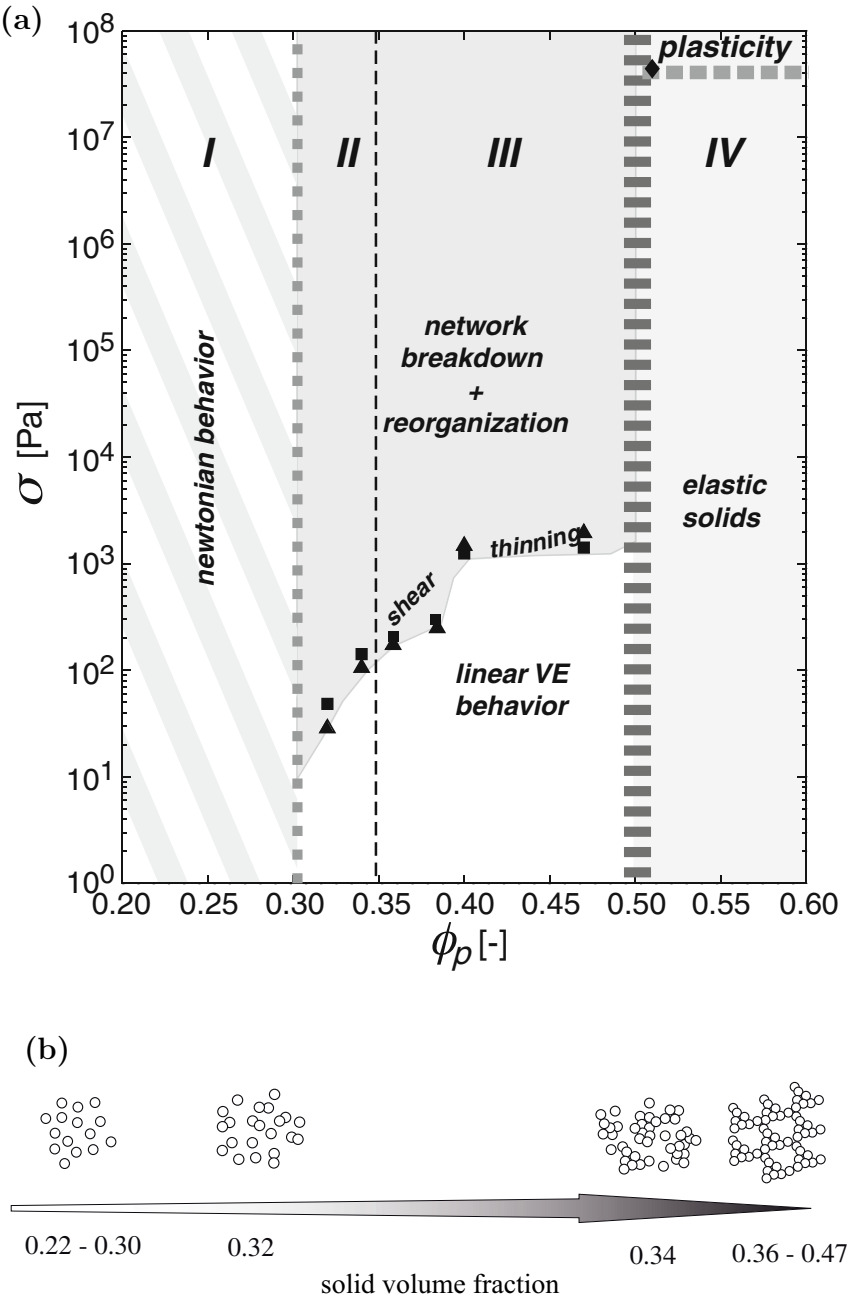

Figure 5.1. From Di Giuseppe *et al.* (2012): **(a)** regime diagram of aqueous monodisperse silica colloid (LudoxHS40) as a function of the solid volume fraction and the applied stress. The black filled symbols indicate results obtained by the authors. **(b)** sketch showing the possible spatial arrangement of the nanoparticles within the colloid as a function of the solid volume fraction.

teraction and, consequently, the energetically favorable configuration of the solid phase within the colloid (figure 5.1b). The latter is what ultimately controls the mechanical response of the colloid at a given applied stress. As illustrate in figure 5.1a the LudoxHS40 is characterized by four different rheological regimes. Regime I, for $\phi_p \leq 0.30$, where the colloid is constituted of a network of repelling isolated nanoparticles and it behaves as a Newtonian fluid, for any applied stress. Regime II, for $0.31 \leq \phi_p \leq 0.35$, where the nanoparticles start to aggregate, forming small clusters which induce solid-like properties, such as elasticity and a yield stress. Within this range of ϕ_p, the colloid behaves as a visco-elastic sol, exhibiting a shear-thinning rheology. Regime III, for $0.35 \leq \phi_p \leq 0.47$, where most of the particles have aggregated in stable structures which, however, can still deform and rearrange at high shear. At $\phi_p \approx 0.35$ is the sol-gel transition and the colloid is now a visco-elastic gel which maintains a shear-thinning rheology. Finally, regime IV, for $\phi_p \geq 0.51$, where the colloid has undergone the glass transition and behaves as an elastic-brittle solid. More details on the rheological characterization of such material can be found in Di Giuseppe *et al.* (2012).

Let us now consider a layer of Ludox in an experimental setup similar to the one shown in figure 5.3. The tank is dried from above, equivalent of cooling as both rock cooling and solution dessication are diffusion processes (§ 7 of Bacchin *et al.*, 2018), and heated uniformly from below. As shown in Davaille *et al.* (2017), in such configuration the laboratory model is characterized by an infinite Prandtl number and a high Rayleigh number, as appropriate for mantle convection modeling. A typical evolution of this type of convection experiment can be extrapolated by the curve of figure 5.2a, which shows how the evaporation rate V_E varies through time (§ 8 of Bacchin *et al.*, 2018). Looking at the trend of V_E, we can individuate five different stages of convection. First, there is a regime of vigorous convection 'CONV' where V_E remains roughly constant. Here, as the water evaporates at the free surface, ϕ_b locally increases generating a thin boundary layer at the top of the tank, whose thickness δ increases with the time. In case this boundary layer becomes gravitationally unstable and sinks, it is readily replaced by hot upwellings rising from below and the layer surface results continuously rejuvenated. The solutal Rayleigh number measuring locally the instability of the boundary layer is defined as

$$\mathrm{Ra}_{\mathrm{ch}} \equiv \frac{\Delta\rho g d^3}{\kappa_c \eta}, \tag{5.1}$$

where $\Delta\rho$ is the density contrast due to heterogeneities in the solid volume fraction ϕ_b, κ_c represents the chemical diffusivity and all the other parameters are defined

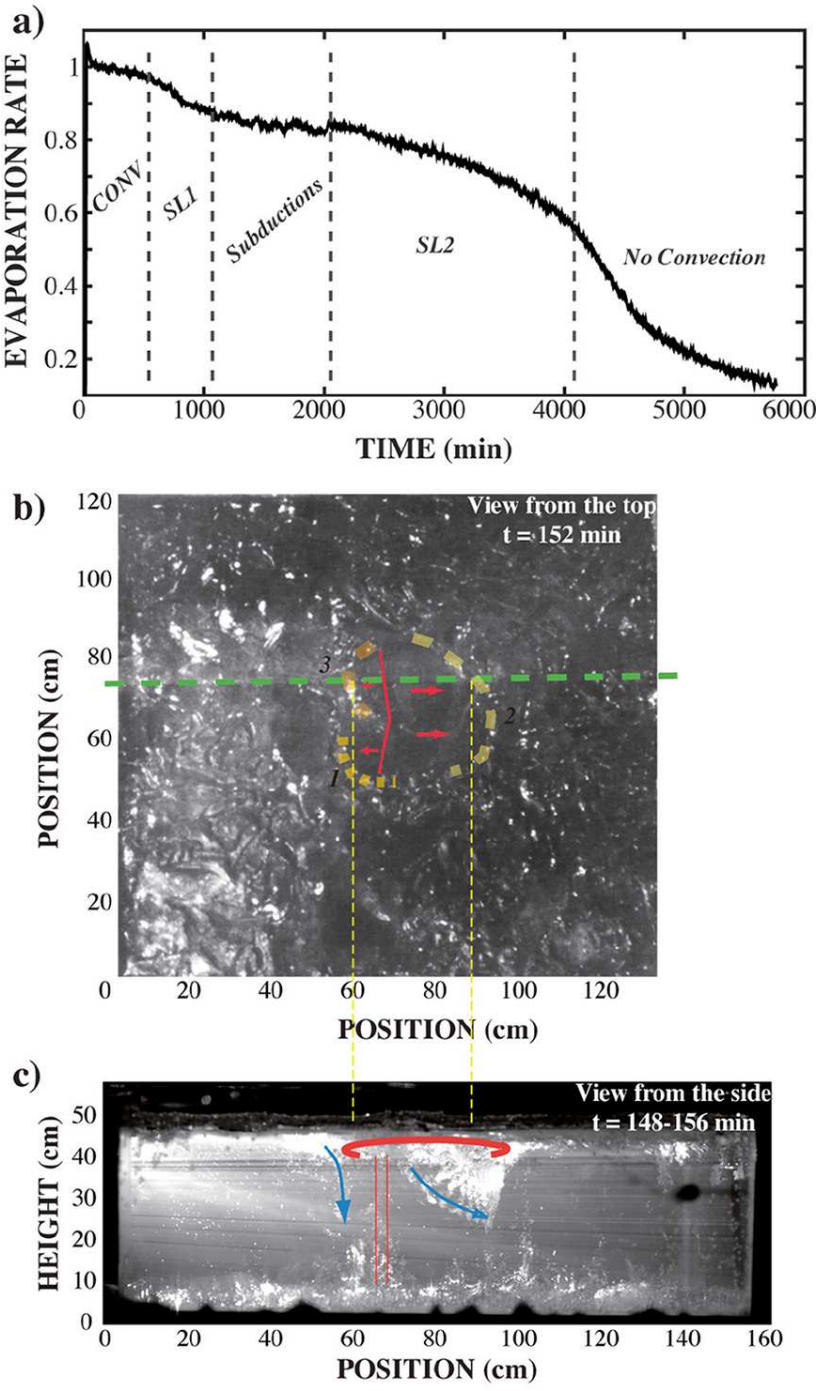

Figure 5.2. From Bacchin *et al.* (2018): **(a)** time-evolution of the evaporation rate during an experiment involving the drying of LudoxHS40. The evaporation rate is normalized by the corresponding evaporation rate of pure water in the the same setup. **(b)** top view of the tank showing the buckling deformation of the visco-elastic skin and the effect related to the impact of a hot upwelling. **(c)** side view of the tank, composed of superposed images, showing the subduction of the skin. For this experiment, presented in Davaille *et al.* (2017), the plume-induced subduction mechanism has been suggested.

as usual. In a typical experiment $\mathrm{Ra}_{\mathrm{ch}} \in [10^8 - 10^{11}]$ (Davaille *et al.*, 2017). We enter in the second regime 'SL1' when ϕ_b on the top reaches the critical value which marks the sol-gel transition ($\phi_b \approx 0.35$). Due to the formation of the superifical jelly skin, which acts as a barrier against the upward flow of the water, V_E decreases significantly. At the same time, convection continues to take places below the skin and a Stagnant Lid regime develops. Now, as the water continues to flow through the skin, it generates pressure gradients and in-plane stresses in the skin, which, in turn, starts to visco-elastically buckle. This deformation is shown in the top view of the tank reported in figure 5.2b. The buckling instability grows in amplitude with time due to the spatial confinement of the skin and the increasing of stresses related to the continuous evaporation of water. At one point, because of the high strain and stress at which it is subjected, the skin leaves the elastic regime and it starts to deform plastically until it eventually breaks. Then, due to its higher density with respect to the underlying fluid, it sinks toward the bottom. This is the third regime 'Subduction' where spontaneous, one-sided subduction events appear, showing also the characteristic "trench roll back" feature of natural subduction zones, as highlighted in figure 5.2c. Furthermore, as new fluid reaches the surface and dries, new skin is continuously formed and the cycle of buckling deformation and subduction is repeated. Even if we cannot speak yet of true and continuous plate tectonics, this 'Subduction' regime presents striking similarities with what is observed on Earth. Here, the combination between a strong buckling instability and the particular rheology of the skin (i.e. the lithosphere), seems to lead to the rupture and the consequent initiation of subduction. Another mechanism triggering subduction, involving the impact of a rising plume on the lower part of the skin, has also been proposed (Davaille *et al.*, 2017). This might be valid, in particular, when bottom heating is significant. In any case, as the system continues to dry, the system reaches a critical point where the top layer is so stiff and thick that cannot be broken anymore. It starts the 'SL2' regime where convection is in a second Stagnant Lid mode and subduction stops. V_E smoothly decreases through time, while the skin continuously thickens. When it approaches the bottom of the tank, V_E abruptly decreases and the convection finally stops. This is the 'No Convection' regime.

5.2 Preliminary results

Aiming to better understand the dynamics underlying the drying of a colloidal dispersion, in the last part of the thesis we run a laboratory experiment, similar to the one described in the previous section. The setup of the experiment is

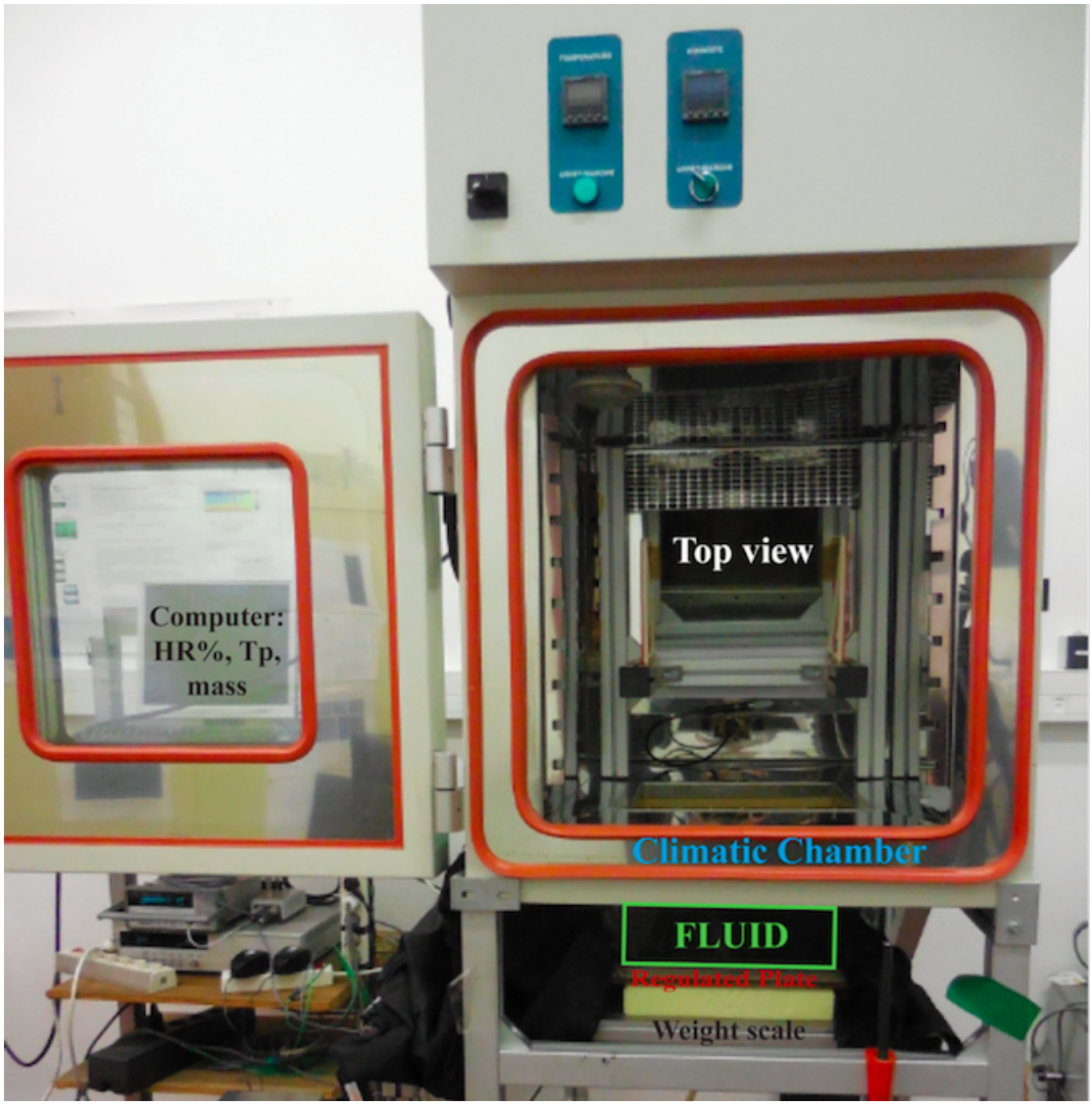

Figure 5.3. Experimental setup of a drying convection experiment. The colloid layer into the tank (green) is dried from above by an air stream whose temperature (T) and humidity (Rh) are controlled by a climatic chamber. For our experiment is $T = 25°C$ and Rh = 30%. The tank is placed on a metal plate that can be heated if needed. Further below there is a weight scale that records the mass lost during the experiment because of the evaporation of water.

illustrated in figure 5.3. For our study, we adopted a LudoxTM50 silica colloidal dispersion from Sigma-Aldrich. We used a $30 \times 30 \times 5$ cm tank, placed in a climatic chamber, where the temperature and the humidity were kept at the constant values of $T = 25°C$ and $Rh = 30\%$, respectively. The bottom boundary of the tank was maintained at the room temperature, without providing any heating. The tank was on a scale to record the evolution of mass and evaporation rate. The experiment lasted one day.

5.2.1 Observations

In figure 5.4b is reported the time-evolution of the evaporation rate V_E recorded during our experiment. The curve is characterized by 3 different zones: Zone 1, $50 \leq t \leq 200$, where V_E rapidly decreases; Zone 2, $200 \leq t \leq 1600$, where V_E remains around the value $V_E = 0.008$ g/s (blue line), showing a slow (but constant) decreasing starting from $t \geq 540$; Zone 3, $t \geq 1600$, where V_E begins to decrease rapidly again. In analogy with what has been shown in figure 5.2a, Zone 1 seems to correspond to the 'SL1' regime of convection. In fact, in our experiment, the 'CONV' regime seems to be missing and we assist directly to a rapid formation on the top of a gel skin with a consequent decreasing of the evaporation rate. In this regime, as the gel continues to form, we record a first subduction/resurfacing event which starts at $t = 80$ min (figure 5.5a) and evolves followed by news subduction/resurfacing events (figure 5.5b). This leads to a complete rejuvenation of the superficial gel skin. Next, as V_E stabilizes around the constant value of $V_E = 0.008$ g/s, we enter in the Zone 2. This is the 'Subduction' regime of figure 5.2a. Here cycles of gel breakage, subduction and gel regeneration repeat continuously and in a local scale instead of leading to complete resurfacing. Unfortunately, we could not get photos of the tank during this stage of convection. However, the side view of the tank given in figure 5.6, taken at the end of the experiment, clearly shows a "rich" subduction history. In particular, we can notice the subduction of two "fat slabs", as highlighted by the red circle at the bottom left corner of figure 5.6. Within the Zone 2, we can see that at one point ($t = 540$ min), glass begins to form on the surface of the tank (figure 5.5c). This event roughly corresponds with the point where V_E starts slowly to decrease (third red dot figure 5.4c). Finally, as the superficial layer of glass spreads on the entire surface (figure 5.5d) and thickens, subduction/surface regeneration events are more and more rare and we approach the beginning of the 'SL2', where convection takes place below a stiff "glass lid".

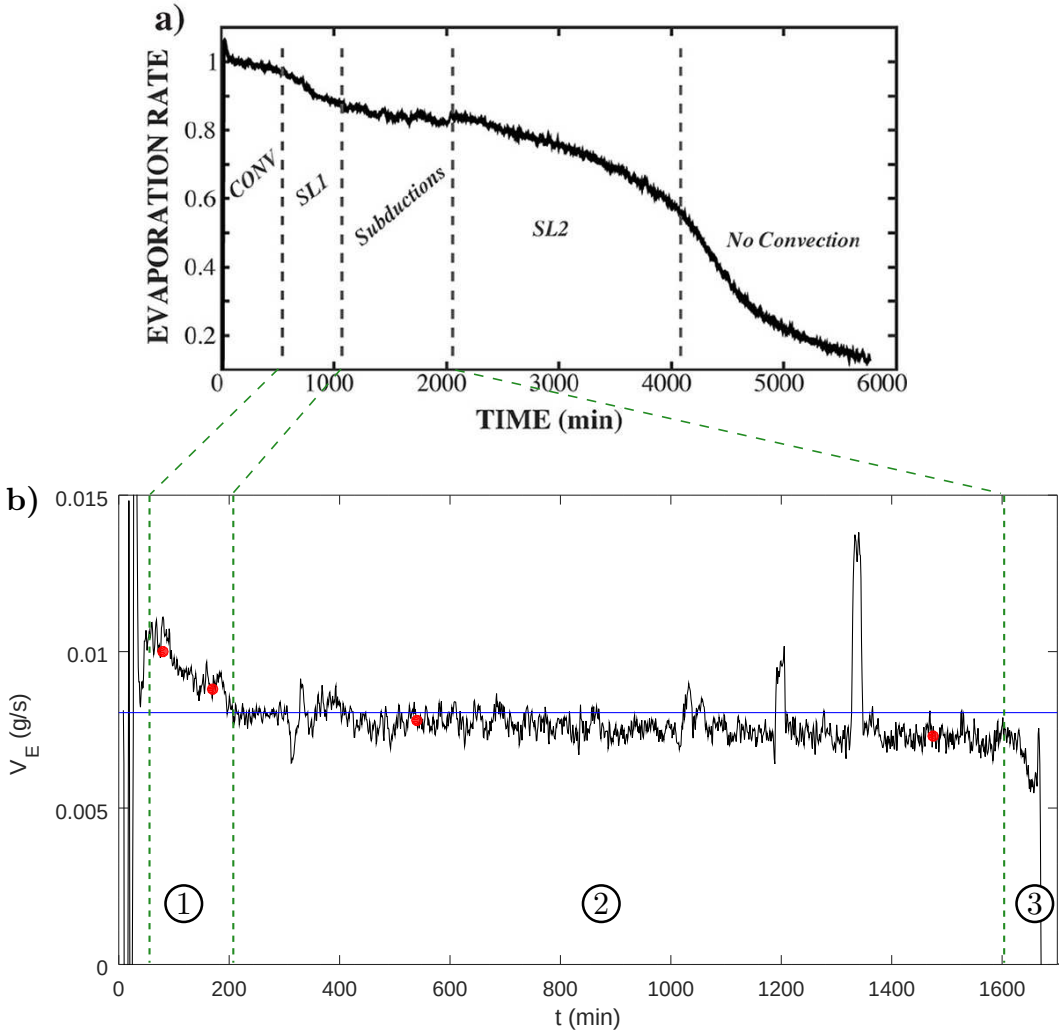

Figure 5.4. **(a)** $V_E - t$ curve shown in figure 5.2a. **(b)** $V_E - t$ curve of our experiment. The green dashed lines compare the three regimes of convection of our experiment with the ones identified in **(a)**. The red dots correspond to the four top views of the tank reported in figure 5.5. The sharp peaks at $t \approx 1200$ min $t \approx 1350$ min are related to external perturbations.

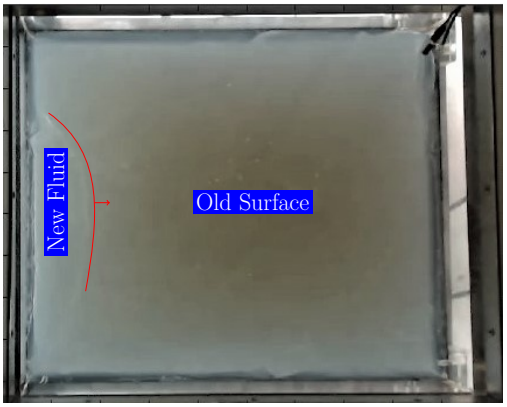

(a) Zone 1: The gel breaks on the surface and a first subduction/resurfacing event is recorded. The red line shows the wrinkle which moves as indicated by the red arrow. New fluid rises from the left side of the wrinkle.

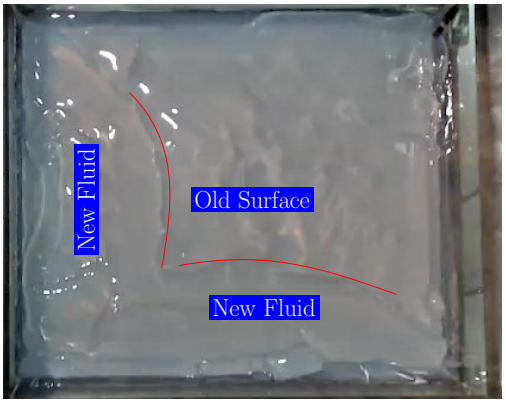

(b) Zone 1: Here we can appreciate the evolution of the subduction/resurfacing event shown in figure 5.5a, as well as the starting of new subduction/resurfacing events (red line at the bottom).

(c) Zone 2: the glass transition starts to take place and white, solid material appears (red circles).

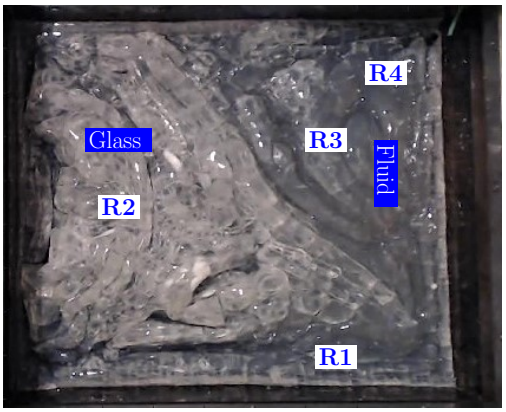

(d) Zone 3: The glass phase covers a large part of the surface. Some fluid-like material is, however, still presents. R1-R2-R3-R4 indicate the regions where the samples listed in table 5.1 have been taken.

Figure 5.5. Top view of the tank during the experiment, showing the time evolution of the skin. The photos have been taken at $t = 80$ min (a), $t = 170$ min (b), $t = 540$ min (c), $t = 1475$ min (d), which correspond to the four red dots of figure 5.4b.

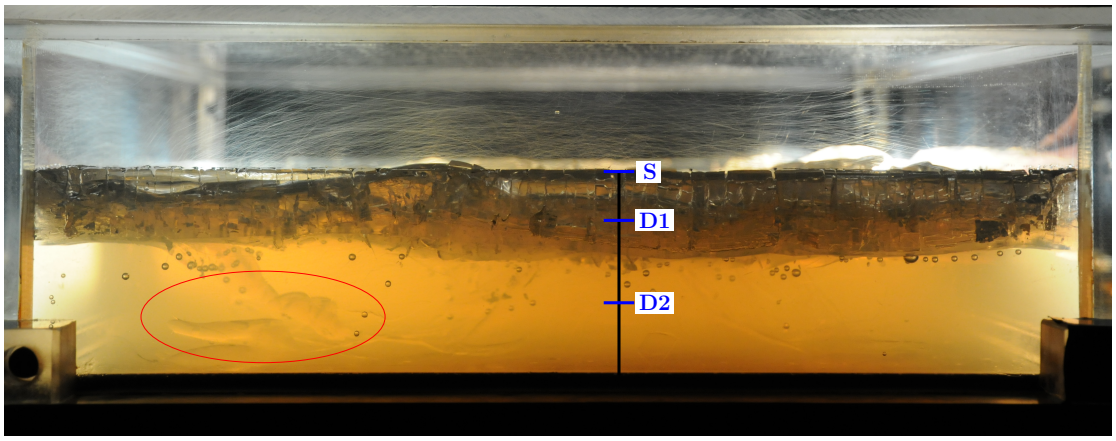

Figure 5.6. A side view of the tank taken at the end of the experiment. The image shows that, during the experiment, a significant amount of superifical material (translucent) has sunk in the underlying fluid layer. In the bottom left corner of the picture, we can notice two "fat slabs" lying on the bottom of the tank. S-D1-D2 represents the depths at which the samples listed in table 5.1 have been taken.

5.2.2 In situ measurements

As it immediately appears from the comparison of the $V_E - t$ curves of figures 5.4a and 5.4b, using two different colloids (LudoxHS40 for what concerns figure 5.4a and LudoxTM50 for what concerns figure 5.4b) for the same type of experiment, it can lead to different results. This follows from the fact that changing the properties of the dispersed phase in the colloid (i.e. the silica nanoparticles), the physical-chemical phenomena which control molecular aggregation vary accordingly and the response of the colloidal system observed at the marcoscopic scale results different. For the present case, what changes between the two types of colloid is the hydrodynamic radius r_{H} which, measured by means of dynamic light scattering in the initial semi-dilute suspension ($\phi_b \leq 0.22$), results $r_{\mathrm{H}} \approx 15$ nm for the LudoxHS40 and $r_{\mathrm{H}} \approx 30$ nm for the LudoxTM50. As we can see in figure 5.7, a different value of r_{H} influences tremendously the correlation between the rheology of the colloid and the particle volume fraction ϕ_b.

In order to shed light on the composition and the nano-scale structure of the LudoxTM50 adopted in our study, we analyzed several samples taken at the end of the experiment. For each sample, which generally was around 15.0 mg, we performed two type of measurements: i) the thermal gravimetric analysis (TGA), where the mass of the sample is measured over time as the temperature changes; ii) the differential scanning calorimetry (DSC), where the apparatus measures the amount of heat absorbed/released by the sample as a function of temperature. The TGA has been carried out in a dynamic nitrogen atmosphere of 40 mL/min, varying the temperature with a rate of 5°C/min from room temperature to T =

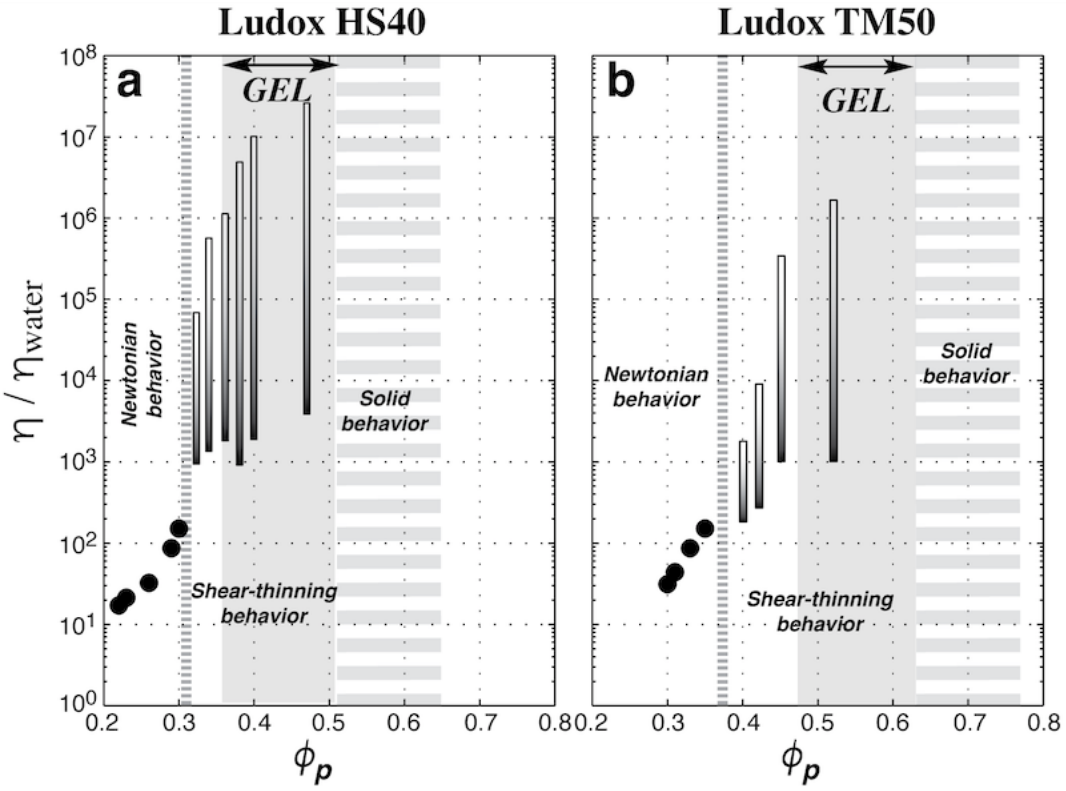

Figure 5.7. Phase diagrams for the LudoxHS40 (**a**) and the LudoxTM50 (**b**). The figures report the relative viscosity of the colloid (normalized by the viscosity of the water) as a function of the particle volume fraction. The GEL state is defined by $G' > G''$, where G' is the storage modulus, characterizing the stored elastic energy and G'' is the loss modulus, characterizing the energy dissipated by heat (Di Giuseppe *et al.*, 2012). The elongated bars show the viscosity variations for strain-rates between 10^{-1}(white) and 10^{3} (black) 1/s. The sol-gel transition is at ϕ_b = 0.35 for the LudoxHS40 and at ϕ_b = 0.48 for the LudoxTM50. The gel-glass transition is at ϕ_b = 0.51 for the LudoxHS40 and at ϕ_b = 0.62 for the LudoxTM50. Measurements of Erika Di Giuseppe.

Table 5.1. Properties of the samples analyzed with the TGA and the DSC techniques. The position of the sample in the tank is specified by the region (figure 5.5d) and the depth (figure 5.6). The two samples 'Sl1' and 'Sl2' are the two "fat slabs" shown in figure 5.6. Samples 6 and 7 have been taken at slightly lower levels than the depth $D1$. The temperature in brackets in the column referring to ΔT_m indicates the melting point of free water. The sol-gel transition is at $\phi_b = 0.48$. The gel-glass transition at $\phi_b = 0.62$ (see figure 5.7).

Samples	Region	Depth	ϕ_b	Phase	ΔT_m [°C]	d [nm]
#1	R1	S	0.39	Sol	7.49 (0.56)	12.7
#2	R1	D1	0.59	Gel	7.87	12.1
#3	R1	D2	0.39	Sol	6.93 (0.28)	13.7
#4	R2	S	0.65	Glass	6.74	14.1
#5	R2	D1	0.64	Glass	7.21	13.2
#6	R2	D1−	0.64	Glass	7.59	12.5
#7	R2	D1−−	0.68	Glass	7.31	13.0
#8	R2	D2	0.32	Sol	6.93 (0.56)	13.7
#9	R3	S	0.53	Gel	7.02	13.5
#10	R3	D2	0.34	Sol	7.40 (0.47)	12.8
#11	R4	'Sl1'	0.57	Gel	7.31	13.0
#12	R4	'Sl2'	0.60	Gel	7.64	12.4

250°C and of 10°C/min beyond. The DSC has been carried out in a dynamic nitrogen atmosphere of 25 mL/min, decreasing the temperature with a rate of −5°C/min from room temperature to −60°C and then increasing it with a rate of 2°C/min up to 20°C. We analyzed 12 samples taken at different depth and in different regions of the tank, as indicated in table 5.1. Two of these samples were part of the "fat slabs" shown in figure 5.6. This analysis has been done at the Laboratoire Léon Brillouin of the CEA Saclay thanks to the precious help of Christiane ALBA-SIMIONESCO and Oriana OSTA.

An example of the output obtained from the TGA is shown in figure 5.8. Since at the end of this type of measurement only the silica solid phase of the sample is left, we exploited the TGA to extrapolate the silica weight fraction χ_s and the corresponding solid volume fraction ϕ_b, according to

$$\phi_b = \frac{\chi_s}{\chi_s + (1 - \chi_s) * \frac{\rho_{\mathrm{Si}}}{\rho_{\mathrm{W}}}}, \tag{5.2}$$

where $\rho_{\mathrm{Si}} = 2.36$ g/cm^3 is the density of silicon and $\rho_{\mathrm{W}} = 1.00$ g/cm^3 is the density of water. The results on the solid volume fraction are summarized in the 4th column of table 5.1. The data show that at the end of the drying experiment, the colloid presents all the three phases: sol, gel and glass. Region 1 of the tank

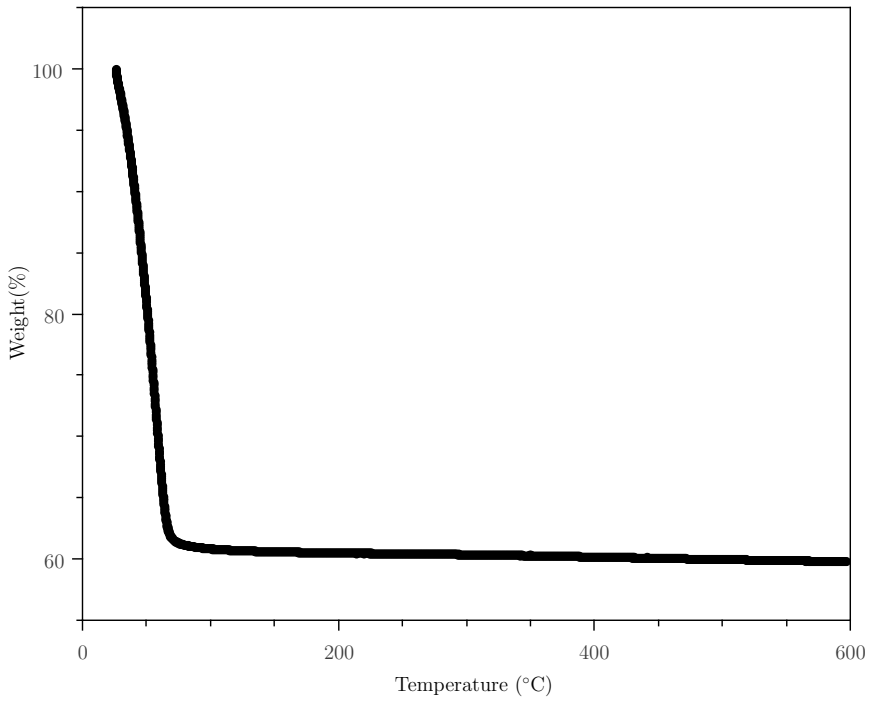

Figure 5.8. TGA measurement reporting the variation of the mass of the sample (in percentage) as a function of the temperature.

(see figure 5.5d) presents sol on the surface and a gel layer immediately below. At the depth of D2 (see figure 5.6), the sol phase appears again. This composition, clearly highlights that in this region there is still fluid from below rising toward the surface. Region 2 is composed of a thick layer of glass which covers the underlying sol. Region 3 is instead characterized by a gel layer on the surface which underlies the sol-phase. The samples referring to the "fat slabs" have a gel composition, thus showing that they were on the top of the tank and that they subducted during the experiment.

Concerning the DSC, an example of the outputs is reported in figure 5.9. Measuring the heat flow as temperature varies, this technique can identify the temperature at which physical transitions occur, as they are identified by the absorption/release of latent heat, which is much higher than the sensible heat. The DSC is useful to obtain an information regarding the average size of the pores of the solid network of silica nanoparticles which forms in the colloid during the drying. Indeed, the water entrapped within such a structure undergoes a melting temperature depression ΔT_m which is related to the pore diameter d through the Gibbs-Thomson equation (Alba-Simionesco *et al.*, 2006):

$$\Delta T_m = T_{m,bulk} - T_{m,pore} = 2\frac{(\gamma_{SI} - \gamma_{SL})\nu}{d\lambda_{m,bulk}}, \tag{5.3}$$

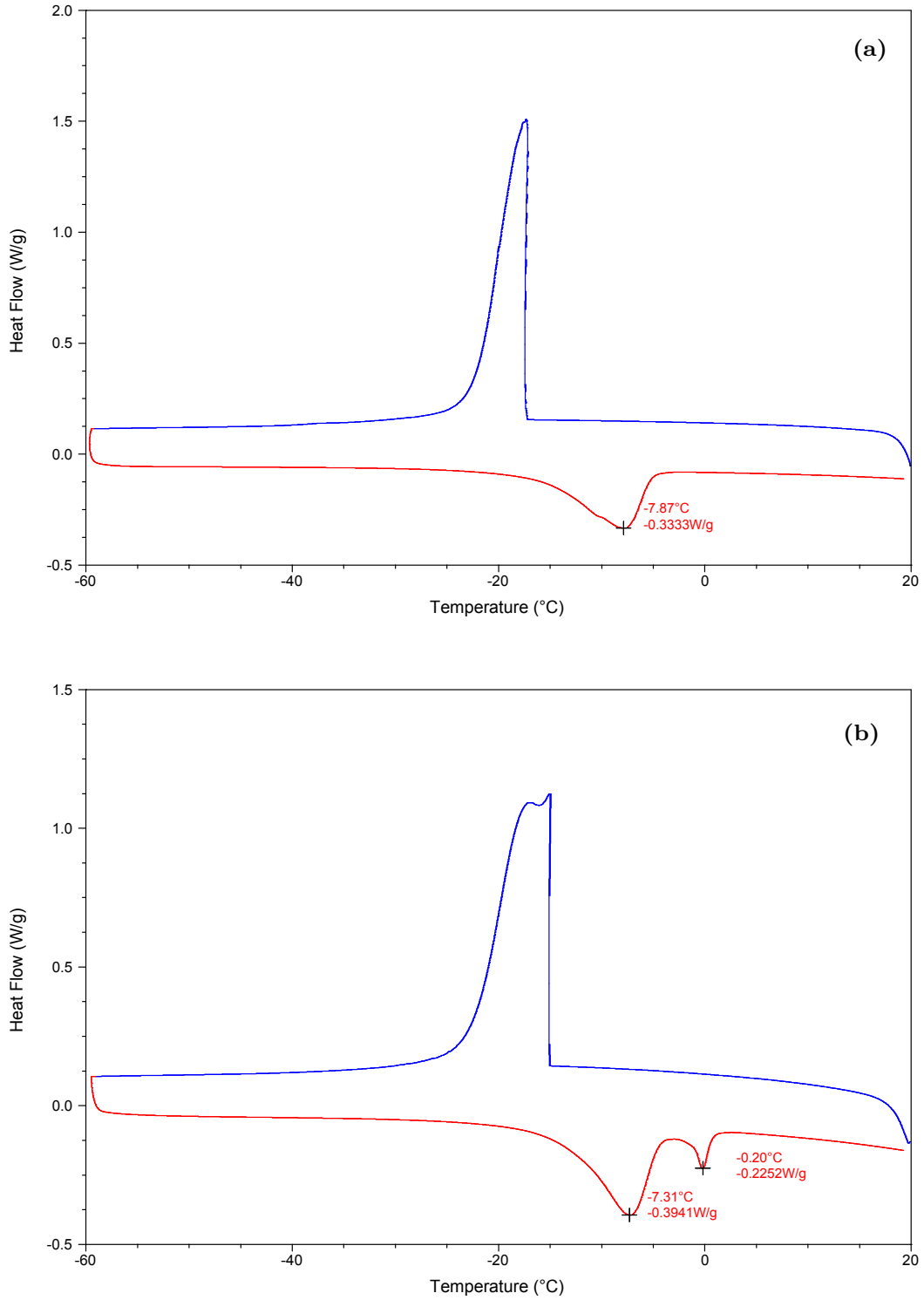

Figure 5.9. DSC measurement reporting the amount of heat released (blue curve) or absorbed (red curve) by the sample as a function of the temperature. The peaks correspond to phase transitions of the water contained in the sample: freezing (blue curve), melting (red curve). **(a)** refers to a glass-like or gel-like samples, while **(b)** refers to a sol-like sample. The latter shows two melting points of the water, as this is both in a confined-state and in a bulk-state within such type of sample (see text for details).

where $T_{m,bulk}$ and $T_{m,pore}$ are the melting temperatures of bulk water crystals and of confined water nanocrystals, respectively, γ_{SI} and γ_{SL} are the silica/ice and silica/liquid water surface tensions, ν is the molar volume of the liquid water and $\lambda_{m,bulk}$ is the bulk latent heat of melting. Due to the dependence of the quantities γ_{SI}, γ_{SL} and ν on the pore diameter d, eq. (5.3) is usually adopted in an experimental-fitting form. Relevant to our case study, where water nanocrystals melt in a solid structure composed of silica nanoparticles, is the fitting equation proposed by Lu *et al.* (2013):

$$\Delta T_m = \frac{95}{d}, \tag{5.4}$$

which easily correlates d with the ΔT_m obtained from the DSC measurements.

For all the samples (sol-like, gel-like and glass-like), the DSC showed a melting temperature depression of the confined water between $6.74°C$ and $7.87°C$ (6th column of table 5.1), corresponding to an average pore diameter ranging from 12 to 14 nm (7th column of table 5.1). The data did not show any correlations between d and the solid volume fraction of the samples ϕ_b. However, as highlighted in figure 5.9b, for sol-like samples the DSC additionally recorded the melting temperature of water crystals not affected by any confinement effect ($T_m = 0°C$). This means that in this phase we have both confined and bulk (or free) water.

The pore diameter d resulted half the nanoparticle hydrodynamic radius ($r_H \approx 30$ nm). This suggests that all the three phases are characterized by dense packed structures of nanoparticles. In the glass and gel phases these structures probably build a semi-ordered, continuous network of nanoparticles. In the sol phase, due to the presence of free water, they assume more likely the form of dense clusters that keep a certain distance between them.

Ongoing work involves the characterization of the colloid at the different stages of the drying experiment. This will help to unmask the correlation between the physical-chemical phenomena controlling the nanoparticles aggregation and the macroscopic response of the colloidal system.

Conclusions

This thesis was devoted to the study of the phenomenon of subduction. For this purpose, we developed a 2-D free subducion model, based on the Boundary Element Method, able to mimic the interaction between a Subducting Plate (SP) and an Overriding Plate (OP) across a Subduction Interface (SI) with a tunable strength. Then, we systematically interpreted the numerical solutions of the model exploiting concepts of thin viscous-sheet theory. This helped us to determine quantitative scaling laws expressing relations among key dimensionless parameters of the system.

We examined subduction from two main points of view: first, we investigated the phenomenon in a 'local' context, aiming to better understand the mechanics underlying it; then, we moved to a 'global' context, exploring the effect of subduction zones in the frame of large-scale mantle convection.

Exploring subduction locally, we focused our investigation on the SP kinematics and the OP deformation, paying particular attention at the influence of the SI strength on both these aspects of subduction. Regarding the SP kinematics, we first found that the convergence speed of the sinking slab (V_{Conv}) is mainly controlled by three parameters: the subduction angle θ_0, the flexural stiffness St of the SP and the strength γ of the SI. For instance, V_{Conv} increases as we move from shallow to steep subduction (increasing of θ_0) or if either the stiffness of the SP or the strength of the SI decreases. Interestingly, such speed did not show any dependency neither on the length of the SP (L_{SP}) nor on that of the OP (L_{OP}). Next, we analyzed the horizontal plate speed (U_{SP}) of the flat portion of the SP and, considering first our subduction model in the SP ONLY configuration (i.e. without the OP), we found that U_{SP} obeys the scaling law $U_{\mathrm{SP}}/V_{\mathrm{Stokes}} = \alpha(\mathrm{St}) + \beta(\mathrm{St}) \log(L_{\mathrm{SP}}/\ell)$, where α and β are logarithmic functions of St. The main result here is the perfect logarithmic dependence of $U_{\mathrm{SP}}/V_{\mathrm{Stokes}}$ on the geometrical ratio L_{SP}/ℓ, a result which we found systematically also in the SP+OP configuration and for whatever model setups we investigated. This very weak correlation between plate speed and plate length for plates attached to subducting slabs seems to be in agreement with natural observations. Turning to

the OP deformation, we detected a characteristic pattern of deformation that repeated similarly for the majority of cases we explored. Close to the trench, the OP is always under strong compression due to the opposing actions of the horizontal resultant of the lubrication force within the SI and the shear force below the forearc region of the OP. This latter force, generated by the mantle return flow, results as the sole driving force triggering the OP motion. Further from the trench there is a second zone of deformation dominated by the bending of the OP. This zone disappears only if one considers steep subduction angles and, especially, long subducting slabs for which compression continues to dominate. Finally, a third mode of deformation, characterized by significant extension in the backarc region of the OP, arises when the OP is positively buoyant. We explained such result by means of simple analytical thin-layer models. In conclusion of this first part, we adopted our BEM model to infer the long-term strength of the subduction interface in the central Aleutian subduction zone. For a realistic range of values of the viscosity ratio between the SP and the underlying mantle, we found $\eta_{\mathrm{SI}} = 0.96 - 1.72 \times 10^{20}$ Pa s for a corresponding range of mantle viscosities $\eta_0 = 3.92 - 6.95 \times 10^{20}$ Pa s.

Next, we turned to the analysis of the energetics of subduction. In particular, we quantified the amount of viscous energy that is dissipated in a subduction zone, discussing then the effects that this might have on large-scale mantle convection. Considering first the SP ONLY configuration, by means of a scaling analysis of the instantaneous rates of viscous dissipation associated with the deformation of the SP and of the underlying mantle, we found that the ratio R of the energy dissipated in the upper boundary layer to the total energy dissipation obeys the scaling law $R \sim \mathrm{St}/[\mathrm{St} + \mathrm{F}(\theta)]$, where, again, a crucial parameter is the stiffness St of the SP and $\mathrm{F}(\theta)$ represents a function that accounts for the effect of the subduction angle θ. Adding the OP to the system, we found that R also depends on the SI strength γ, which takes into account the dissipation of energy related to the deformation of the SI, particularly relevant for weak SPs. Then, we explored the temporal evolution of the dissipation ratio $R(t)$ for a SP/mante viscosity ratio $\lambda_1 = 250$ and $\lambda_1 = 2500$. The interesting result here is that $R(t)$ remains always below the value 0.5, thus showing that the energy dissipation during free subduction is never dominated by the plate bending and interface shearing contributions. In light of these results, we finally moved on the study of large-scale mantle convection in presence of strong subduction zones. More specifically, we investigated the influence of the energy dissipation at subduction zones on the exponent β of the scaling law $\mathrm{Nu} \sim \mathrm{Ra_m}^{\beta}$, where $\beta = 1/3$ in the classical derivation concerning an isoviscous fluid layer. With the help of a parameterized model of mantle convection, we first showed that a crucial parameter is the time t employed by the

lithosphere to travel from the ridge to the trench of the subudction zone. Indeed, we distinguished between two cases depending on whether or not the travel time achieves the value $t \approx 80$ Myr, which is commonly indicated as the age at which seafloor flattening is observed to occur. If $t \leq 80$ Myr, the thickness h_{SP} of the SP when it enters the subduction zone is described by the classical half-space cooling model and depends on the mantle Rayleigh number $\mathrm{Ra_m}$. In such case, for a reasonable range of energy dissipation at the subduction zone, associated with both the SP bending and the SI shearing, we found $\beta = 1/3$, as for an isoviscous mantle. Differently, when $t \gg 80$ Myr and h_{SP} is not anymore a function of $\mathrm{Ra_m}$, we found that β varies according to $\beta = 0.5/(1 + C_{\mathrm{R}})$, where $C_{\mathrm{R}} \equiv R/(1 - R)$ is the ratio of the boundary-layer dissipation rate to that within the surrounding mantle. What drammaticaly influences the result here is the length scale that one adopts to characterize the bending of the SP. We demonstrated that if the minimum radius of curvature of the plate is used (R_{min}) the bending dissipation of the SP is strongly overestimated leading thus to $\beta \to 0$. By contrast, using the correct length scale, the 'bending length' ℓ_b, we found that $\beta \in [0.25 - 0.34]$, depending on the depth of the convecting layer which one considers. This suggests that strong subduction zones do not dominate the viscous dissipation associated with mantle convection and that they lead to relatively small departures from the classical $\mathrm{Nu} \sim \mathrm{Ra_m}^{1/3}$ heat transfer law. In light of such results, we conclude that viscous dissipation at subduction zones can not be the cause underlying the failure of parameterized cooling models in predicting the present-day Urey ratio for the Earth. We need to look somewehere else in order to reconcile the arguments coming from geodynamical and geochemical investigations.

In the last part of the thesis, aiming to validate our last results concerning large-scale mantle convection, we investigated a convection experiment based on the drying of a colloidal system. Preliminary results seem to confirm some results that have lately been published. This type of experiment seem to effectively captures the essence of Earth's mantle convection and the particular features which characterized it, as, for instance, the breakage of the strong upper boundary layer (i.e. the lithosphere) and the subsequent phenomenon of subduction. Investigate further the link between nano-scale phenomena, colloid rheology transitions and macroscopic response of the system seems a promising route to explore in order to have a clearer picture of how mantle convection works and to unmask the weakening mechanism leading to subduction initiation on Earth.

Appendix A

Stretching rate of a thin-viscous sheet below a lubrication layer bounded by a free-slip surface

Our goal is to show that a positively buoyant OP beneath a thin lubrication layer tends to deform in extension. For this purpose, we consider an isolated OP, and assume that the shear stress acting on its upper surface is much larger than that on its lower surface. To simplify the notation, we set $x_1 \to s$, $x_2 \to z$, and $u_1 \to u$. The global force balance in the horizontal (s-) direction is (Ribe, 2001)

$$(4\eta_2 h_{\mathrm{OP}} U')' + \sigma_{sz}|_{z=-d_1} = 0, \tag{A.1}$$

where primes denote $\mathrm{d}/\mathrm{d}s$, $\sigma_{sz}|_{x_2=-d_1}$ is the shear stress acting on the upper surface of the OP, and the quantity in parentheses is the integral of the fibre stress σ_{ss} across the OP. To determine σ_{sz} in the lubrication layer, we start from the s-component of the momentum equation in the lubrication limit, which is

$$p' = \eta_0 \frac{\partial^2 u}{\partial z^2}. \tag{A.2}$$

Since the OP is much more viscous than the lubrication layer, the effective boundary condition on the horizontal velocity is $u|_{z=-d_1} = 0$. Integrating eq. (A.2) subject to that condition and the free-slip surface condition $\partial u/\partial z|_{z=0} = 0$, we obtain

$$\sigma_{sz}(s, -d_1) \approx \eta_0 \frac{\partial u}{\partial z}(s, -d_1) = -p' \frac{d_1}{\eta_0}. \tag{A.3}$$

Eq. (A.1) then becomes

$$4\eta_2 h_{\mathrm{OP}} U'' - p' d_1 = 0. \tag{A.4}$$

Now integrate eq. (A.4) once subject to the condition that both U' and p vanish at $s = 0$, which yields

$$U' = \frac{d_1}{4\eta_2 h_{\mathrm{OP}}} p. \tag{A.5}$$

Now the pressure in the OP is given by the solution of Ribe (2010), viz.,

$$\frac{p}{h_{\mathrm{OP}} g \Delta\rho_2} = -1 + \exp\left(-s/\ell_0\right) - \frac{2}{\sqrt{3}} \exp\left(-s/2\ell_0\right) \sin\frac{\sqrt{3}s}{2\ell_0}, \tag{A.6}$$

where

$$\ell_0 = \left(\frac{\lambda_2 h_{\mathrm{OP}}^3 d_1^3}{9}\right)^{1/6}. \tag{A.7}$$

Combining (A.5) and (A.6), we obtain

$$\frac{4\eta_2}{d_1 g \Delta\rho_2} U' = -1 + \exp\left(-s/\ell_0\right) - \frac{2}{\sqrt{3}} \exp\left(-s/2\ell_0\right) \sin\frac{\sqrt{3}s}{2\ell_0}. \tag{A.8}$$

Eq. (A.8) describes the stretching rate of an OP that is sufficiently long that the two ends do not influence each other. Far from the ends of the OP ($s \gg \ell_0$), the stretching rate is

$$U' = -\frac{d_1 g \Delta\rho_2}{4\eta_2}, \tag{A.9}$$

which shows that the OP deforms by extension ($U' > 0$) if it is positively buoyant ($\Delta\rho_2 < 0$).

We now verify our assumption that the shear stress on the lower surface of the OP ($= F_s^-$) is negligible compared to that on the upper surface ($= F_s^+$). Consider the portion of the OP of length $\sim \ell_0$ adjoining the end $s = 0$, where the shear stress on the bottom surface is largest. From the above solution, we already know that

$$F_s^+ \sim p' d_1 \sim h_{\mathrm{OP}} g \Delta\rho_2 / \ell_0, \tag{A.10}$$

where the scale for p' comes from eq. (A.6). Now, the shear stress on the base of the OP is

$$F_s^- \sim \eta_2 W / \ell_0 \sim d_1^{3/2} g \Delta\rho_2 / \sqrt{\lambda_2 h_{\mathrm{OP}}}, \tag{A.11}$$

where the scale for W comes from eq. (B6) of Ribe (2010). Taking the ratio of the two stresses and using eq. (A.7), we obtain

$$\frac{F_s^-}{F_s^+} \sim \lambda_2^{-1/3} \left(\frac{d_1}{h_{\mathrm{OP}}} \right). \tag{A.12}$$

For small values of d_1/h_{OP} and large viscosity contrasts λ_2 (as in our study), $F_s^-/F_s^+ \ll 1$.

The analysis above is for an isolated OP, and succeeds in showing that a positively buoyant OP should deform in extension. However, in our BEM model the OP is not isolated, but is strongly influenced by the shear stress induced on its base by the sinking of the neighboring slab. This additional shear stress is much larger than F_s^+, and so our assumption $F_s^- \ll F_s^+$ breaks down. The results of the derivation above should therefore be interpreted as indicative rather than as an accurate reflection of the BEM model.

Appendix B

Spreading gravity current below a free-slip surface

Inspired by the model of Holt *et al.* (2015), we consider a buoyant layer of fluid (the OP) bounded above by a free-slip surface. The OP has thickness h_{OP}, density ρ_{OP} and viscosity η_{OP}, while the underlying fluid has density $\rho_{\mathrm{M}} = \rho_{\mathrm{OP}} - \Delta\rho$ and viscosity $\eta_{\mathrm{M}} \ll \eta_{\mathrm{OP}}$. To lowest order, the horizontal velocity is constant across the layer (plug flow). The horizontal force balance within the layer is (Canright & Morris, 1993)

$$\frac{\partial}{\partial s}\left[h_{\mathrm{OP}}^2 + 8h_{\mathrm{OP}}\left(\frac{\eta_{\mathrm{OP}}}{g\Delta\rho}\right)U'\right] = 0, \tag{B.1}$$

where $U' = \partial U/\partial s$. Integrating (B.1) once, we obtain

$$h_{\mathrm{OP}}^2 + 8h_{\mathrm{OP}}\left(\frac{\eta_{\mathrm{OP}}}{g\Delta\rho}\right)U' = F, \tag{B.2}$$

where F is a constant. At the ends of the OP, $U' = h_{\mathrm{OP}} = 0$, which requires $F = 0$. Therefore

$$U' = -\frac{h_{\mathrm{OP}} g\Delta\rho}{8\eta_{\mathrm{OP}}}. \tag{B.3}$$

Now from thin viscous-sheet theory, the horizontal normal stress in the OP is $\sigma_{ss} = 4\eta_{\mathrm{OP}}U'$, or

$$\sigma_{ss} = -\frac{h_{\mathrm{OP}} g\Delta\rho}{2}. \tag{B.4}$$

With the values $h_{\mathrm{OP}} = 80$ km and $\Delta\rho = -130$ kg m^{-3} used by Holt *et al.* (2015), eq. (B.4) gives $\sigma_{ss} \approx 50$ MPa. This agrees almost exactly with the numerical prediction of fig. 15a of Holt *et al.* (2015).

Appendix C

Numerical implementation

We ran all the simulations using a nonuniform mesh with increased resolution along the upper surfaces of the plates and along the portions adjoining the subduction interface (figure C.1). This choice follows from the requirement that the distance between the observation point and the integration point in the Green's functions used in the BEM approach must always be larger than the size of the element in order to avoid loss of accuracy (Pozrikidis, 1992). In our problem, this requires paying particular attention to the discretization of the subduction interface where two surfaces are close together.

With these considerations in mind, we built our mesh as follows. We began by choosing the lower limit of the interface thickness upon which to calibrate the corresponding resolution at the interface. Once this is done, we can safely go to wider interfaces being sure that the accuracy criterion explained above is satisfied. We fixed this value at $d_2 = 0.08h_{\mathrm{SP}}$, which represents a robust limit to simulate sufficiently strong interfaces ($\gamma = 12.5$) in a wide range of viscosity ratios, that is, $10^2 \leq \lambda_i \leq \times 10^5$, $i = 1$ or 2. Thinner interfaces (e.g., $d_2 = 0.05h_{\mathrm{SP}}$) could have been adopted but not in combination with high viscosity ratios ($\lambda_i > 5 \times 10^4$)

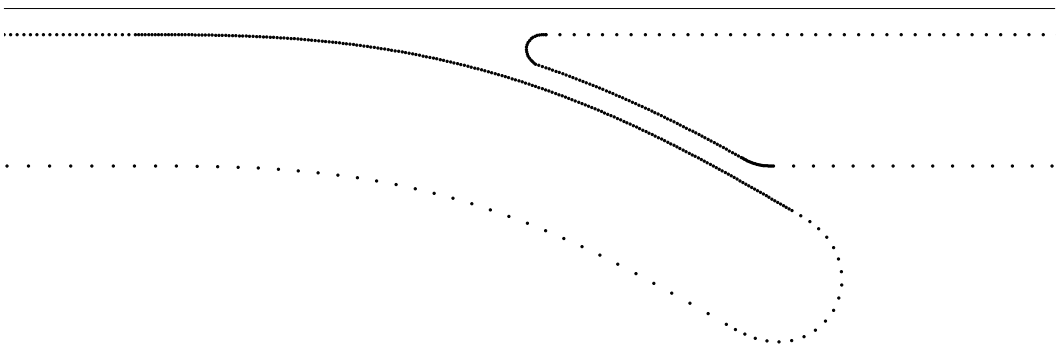

Figure C.1. Mesh of the model.

for which we obtained unphysical flow fields. Next, we imposed a reasonable resolution for the lower surface of the plates ($=0.1h_{\mathrm{SP}}$) and we quadrupled it at the interface obtaining a constant element size of $\approx 0.025h_{\mathrm{SP}}$. For the instantaneous solutions of the model, this mesh represents a good balance between accuracy and computational cost: decreasing the resolution by a factor of 2 led to an average error of 10% while increasing it by the same factor resulted in exactly the same flow field but with a significant slowdown in the computational time.

Finally, we made sure that the mesh maintained adequate resolution during time-dependent simulations. In principle, the natural evolution of the interface(not constrained with any 'contact algorithm') could reduce the thickness of the lubrication layer to below the fixed element size $0.025h_{\mathrm{SP}}$. To verify that this does not occur, we started from an initial SI thickness $d_2 = 0.08h_{\mathrm{SP}}$ and let the system evolve until the slab's tip reached the depth $x_2 = -6.6h_{\mathrm{SP}}$, keeping trace of the minimum distance $d_2^{\mathrm{min}}(t)$ between the two plates. We observed that d_2^{min} never went below ≈ 0.068, so that the accuracy criterion was fulfilled. We also verified that doubling the resolution of the mesh did not result in any significant changes in the computed flow field.

Bibliography

Abbott, D., Burgess, L., Longhi, J., & Smith, W. H. An empirical thermal history of the Earth's upper mantle. *Journal of Geophysical Research: Solid Earth*, 99 (B7):13835–13850, 1994.

Alba-Simionesco, C., Coasne, B., Dosseh, G., Dudziak, G., Gubbins, K., Radhakrishnan, R., & Sliwinska-Bartkowiak, M. Effects of confinement on freezing and melting. *Journal of Physics: Condensed Matter*, 18(6):R15–R68, 2006.

Androvandi, S., Davaille, A., Limare, A., Foucquier, A., & Marais, C. At least three scales of convection in a mantle with strongly temperature-dependent viscosity. *Physics of the Earth and Planetary Interiors*, 188(3-4):132–141, 2011.

Babeyko, A. & Sobolev, S. High-resolution numerical modeling of stress distribution in visco-elasto-plastic subducting slabs. *Lithos*, 103(1-2):205–216, 2008.

Bacchin, P., Brutin, D., Davaille, A., Di Giuseppe, E., Chen, X. D., Gergianakis, I., Giorgiutti-Dauphiné, F., Goehring, L., Hallez, Y., Heyd, R., *et al.* Drying colloidal systems: Laboratory models for a wide range of applications. *The European Physical Journal E*, 41(8):94–127, 2018.

Bellahsen, N., Faccenna, C., & Funiciello, F. Dynamics of subduction and plate motion in laboratory experiments: Insights into the "plate tectonics" behavior of the Earth. *Journal of Geophysical Research: Solid Earth*, 110(B1):1–15, 2005.

Bercovici, D. The generation of plate tectonics from mantle convection. *Earth and Planetary Science Letters*, 205(3-4):107–121, 2003.

Bijwaard, H., Spakman, W., & Engdahl, E. R. Closing the gap between regional and global travel time tomography. *Journal of Geophysical Research: Solid Earth*, 103(B12):30055–30078, 1998.

Birch, F. Density and composition of mantle and core. *Journal of geophysical research*, 69(20):4377–4388, 1964.

Boccaletti, M., Nicolich, R., & Tortorici, L. New data and hypothesis on the development of the Tyrrhenian basin. *Palaeogeography, Palaeoclimatology, Palaeoecology*, 77(1):15–40, 1990.

Buffett, B. & Becker, T. Bending stress and dissipation in subducted lithosphere. *Journal of Geophysical Research: Solid Earth*, 117(B5), 2012. doi: 10.1029/2012JB009205.

Buffett, B. A. Plate force due to bending at subduction zones. *Journal of Geophysical Research: Solid Earth*, 111(B9), 2006. doi: 10.1029/2006JB004295.

Canright, D. & Morris, S. Buoyant instability of a viscous film over a passive fluid. *Journal of Fluid Mechanics*, 255:349–372, 1993.

Capitanio, F., Morra, G., & Goes, S. Dynamic models of downgoing plate-buoyancy driven subduction: Subduction motions and energy dissipation. *Earth and Planetary Science Letters*, 262(1-2):284–297, 2007.

Chen, Z., Schellart, W. P., & Duarte, J. C. Overriding plate deformation and variability of fore-arc deformation during subduction: Insight from geodynamic models and application to the Calabria subduction zone. *Geochemistry, Geophysics, Geosystems*, 16(10):3697–3715, 2015.

Chen, Z., Schellart, W. P., Strak, V., & Duarte, J. C. Does subduction-induced mantle flow drive backarc extension? *Earth and Planetary Science Letters*, 441: 200–210, 2016.

Christensen, U. R. Thermal evolution models for the Earth. *Journal of Geophysical Research: Solid Earth*, 90(B4):2995–3007, 1985.

Cogley, J. G. Continental margins and the extent and number of the continents. *Reviews of Geophysics*, 22(2):101–122, 1984.

Cogné, J.-P. & Humler, E. Temporal variation of oceanic spreading and crustal production rates during the last 180 My. *Earth and Planetary Science Letters*, 227(3-4):427–439, 2004.

Conrad, C. P. & Hager, B. H. Effects of plate bending and fault strength at subduction zones on plate dynamics. *Journal of Geophysical Research: Solid Earth*, 104(B8):17551–17571, 1999a.

Conrad, C. P. & Hager, B. H. The thermal evolution of an Earth with strong subduction zones. *Geophysical Research Letters*, 26(19):3041–3044, 1999b.

Courtillot, V., Davaille, A., Besse, J., & Stock, J. Three distinct types of hotspots in the Earth's mantle. *Earth and Planetary Science Letters*, 205(3-4):295–308, 2003.

Crameri, F. & Kaus, B. J. Parameters that control lithospheric-scale thermal localization on terrestrial planets. *Geophysical Research Letters*, 37(9):1–6, 2010.

Davaille, A. & Jaupart, C. Transient high-Rayleigh-number thermal convection with large viscosity variations. *Journal of Fluid Mechanics*, 253:141–166, 1993.

Davaille, A. & Limare, A. Laboratory studies of mantle convection. *Treatise on Geophysics*, 7:73–144, 2015.

Davaille, A. & Vatteville, J. On the transient nature of mantle plumes. *Geophysical Research Letters*, 32(14):1–6, 2005.

Davaille, A., Smrekar, S., & Tomlinson, S. Experimental and observational evidence for plume-induced subduction on Venus. *Nature Geoscience*, 10(5):349–355, 2017.

Davies, G. F. Thermal histories of convective Earth models and constraints on radiogenic heat production in the Earth. *Journal of Geophysical Research: Solid Earth*, 85(B5):2517–2530, 1980.

Davies, G. F. *Dynamic Earth: Plates, plumes and mantle convection*, 2001.

Davies, G. F. Effect of plate bending on the Urey ratio and the thermal evolution of the mantle. *Earth and Planetary Science Letters*, 287(3-4):513–518, 2009.

Deuss, A. & Woodhouse, J. Seismic observations of splitting of the mid-transition zone discontinuity in Earth's mantle. *Science*, 294(5541):354–357, 2001.

Di Giuseppe, E., Van Hunen, J., Funiciello, F., Faccenna, C., & Giardini, D. Slab stiffness control of trench motion: Insights from numerical models. *Geochemistry, Geophysics, Geosystems*, 9(2):1–19, 2008.

Di Giuseppe, E., Davaille, A., Mittelstaedt, E., & François, M. Rheological and mechanical properties of silica colloids: from Newtonian liquid to brittle behaviour. *Rheologica acta*, 51(5):451–465, 2012.

Duarte, J. C., Schellart, W. P., & Cruden, A. R. Three-dimensional dynamic laboratory models of subduction with an overriding plate and variable interplate rheology. *Geophysical Journal International*, 195(1):47–66, 2013.

Duarte, J. C., Schellart, W. P., & Cruden, A. R. How weak is the subduction zone interface? *Geophysical Research Letters*, 42(8):2664–2673, 2015.

Engdahl, E., Flinn, E. A., & Massé, R. P. Differential PKiKP travel times and the radius of the inner core. *Geophysical Journal of the Royal Astronomical Society*, 39(3):457–463, 1974.

England, P. & McKenzie, D. A thin viscous sheet model for continental deformation. *Geophysical Journal of the Royal Astronomical Society*, 70(2):295–321, 1982.

England, P. & McKenzie, D. Correction to: A thin viscous sheet model for continental deformation. *Geophysical Journal of the Royal Astronomical Society*, 73 (2):523–532, 1983.

Faccenna, C., Davy, P., Brun, J.-P., Funiciello, R., Giardini, D., Mattei, M., & Nalpas, T. The dynamics of back-arc extension: An experimental approach to the opening of the Tyrrhenian Sea. *Geophysical Journal International*, 126(3): 781–795, 1996.

Fukao, Y., Obayashi, M., Inoue, H., & Nenbai, M. Subducting slabs stagnant in the mantle transition zone. *Journal of Geophysical Research: Solid Earth*, 97 (B4):4809–4822, 1992.

Funiciello, F., Moroni, M., Piromallo, C., Faccenna, C., Cenedese, A., & Bui, H. A. Mapping mantle flow during retreating subduction: Laboratory models analyzed by feature tracking. *Journal of Geophysical Research: Solid Earth*, 111 (B3):1–16, 2006.

Funiciello, F., Faccenna, C., Heuret, A., Lallemand, S., Di Giuseppe, E., & Becker, T. Trench migration, net rotation and slab–mantle coupling. *Earth and Planetary Science Letters*, 271(1-4):233–240, 2008.

Garel, F., Goes, S., Davies, D., Davies, J. H., Kramer, S. C., & Wilson, C. R. Interaction of subducted slabs with the mantle transition-zone: A regime diagram from 2-D thermo-mechanical models with a mobile trench and an overriding plate. *Geochemistry, Geophysics, Geosystems*, 15(5):1739–1765, 2014.

Gerardi, G. & Ribe, N. M. Boundary element modeling of two-plate interaction at subduction zones: Scaling laws and application to the Aleutian subduction zone. *Journal of Geophysical Research: Solid Earth*, 123(6):5227–5248, 2018.

Gerya, T. Future directions in subduction modeling. *Journal of Geodynamics*, 52 (5):344–378, 2011.

Giannandrea, E. & Christensen, U. Variable viscosity convection experiments with a stress-free upper boundary and implications for the heat transport in the Earth's mantle. *Physics of the Earth and planetary interiors*, 78(1-2):139–152, 1993.

Goes, S., Capitanio, F. A., & Morra, G. Evidence of lower-mantle slab penetration phases in plate motions. *Nature*, 451(7181):981–984, 2008.

Grigné, C., Labrosse, S., & Tackley, P. J. Convective heat transfer as a function of wavelength: Implications for the cooling of the Earth. *Journal of Geophysical Research: Solid Earth*, 110(B3):1–16, 2005.

Heuret, A. & Lallemand, S. Plate motions, slab dynamics and back-arc deformation. *Physics of the Earth and Planetary Interiors*, 149(1-2):31–51, 2005.

Holt, A., Becker, T., & Buffett, B. Trench migration and overriding plate stress in dynamic subduction models. *Geophysical Journal International*, 201(1):172–192, 2015.

Irvine, D. & Schellart, W. Effect of plate thickness on bending radius and energy dissipation at the subduction zone hinge. *Journal of Geophysical Research: Solid Earth*, 117(B6):1–14, 2012.

Jaupart, C. & Mareschal, J.-C. *Heat Generation and Transport in the Earth*. Cambridge University Press, 2010.

Jaupart, C. & Parsons, B. Convective instabilities in a variable viscosity fluid cooled from above. *Physics of the Earth and Planetary Interiors*, 39(1):14–32, 1985.

Jaupart, C., Labrosse, S., & Mareschal, J. Temperatures, heat and energy in the mantle of the Earth. *Treatise on Geophysics*, 7:253–303, 2015.

Jochum, K., Hofmann, A., Ito, E., Seufert, H. M., & White, W. K, U and Th in mid-ocean ridge basalt glasses and heat production, K/U and K/Rb in the mantle. *Nature*, 306(5942):431–436, 1983.

Kaus, B. J. & Podladchikov, Y. Y. Initiation of localized shear zones in viscoelastoplastic rocks. *Journal of Geophysical Research: Solid Earth*, 111(B4): 1–18, 2006.

Kim, S. & Karrila, S. J. *Microhydrodynamics: Principles and Selected Applications*. Courier Corporation, 2013.

Kincaid, C. & Olson, P. An experimental study of subduction and slab migration. *Journal of Geophysical Research: Solid Earth*, 92(B13):13832–13840, 1987.

Klein, E. Geochemistry of the igneous oceanic crust. *Treatise on Geochemistry*, 3:433–463, 2003.

Klein, E., Fleitout, L., Vigny, C., & Garaud, J. Afterslip and viscoelastic relaxation model inferred from the large-scale post-seismic deformation following the 2010 Mw 8.8 Maule earthquake (Chile). *Geophysical Journal International*, 205 (3):1455–1472, 2016.

Kohlstedt, D., Evans, B., & Mackwell, S. Strength of the lithosphere: Constraints imposed by laboratory experiments. *Journal of Geophysical Research: Solid Earth*, 100(B9):17587–17602, 1995.

Korenaga, J. Energetics of mantle convection and the fate of fossil heat. *Geophysical Research Letters*, 30(8):20–24, 2003.

Krien, Y. & Fleitout, L. Gravity above subduction zones and forces controlling plate motions. *Journal of Geophysical Research: Solid Earth*, 113(B9):1–20, 2008.

Labrosse, S. & Jaupart, C. Thermal evolution of the Earth: Secular changes and fluctuations of plate characteristics. *Earth and Planetary Science Letters*, 260 (3-4):465–481, 2007.

Lallemand, S., Heuret, A., & Boutelier, D. On the relationships between slab dip, back-arc stress, upper plate absolute motion, and crustal nature in subduction zones. *Geochemistry, Geophysics, Geosystems*, 6(9):1–18, 2005.

Leng, W. & Zhong, S. Constraints on viscous dissipation of plate bending from compressible mantle convection. *Earth and Planetary Science Letters*, 297(1-2): 154–164, 2010.

Li, J. & Fei, Y. Experimental constraints on core composition. *Treatise on Geochemistry*, 3:527–557, 2014.

Li, Z.-H. & Ribe, N. M. Dynamics of free subduction from 3-D boundary element modeling. *Journal of Geophysical Research: Solid Earth*, 117(B6):1–18, 2012.

Limare, A., Vilella, K., Di Giuseppe, E., Farnetani, C., Kaminski, E., Surducan, E., Surducan, V., Neamtu, C., Fourel, L., & Jaupart, C. Microwave-heating laboratory experiments for planetary mantle convection. *Journal of Fluid Mechanics*, 777:50–67, 2015.

Litasov, K. & Ohtani, E. Phase relations and melt compositions in CMAS–pyrolite–H_2O system up to 25 GPa. *Physics of the Earth and Planetary Interiors*, 134(1-2):105–127, 2002.

Lu, Y., Liu, Y., Xu, Y., Wang, L., & Li, J. Size-dependent melting of ice in mesoporous silica. *Philosophical Magazine*, 93(15):1827–1842, 2013.

Manga, M. & Stone, H. Buoyancy-driven interactions between two deformable viscous drops. *Journal of Fluid Mechanics*, 256:647–683, 1993.

Massmeyer, A. *Thermal Instabilities in a Yield-Stress Fluid: From the Laboratory to the Planetary Scale*. PhD thesis, Université Paris Sud-Paris XI, 2013.

McKenzie, D., Jackson, J., & Priestley, K. Thermal structure of oceanic and continental lithosphere. *Earth and Planetary Science Letters*, 233(3-4):337–349, 2005.

McKenzie, D. P. Speculations on the consequences and causes of plate motions. *Geophysical Journal of the Royal Astronomical Society*, 18(1):1–32, 1969.

Meyer, C. & Schellart, W. Three-dimensional dynamic models of subducting plate-overriding plate-upper mantle interaction. *Journal of Geophysical Research: Solid Earth*, 118(2):775–790, 2013.

Mitrovica, J. & Forte, A. A new inference of mantle viscosity based upon joint inversion of convection and glacial isostatic adjustment data. *Earth and Planetary Science Letters*, 225(1-2):177–189, 2004.

Morra, G., Regenauer-Lieb, K., & Giardini, D. Curvature of oceanic arcs. *Geology*, 34(10):877–880, 2006.

Namiki, A. & Kurita, K. The influence of boundary heterogeneity in experimental models of mantle convection. *Geophysical research letters*, 26(13):1929–1932, 1999.

Nataf, H. & Richter, F. Convection experiments in fluids with highly temperature-dependent viscosity and the thermal evolution of the planets. *Physics of the Earth and Planetary Interiors*, 29(3-4):320–329, 1982.

Niazi, M. & Anderson, D. L. Upper mantle structure of western North America from apparent velocities of P waves. *Journal of Geophysical Research*, 70(18): 4633–4640, 1965.

O'Connell, R. & Hager, B. H. On the thermal state of the Earth. *Physics of the Earth's Interior*, 76, 1980.

Pozrikidis, C. *Boundary Integral and Singularity Methods for Linearized Viscous Flow*. Cambridge University Press, 1992.

Press, W., Teukolsky, S., Vetterling, W., & Flannery, B. Numerical Recipes in Fortran 77: The Art of Scientific Computing. Cambridge Univ. *Press, Cambridge*, 1992.

Ribe, N. Bending and stretching of thin viscous sheets. *Journal of Fluid Mechanics*, 433:135–160, 2001.

Ribe, N. Analytical approaches to mantle dynamics. *Treatise on Geophysics*, 7: 145–196, 2015.

Ribe, N. M. The dynamics of thin shells with variable viscosity and the origin of toroidal flow in the mantle. *Geophysical Journal International*, 110(3):537–552, 1992.

Ribe, N. M. A general theory for the dynamics of thin viscous sheets. *Journal of Fluid Mechanics*, 457:255–283, 2002.

Ribe, N. M. Bending mechanics and mode selection in free subduction: A thin-sheet analysis. *Geophysical Journal International*, 180(2):559–576, 2010.

Ricard, Y. Physics of mantle convection. *Treatise on Geophysics*, 7:31–87, 2015.

Rodríguez-González, J., Negredo, A. M., & Billen, M. I. The role of the overriding plate thermal state on slab dip variability and on the occurrence of flat subduction. *Geochemistry, Geophysics, Geosystems*, 13(1):1–21, 2012.

Rose, I. & Korenaga, J. Mantle rheology and the scaling of bending dissipation in plate tectonics. *Journal of Geophysical Research: Solid Earth*, 116(B6):1–21, 2011.

Rowley, D. B. Rate of plate creation and destruction: 180 Ma to present. *Geological Society of America Bulletin*, 114(8):927–933, 2002.

Rudolph, M. L., Lekić, V., & Lithgow-Bertelloni, C. Viscosity jump in Earth's mid-mantle. *Science*, 350(6266):1349–1352, 2015.

Rutland, R. Andean orogeny and ocean floor spreading. *Nature*, 233(5317):252–255, 1971.

Schellart, W. Kinematics of subduction and subduction-induced flow in the upper mantle. *Journal of Geophysical Research: Solid Earth*, 109(B7):1–19, 2004.

Schellart, W. Kinematics and flow patterns in deep mantle and upper mantle subduction models: Influence of the mantle depth and slab to mantle viscosity ratio. *Geochemistry, Geophysics, Geosystems*, 9(3):1–29, 2008.

Schellart, W. & Moresi, L. A new driving mechanism for backarc extension and backarc shortening through slab sinking induced toroidal and poloidal mantle flow: Results from dynamic subduction models with an overriding plate. *Journal of Geophysical Research: Solid Earth*, 118(6):3221–3248, 2013.

Schellart, W., Freeman, J., Stegman, D., Moresi, L., & May, D. Evolution and diversity of subduction zones controlled by slab width. *Nature*, 446(7133):308–311, 2007.

Schellart, W. P. & Strak, V. A review of analogue modelling of geodynamic processes: Approaches, scaling, materials and quantification, with an application to subduction experiments. *Journal of Geodynamics*, 100:7–32, 2016.

Sclater, J., Jaupart, C., & Galson, D. The heat flow through oceanic and continental crust and the heat loss of the Earth. *Reviews of Geophysics*, 18(1): 269–311, 1980.

Sclater, J. G., Parsons, B., & Jaupart, C. Oceans and continents: similarities and differences in the mechanisms of heat loss. *Journal of Geophysical Research: Solid Earth*, 86(B12):11535–11552, 1981.

Shemenda, A. I. Subduction of the lithosphere and back arc dynamics: Insights from physical modeling. *Journal of Geophysical Research: Solid Earth*, 98(B9): 16167–16185, 1993.

Sobolev, S. V. & Babeyko, A. Y. What drives orogeny in the Andes? *Geology*, 33 (8):617–620, 2005.

Solomatov, V. Scaling of temperature-and stress-dependent viscosity convection. *Physics of Fluids*, 7(2):266–274, 1995.

Stein, C. A. *et al.* Heat flow of the Earth. *Global Earth Physics: A Handbook of Physical Constants*, 1:144–158, 1995.

Tackley, P. J. Self-consistent generation of tectonic plates in time-dependent, three-dimensional mantle convection simulations. *Geochemistry, Geophysics, Geosystems*, 1(8):1–45, 2000.

Tommasi, A., Knoll, M., Vauchez, A., Signorelli, J. W., Thoraval, C., & Logé, R. Structural reactivation in plate tectonics controlled by olivine crystal anisotropy. *Nature Geoscience*, 2(6):423–427, 2009.

Turcotte, D. & Schubert, G. *Geodynamics*. Cambridge University Press, 2014.

van Dinther, Y., Morra, G., Funiciello, F., & Faccenna, C. Role of the overriding plate in the subduction process: Insights from numerical models. *Tectonophysics*, 484(1-4):74–86, 2010.

van Hunen, J., van den Berg, A. P., & Vlaar, N. J. A thermo-mechanical model of horizontal subduction below an overriding plate. *Earth and Planetary Science Letters*, 182(2):157–169, 2000.

Wakiya, S. Application of bipolar coordinates to the two-dimensional creeping motion of a liquid. ii. Some problems for two circular cylinders in viscous fluid. *Journal of the Physical Society of Japan*, 39(6):1603–1607, 1975.

Weinstein, S. A. & Olson, P. L. Thermal convection with non-Newtonian plates. *Geophysical Journal International*, 111(3):515–530, 1992.

Titre : Sur la dynamique de la subduction et l'effet des zones de subduction sur la convection du manteau

Mots clés : Dynamique de la lithosphère et du manteau, Modélisation numérique, Convection mantellique, Colloïdes

Résumé : La subduction est une des principales expressions superficielles de la convection mantellique et représente un ingrédient crucial de la géodynamique globale. Cela affecte différents processus de la Terre comme la génération des méga tremblements de terre et des volcans explosif sur la surface ou le recyclage des espèces volatiles dans l'intérieur profond. Malgré son importance, plusieurs aspects de la subduction restent à clarifier.
Dans ce travail, nous avons étudié la mécanique et l'énergétique du phénomène en adoptant un modèle numérique 2-D de "subduction libre", basé sur la méthode des éléments frontière. En interprétant systématiquement nos solutions numériques utilisant la théorie des couches minces visqueuses, nous avons déterminé diverses lois d'échelle décrivant les mécanismes physiques sous-jacents aux différents aspects du phénomène. Deux paramètres adimensionnels se distinguent par leur récurrence dans ces lois d'échelle: i) la *résistance* (adimensionelle) de l'interface de subduction, qui contrôle la contrainte de cisaillement agissant à l'interface entre les deux plaques et ii) la *rigidité* de la plaque en subduction, qui décrit la résistance mécanique opposée par cette plaque à la flexion. Ce dernier paramètre est particulièrement important, car il met en évidence l'échelle de longueur qui décrit correctement la déformation en flexion de la plaque en subduction (*bending length*).
En ce qui concerne les aspects énergétiques de la subduction, nous avons également étudié l'effet de la dissipation de l'énergie produite dans les zones de subduction sur la convection du manteau à grande échelle. Nos résultats semblent suggérer que la loi d'échelle classique trouvée dans l'étude de la convection de Rayleigh-Bénard en régime permanent d'une couche de fluide isovisceux reste généralement valable aussi pour la convection du manteau terrestre.
Pour conclure, nous avons mis en place une expérience de convection basée sur le séchage d'une suspension colloïdale de nanoparticules de silice. Comme les résultats préliminaires ont montré, grâce à sa rhéologie particulière, ce matériau semble être un candidat prometteur pour la construction en laboratoire d'une modèl véritable de la convection mantellique.

Title : On the dynamics of subduction and the effect of subduction zones on mantle convection

Keywords : Dynamics of lithosphere and mantle, Numerical modeling, Mantle convection, Colloids

Abstract : Subduction is one of the principal surface expressions of mantle convection and it represents a key ingredient of global geodynamics. It affects Earth processes ranging from the generation of mega-earthquakes and explosive volcanoes at the surface to the recycling of volatile species back into the deep interior. Yet despite its obvious importance, several aspects of subduction remain to be clarified.
In this work we endeavored to shed light on the mechanics and the energetics of the phenomenon adopting of a 2-D numerical model of "free subduction" based on the Boundary-Element Method. Systematically interpreting our numerical solutions in the light of thin viscous-sheet theory, we determined various scaling laws describing the physical mechanisms underlying different aspects of the phenomenon. Two dimensionless parameters stand out for their recurrence in such scaling laws: i) the (dimensionless) *strength* of the subduction interface, which controls the shear stress acting at the interface between the two plates and ii) the *flexural stiffnes* of the subducting plate, which describes the mechanical resistance opposed by such plate to bending. This latter parameter is particularly important as it highlights the length scale that properly describes the bending deformation of the subducting plate (*bending length*).
For what concerns the energetics of subduction, we also investigated the effect of the dissipation of energy occurring at subduction zones on large-scale mantle convection. Our results seem to suggest that the classical scaling law found in the study of the steady-state Rayleigh-Bénard convection of an isoviscous fluid layer remains generally valid also for Earth's mantle convection.
To conclude, we ran a convection experiment based on the drying of a colloidal suspension of silica nanoparticles. As preliminary results have shown, thanks to its particular rheology, this material seems to be a promising candidate for effective laboratory modeling of mantle convection.

Université Paris-Saclay
Espace Technologique / Immeuble Discovery
Route de l'Orme aux Merisiers RD 128 / 91190 Saint-Aubin, France